Estimating the Performance of Multi-Rotor Unmanned Aerial Vehicle - Structure from Motion (UAV_{SfM}) Imagery in Assessing Homogeneous and Heterogeneous Forest Structures: A Comparison to Airborne and Terrestrial Laser Scanning

By

Kenechukwu Chukwudubem Onwudinjo

ONWKEN001

Submitted to the University of Cape Town in fulfilment of the requirements for the Degree of Master of Science in Engineering (Geomatics)

Supervisor:

Assoc Prof J. Smit

Department of Architecture, Planning and Geomatics

Faculty of Engineering and Built Environment

University of Cape Town

February 2021

DECLARATION

I, Kenechukwu Chukwudubem Onwudinjo, hereby declare that the work on which this dissertation is based is my original work (except where acknowledgements indicate otherwise) and that neither the whole work nor any part of it has been, is being, or is to be submitted for another degree in this or any other university. I empower the university to reproduce for the purpose of research either the whole or any portion of the contents in any manner whatsoever.

Signature: Signed by candidate

Date: 25 February 2021

ACKNOWLEDGEMENT

To my supervisor, Assoc Prof Julian Smit, I offer my immense gratitude for allowing me full control over the procedure of my research, for the advice and the suggestions, and for taking time out of his busy schedule to timeously lend a professional opinion and constructive criticism when needed. I am grateful for him and his patience.

For always being willing to lend an ear and assist in making life more amenable during this endeavour I offer my gratitude to Mignon Wells.

A great many thanks to everyone else who made an impact in my life, in one way or another, both positive and negative, since the first day on this journey. It has been truly beneficial to my growth and has taught me many lessons worth learning.

Finally, it is with great pride and pleasure that I thank my parents, Dr. Ifeanyi J. and Mrs. Chinwe M. Onwudinjo, and my siblings, for their continuous support these few years in completing my research. You are immensely appreciated.

ABSTRACT

The implementation of Unmanned Aerial Vehicles (UAVs) and Structure-from-Motion (SfM) photogrammetry in assessing forest structures for forest inventory and biomass estimations has shown great promise in reducing costs and labour intensity while providing relative accuracy. Tree Height (TH) and Diameter at Breast Height (DBH) are two major variables in biomass assessment. UAV-based TH estimations depend on reliable Digital Terrain Models (DTMs), while UAV-based DBH estimations depend on reliable dense photogrammetric point cloud. The main aim of this study was to evaluate the performance of multi-rotor UAV photogrammetric point cloud in estimating homogeneous and heterogeneous forest structures, and their comparison to more accurate LiDAR data obtained from Aerial Laser Scanners (ALS), Terrestrial Laser Scanners (TLS), and more conventional means like manual field measurements.

TH was assessed using UAV_{SfM} and LiDAR point cloud derived DTMs, while DBH was assessed by comparing UAV_{SfM} photogrammetric point cloud to LiDAR point cloud, as well as to manual measurements. The results obtained in the study indicated that there was a high correlation between UAV_{SfM} TH and ALS_{LiDAR} TH (R^2 = 0.9258) for homogeneous forest structures, while a lower correlation between UAV_{SfM} TH and TLS_{LiDAR} TH (R^2 = 0.8614) and UAV_{SfM} TH and ALS_{LiDAR} TH (R^2 = 0.8850) was achieved for heterogeneous forest structures. A moderate correlation was obtained between UAV_{SfM} DBH and field measurements (R^2 = 0.5955) for homogenous forest structures, as well as between UAV_{SfM} DBH and TLS_{LiDAR} DBH (R^2 = 0.5237), but a low correlation between UAV_{SfM} DBH and UAV_{LiDAR} DBH (R^2 = 0.1114).

This research has demonstrated that UAV_{SfM} can be adequately used as a cheaper alternative in forestry management compared to more high-cost and accurate LiDAR, as well as traditional technologies, depending on accuracy requirements.

Keywords: Unmanned Aerial Vehicles, Structure-from-Motion, Aerial Laser Scanning, Terrestrial Laser Scanning, Tree Height, Diameter at Breast Height, Biomass

APPLICATION FORM

Please Note:
Any person planning to undertake research in the Faculty of Engineering and the Built Environment (EBE) at the University of Cape Town is required to complete this form before collecting or analysing data. The objective of submitting this application *prior* to embarking on research is to ensure that the highest ethical standards in research conducted under the auspices of the EBE Faculty, are met. Please ensure that you have read, and understood the EBE Ethics in Research Handbook (available from the UCT EBE, Research Ethics website) prior to completing this application form: http://www.ebe.uct.ac.za/ebe/research/ethics1

APPLICANT'S DETAILS		
Name of principal researcher, student or external applicant		KENECHUKWU CHUKWUDUBEM ONWUDINJO
Department		ARCHITECTURE, PLANNING AND GEOMATICS
Preferred email address of applicant:		ONWKEN001@myuct.ac.za
If Student	Your Degree: e.g., MSc, PhD, etc.	MSc (ENG) in GEOMATICS
	Credit Value of Research: e.g., 60/120/180/360 etc.	180
	Name of Supervisor (if supervised):	A/PROF. JULIAN SMIT
If this is a research contract, indicate the source of funding/sponsorship		N/A
Project Title		EVALUATING THE PERFORMANCE OF MULTI-ROTOR UAV-SfM IMAGERY IN ASSESSING SIMPLE AND COMPLEX FOREST STRUCTURES: COMPARISON TO AERIAL LASER SCANNING AND TERRESTRIAL LASER SCANNING.

I hereby undertake to carry out my research in such a way that:

- there is no apparent legal objection to the nature or the method of research; and
- the research will not compromise staff or students or the other responsibilities of the University;
- the stated objective will be achieved, and the findings will have a high degree of validity;
- limitations and alternative interpretations will be considered;
- the findings could be subject to peer review and publicly available; and
- I will comply with the conventions of copyright and avoid any practice that would constitute plagiarism.

SIGNED BY	Full name	Signature	Date
Principal Researcher/ Student/External applicant	KENECHUKWU C ONWUDINJO	Signed by candidate	06 Feb 2019

APPLICATION APPROVED BY	Full name	Signature	Date
Supervisor (where applicable)	Julian Smit		06 Feb 2019
HOD (or delegated nominee) Final authority for all applicants who have answered NO to all questions in Section1; and for all Undergraduate research (including Honours).	Patricia Videra		11/2/2019
Chair : Faculty EIR Committee For applicants other than undergraduate students who have answered YES to any of the above questions.			

DEDICATION

sic parvis magna

‘Greatness from small beginnings’

TABLE OF CONTENTS

LIST OF FIGURES

LIST OF TABLES

CHAPTER 1

Introduction

1.1 Research Background

South Africa, in January 2010, pledged to the United Nations Framework Convention for Climate Change (UNFCCC) that it would take Nationally Appropriate Mitigation Action (NAMA) to set in place measures that would ensure a trajectory of 34% emissions of Green House Gases (GHG) below 'business as usual' by the year 2020, and further down to 42% emissions of GHG below 'business as usual' by the year 2025 (Rahlao et al., 2012). This was on the condition that the NAMA receive support from the international community in the form of finance, technology, and capacity building. The United Nations Collaborative Programme on Reducing Emissions from Deforestation and Forest Degradation in Developing Countries (UN-REDD), established in 2008, is a programme that aims to partner with developing countries by supporting them in establishing the technical capacities needed to implement the REDD+, meet their UNFCCC mandates and meet requirements for REDD+ incentives.

The Reducing Emissions from Deforestation and forest Degradation, and foster conservation, sustainable management of forests, and enhancement of forest carbon stocks (REDD+) is regarded by most and especially its supporters, as a very cost-effective and efficient way to mitigate the effects of climate change in developing countries (Rahlao et al., 2012). Implementing the REDD+ initiative also aims to construct technical knowledge and technical capability on the ground with improved methods or techniques of monitoring, reporting and verifying data on forest resources (Ratnasingam et al., 2014). This, in turn, could help reduce depletion of forests and promote their sustainable use. There are several developing countries around the globe that have already enlisted to benefit from the programme. In Africa alone, Nigeria, Kenya, Ethiopia, Ghana, Uganda, Mozambique, and the Democratic Republic of the Congo are a few countries currently running local REDD+ programmes.

However, despite the numerous benefits of the REDD+, there are critical challenges associated with developing and subsequently implementing the programme in developing

countries, specifically in Africa. Funding, complex land tenure systems, methods of data collection and manipulation, as well as capacity and technological issues are just a few of the obstacles faced by developing African countries (Makhado et al., 2011). South Africa, a developing country, and an African economic powerhouse is currently not part of the REDD+ programme.

In addition to the obstacles mentioned by Makhado et al. (2011), South Africa has an approximate land surface area of 122 062 764 ha, and of that only 1 257 341 ha, 1.3% of the country's total land surface, is comprised of forestland (DEA, 2014). The country's forestlands are made up of about 35% indigenous woodlands/savannas that range from sparsely wooded grasslands to dense thickets and woodlands. This means that such woodlands and savannas are relatively low in carbon stocks per hectare, typically around <30 tC ha^{-1} compared to most other woodlands and tropical forests (Rahlao et al., 2012). Thus, compared to other southern African countries such as Zambia, which has one of the largest forest resources in southern Africa (66% of its total land mass is covered in forests) (Ratnasingam et al., 2014) and Malawi which, in 2015, had forests make up 33.4% of its total land cover (FAO, 2016), South Africa does not possess much forestland that is in danger of deforestation or degradation in order to incentivise partaking in the programme. However, according to FAO FRA (2012), a "forest" is defined as "*Land spanning more than 0.5 ha with trees higher than 5 meters and a canopy cover of more than 10%, or trees able to reach these thresholds in situ. It does not include land that is predominantly under agricultural or urban land use*". The UNFCCC's definition of a "forest" includes most of the country's vegetation types and woodlands.

1.2 Problem Statement

One of the requirements to benefit from the REDD+ mechanism is that participating countries of the UNFCCC report their verified national biomass and carbon estimates. It is therefore expected of these countries to have capable systems for carbon monitoring and technologies or methodologies with which to obtain this data (Kachamba, Eid and Gobakken, 2016). Many developing countries rely on National Forest Inventories (NFIs) for their biomass and carbon stock estimates. Estimates for sample plots are used to estimate various vegetation types and then applied over the same forest strata.

Unfortunately, many of these countries do not have comprehensive NFIs; run on high operational costs and are highly labour intensive.

Due to these limitations in the conventional acquisition of the necessary measurements and subsequent estimation of biomass, Remote Sensing has been playing a vital role in the last few decades with estimating above ground biomass, henceforth referred to as AGB (Günlü et al., 2014). It has been extensively used in forest management and monitoring as it provides observations over a large area, making the process repetitive while offering a time saving alternative. This data is thus long-term (Maina, Odera and Kinyanjui, 2017), meaning that data over a specific area can be accessed over long periods of time making time-series analysis possible. Techniques such as the use of satellite imagery is a popular and valuable alternative to conventional methods because they contain spatial attributes, can be used to monitor a singular area over a period of time and are relatively inexpensive depending on the platform (Maina, Odera and Kinyanjui, 2017). Most satellites have the added advantage of either providing multispectral or hyperspectral imagery which in some instances can be obtained freely. This data can then be used to measure nutrient invariability, mineral presence, and even biomass. However, this data is usually flawed with providing poor spatial resolution, typically between 10 m/px as is found on the Sentinel-2A Satellite Sensor, to 30 m/px, found in data obtained from the LANDSAT 7 Enhanced Thematic Mapper Plus (ETM+) and the LANDSAT 8 Operational Land Imager (OLI) and Thermal Infrared Sensor (TIRS) Satellite Sensors. In addition to the poor spatial resolution, the images are periodically captured with extensive cloud cover and must be processed through lengthy endeavours to remove the unwanted clouds.

Over the last few decades Remote Sensing has offered up other alternatives to satellite imagery as a substitute to conventional methods in forestry management, analysis, and monitoring in the form of Radar, Aerial Laser Scanning (ALS) and Terrestrial Laser Scanning (TLS). Unfortunately, though these systems have proven useful in their unparalleled ability, they are expensive to acquire, and where necessary have high establishment costs or produce poor point density, or both. ALS and TLS systems, for example, both produce three-dimensional LiDAR data but are quite expensive to obtain and both produce a point density of ±1 to ±15 points/m^2 depending on the sensor used. Whereas most ALS systems have the advantage of covering large swaths of areas and can penetrate thick forest canopies they fail at adequately capturing below canopy forest structures such as complete

tree trunks if loaded with a low point density sensor. TLS boasts the ability to capture below canopy forest structures but falls short at capturing the top forest canopy, is incredibly labour intensive and time-consuming (Brede et al., 2017).

The use of Unmanned Aerial Vehicle (UAVs) and Structure-from-Motion (SfM) Photogrammetry can therefore improve the reliability of estimated biomass and carbon stocks data while greatly reducing operational costs and labour intensity. UAVs can be flown at much lower altitudes which allows, in some cases, an image spatial resolution of as high as 1 cm/px, or higher, depending on the sensor mounted. Because they are low altitude platforms, they also eliminate the possibility of cloud cover as flight takes place beneath cloud formation. Due to these added advantages, as well as their small and nimble size, manoeuvrability around forest structures is possible which makes them capable of capturing above and below canopy imagery of forest structures such as treetops, tree trunks and the forest floor, which are all crucial in the formation of three-dimensional point cloud, digital terrain and surface models.

It is the aim of this research to assess the overall feasibility of UAV applications in biomass estimations of homogeneous and heterogeneous *Pinus* forest structures in South Africa in the effort to support its UNFCCC goals and mandates. At the time of writing, there are no sourced published literature of this sort of undertaking in South Africa.

1.3 Scope and Limitations

The overarching aim of this research is to evaluate the performance of multi-rotor UAV_{SfM} imagery in assessing homogeneous and heterogeneous *Pinus* forest structures, specifically in Cape Town, in the Western Cape of South Africa. This is done by comparing the UAV_{SfM} results obtained from designated study sites to the results obtained from both ALS and TLS of the same study sites. Within the scope of this research homogeneous *Pinus* forest structures comprise of 'ideal' environments defined by open top canopy, sparsely spaced trees, similar tree species and with little or no undergrowth of sub-species; while heterogeneous *Pinus* forest structures comprise of 'realistic' forestry environments characterised by a dense or closed top canopy, high tree density, possible combination of various tree species, and the possible presence of below canopy sub-species.

Due to several constraints such as time, equipment, scope, and requirements of permits the research is limited in the location of the study sites, plant species and size of the study sites. Sample locations are selected based on two criteria – (1) Most forests in Cape Town are under management of SANParks and a permit must be obtained to acquire aerial imagery as is stated on their website: "*In terms of Regulation 20(1)(a) of the regulations under the National Environmental Management: Protected Areas Act, nobody may in a national park undertake "the filming and simultaneous transmitting of photographic images by the use of a webcam or other image recording or transmitting device", unless a filming permit has been obtained*" (SANBI, 2019), leaving only areas outside SANParks management; and (2) due to Western Cape's Mediterranean climate the *Pinus* species (Pine tree) is commonly found throughout the region making the gathering of data more cost effective and less tedious. As such, this research assesses UAV_{SfM} imagery of three *Pinus* species at three different locations, namely the *Pinus pinaster* in the Steenbras Dam Nature Reserve, *Pinus pinea* found at Rondebosch Common, and *Pinus radiata* found on the Upper Campus of the University of Cape Town (UCT).

The research also focuses on measuring two forest structure variables namely Diameter at Breast Height (DBH) and Tree Height (TH) because these two measurements hold the most influence on AGB (Kachamba et al., 2016b), and do not require additional equipment.

1.4 Research Questions

1. What are the necessary data, procedures, standards, and ideal conditions that make UAVs an effective tool in AGB estimation?

2. Are the various factors, such as cost, labour intensity, accuracy, spatial resolution, applicability, scale, and estimation correlation enough to make UAV usage a more viable option compared to current methods or technologies?

3. How can biomass estimation with UAVs be improved in terms of standards or procedures to improve results or efficacy?

1.5 Aim

The main aim of this project is to obtain allometric variables such as DBH and TH from UAV_{SfM} photogrammetric point cloud data and its derivative products and compare those to the same variables obtained from Aerial Laser Scanning and Terrestrial Laser Scanning LiDAR to assess the use of multi-rotor UAVs as an alternative in the forestry data capture process in South Africa in order to meet its UNFCCC mandates and assist its involvement in the UN-REDD and REDD+ programmes.

1.6 Objectives

1. To investigate what necessary data, standards, and ideal conditions are necessary to carry out measurement and feature extraction of forest features and structures using a multi-rotor UAV and SfM photogrammetry,

2. To use existing and collected data to compare labour intensity, spatial resolution, and spatial accuracy of more accurate technologies such as ALS_{LiDAR} and TLS_{LiDAR} to UAV_{SfM} within the study areas and to validate these UAV_{SfM} derived feature measurement results, and

3. To conclude and make recommendations on the efficiency and effectiveness of capturing homogeneous and heterogenous *Pinus* forest structures in South Africa using multi-rotor UAV_{SfM} photogrammetry in support of bridging technological gaps for the REDD+ programme in the country.

1.7 Organisation of the Document

This research is divided in 6 chapters that detail the evaluation of multi-rotor UAVs and SfM imagery in assessing homogeneous and heterogeneous *Pinus* forest structures. A brief outline if each chapter is detailed below.

Chapter 1: Introduction

In the Introductory chapter, the essential research background detailing the purpose for which the research exists, the problem definition and presentation of the aims and objectives for this research project are presented.

Chapter 2: Literature Review and Theoretical Background

The literature review covers the various concepts, experiments, investigations and activities related to biomass estimation and remote sensing techniques in biomass estimation which include the use of UAVs, ALS, TLS, and Satellite Imagery in biomass estimation to place the project in its academic context.

Chapter 3: Data and Study Area

This chapter discusses in detail the data sources required for such an endeavour and the data required for this project, as well as the study areas used.

Chapter 4: Research Methods

A detailed discussion of the methodology, procedures, experiments, decisions, and challenges undertaken to acquire the data. It also details the processing done on the raw data to acquire the information needed for the estimation of DBH and TH.

Chapter 5: Results and Discussion

The results and discussion chapter places emphasis on the results and discussions stemming from the project findings. This chapter provides the necessary information acquired after processing has been done, as well as the statistical evidence that supports various experiments carried out earlier. It also discusses the efficacy of UAV_{SfM} in estimating the fundamental tree variables for biomass estimation based on rudimentary formulae.

Chapter 6: Conclusions and Recommendations

A conclusive chapter consisting of conclusions drawn from the project based on the processing and results. The chapter also details observations and recommendations based around the findings generated from earlier chapters.

CHAPTER 2

Literature Review and Theoretical Background

2.1 Biomass and Estimation of Biomass

Biomass is all material of a biological nature – wood, crops, or animal waste – that isn't a derivative of, or stored in, geological formations (fossil fuels) (IRENA, 2016). There are generally four types of biomass in use globally – solid waste, wood and agricultural products, landfill gas and biogas, and ethanol (NEED, 2006). Whereas any biological material can constitute as biomass, plant biomass, specifically, can be defined as the dry mass of living plant material contained above or below a unit surface area of ground at any given point in time or per unit time. Biomass stored in woodlands or grasslands, whether above ground in tree trunks; branches; or leaves, or below ground in roots, plays a vital role as either carbon sinks (Dandois, Olano and Ellis, 2015; Tongwane, Mdlambuzi and Moeletsi, 2016) or biofuel (DEA, 2014). Due to its versatility, biomass is either used in its original form or can be processed and refined into other kinds of solid, liquid or gaseous biofuels depending on the need.

Because of its ease of access and abundance in nature, energy from biomass (bioenergy) contributed to 14% of the global energy consumption in 2012, with approximately 2.6 billion people depending on conventional biomass forms for their energy needs – mostly cooking and heating (IRENA, 2016). This burning of biomass to release energy however produces carbon dioxide (CO_2), and carbon monoxide (CO). South Africa for example, in 2013, had a contribution of 25 624 tonnes oil equivalent (TOE) to its gross electricity generation from biomass and biofuels (IRENA, 2016).

Carbon production is frequently a more common and useful way of representing biomass than representing it in weight per unit area (IRENA, 2016). This is due to trees and their natural ability to sequester CO_2, because they act as carbon sinks. Although all trees possess the ability to sequester carbon, it is possible that the carbon content may vary from species to species despite, in some cases, having a similar biomass weight. Therefore, it is necessary to measure biomass and carbon stocks specific to tree or plant species.

Various methods exist for the estimation of plant biomass, whether woodlands, grasslands, or agricultural crops. However, the choice of method and procedure thereafter is generally influenced by the size of the area (scale to be covered), the economic value of the vegetation being assessed, time constraints, accessibility, and level of accuracy required, etc. For the estimation of aboveground biomass (AGB) in grasslands or small agricultural crops, a popular approach involves dividing the stand into quadrats and then dividing the harvested dry plant mass, or forced-air dried plant mass, by the quadrat area (Bao, Gao and Gao, 2009), as indicated in equation 2.1 below. In this way, the biomass per unit area can be calculated.

A study by Bao et al. (2009) measured the biomass of winter wheat by dividing a study area into several 0.6 m by 0.5 m sample quadrats. The crops, when harvested from each quadrat and weighed, had their weights recorded. The crops were then forced-air dried in a drying oven at about 60 °C, over 24 hours. The dried plant mass was then weighed, in grams, and divided by the sample area (in this case, 0.3 m^2) measured earlier using equation 2.1 (Bao, et al., 2009):

$$AGB\ (g/m^2) = \frac{Dry\ Plant\ Mass\ (g)}{Sample\ Area\ (m^2)} \tag{2.1}$$

Although this method does equate the biomass measurement for specific plant species, it produces the biomass mass of those plant species per specific unit area, in this case x number of *grams* of winter wheat per m^2, and not the biomass of each individual wheat crop. The other limitation with this method is that it is destructive, as the plants need to be harvested and then forced-air dried before they can be weighed, as opposed to waiting for the stage in the crop life when the plants lose their moisture content naturally. This method has two drawbacks however – waiting for the plants to naturally dry out could take months which makes it a time-consuming method, and its destructive nature is not suitable for assessing biomass of large vegetation types like trees.

When estimating tree biomass, several approaches exist, and can be distinguished between destructive and non-destructive methods (Kumar and Mutanga, 2017). Non-destructive approaches include evaluation through biomass expansion factors (Lehtonen et al., 2004) which convert tree stem volume into whole-tree biomass; physiologically-based models such as 3PG as suggested by Landsberg, Waring and Coops (2003) which use temperature,

rainfall and solar radiation information to predict total tree biomass; and allometric equations that can predict total tree biomass using several measured variables such as TH and DBH (Ter-Mikaelian and Korzukhin, 1997; Parresol, 1999; Zianis et al., 2005; Kachamba et al., 2016a), measured with instruments such as the clinometer and calliper respectively. Allometric equations are unfortunately not very useful in heterogonous forests, but rather in homogeneous forests or plantations with trees or stands of similar age (Kumar and Mutanga, 2017). In conventional biomass estimation involving field campaigns, each tree is individually assessed. Tree diameter, measured as DBH is a popular variable measured for allometric equations and is measured at 1.37 m (4.5 ft) above the ground, although this differs in some parts of the world. The measurement can be made with several different instruments but most popular are a measuring tape or callipers. The manner in which the measurement is taken can differ drastically depending on the shape of the tree trunk, and the terrain it grows on, as suggested by Malone, Liang and Packee (2009) in *Figure 2.1*.

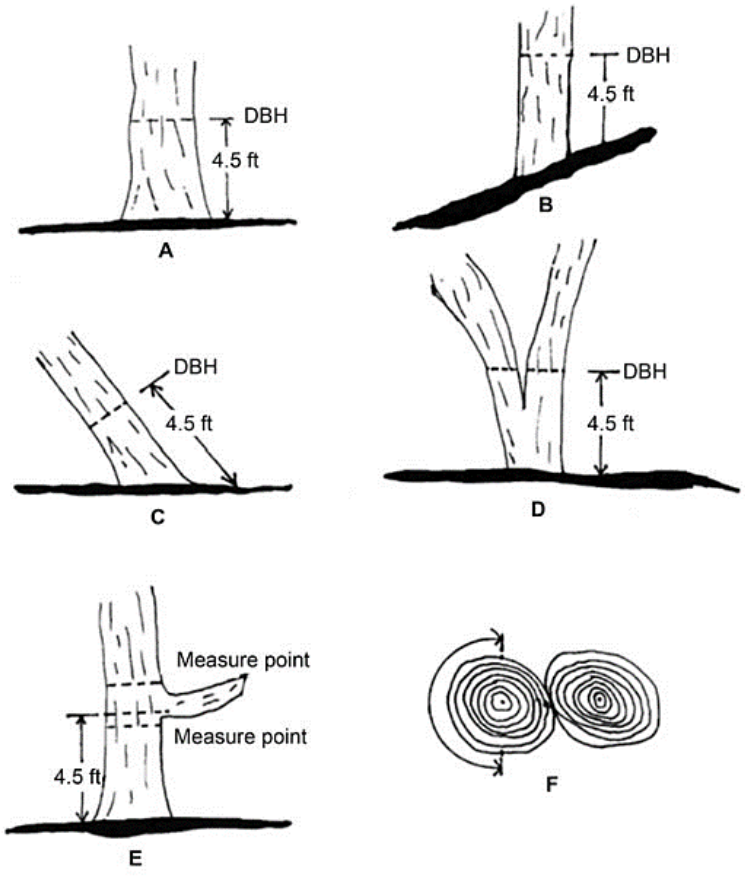

Figure 2.1 | *Several methods for measuring tree diameter using the Diameter at Breast Height (DBH) method (Malone et al., 2009)*

Allometric equations have been developed for individual trees of several different tree species, including *Pinus radiata* trees and stands. However, these equations can be stand and site specific so there is potential to introduce some level of uncertainty when applied on a national level for national biomass or carbon stock estimations because of the vast array of differences in site types, differing tree-age classes and stand structure (Moore, 2010). In order to apply these equations to trees and stands not directly sampled, regression analysis must be performed on the collected sample data to produce a regression model to relate total AGB to tree variables like DBH, TH and tree volume (DBH^2TH). A traditional non-linear allometric equation has the form (Moore, 2010):

$$AGB = \beta_0 X_1^{\beta_1} X_2^{\beta_2} \dots \dots X_p^{\beta_p} \quad (2.2)$$

where AGB is the total above ground biomass, X_I is the tree dimension variable such as TH or DBH (I = 1, 2…., p), and β_I are the model parameters (I = 0, 1…., p). Additive or multiplicative constants can be assumed (Moore, 2010). Where the objective is to develop above- and below ground biomass models that can be applicable across entire distributions of specific tree species, often for merchantable projects, then a destructive method – harvest method – approach is applied. This is especially popular in homogenous forests, like pine plantations (Kumar and Mutanga, 2017). In this sampling approach, each tree sample is deconstructed into their components: branches on the tree above a predefined height and minimum diameter, tree stem above a predefined height above the ground, and twigs within a predefined diameter. These tree components are dried in an oven between 60 °C and 80 °C until a constant weight is achieved. Adding the dry weights of the various components together gives the total above ground biomass, as was done for *Pinus radiata* forests in New Zealand (Moore, 2010), and moimbo woodlands in Malawi (Kachamba et al., 2016a).

Destructive methods are limited to small scale practices because of its nature, nor is it suitable for areas located where threatened flora or fauna exist (Kumar and Mutanga, 2017). Field methods, both destructive and non-destructive, that entail the measuring of each individual tree in the sample data can be costly campaigns, in monetary value, in time and in labour intensity because large numbers of trees for the sample data need to be assessed which can usually tally between tens and hundreds of trees (Kachamba, et al., 2016a; Moore, 2010).

2.2 Remote Sensing in Above Ground Biomass Estimation

Whereas biomass estimated through field methods is perhaps the most accurate way of obtaining these measurements, it is not very practical over large scales (Kumar and Mutanga, 2017) for reasons previously mentioned. Numerous studies have however shown that Remote Sensing, and its related techniques and technologies, can provide data, on a large scale, at a fraction of the cost and allows areas previously inaccessible by normal means to be accessed. Remote Sensing platforms include optical sensors, Light Detection and Ranging (LiDAR), Radio Detection and Ranging (RADAR), etc. Because science is an ever-evolving field different techniques and technologies emerge continually, and alterations and adaptations of previous works are investigated for the purpose of estimating AGB. This section discusses some of the applications of several remote sensing technologies and techniques in estimating biomass.

2.2.1 Satellite Biomass Estimation

Optical Remote Sensing is perhaps the most popular alternative platform used for biomass estimation because it is incredibly cost-effective, as it is in most cases free and accessible as long as there is internet access; it is scalable; has immense global coverage; is repetitive (Kumar and Mutanga, 2017); and has a long history of use (Galidaki et al., 2017). The popularity of optical remote sensing is mainly attributed to the fact that solar radiation reacts mostly with tree foliage, and because of this optical imagery contains a lot of crucial top-canopy information. As such, numerous studies have established successful relationships between optical remote sensing data and woody forest biomass (Galidaki et al., 2017). Several platforms exist, each one having its own set of advantages over the other - from varying revisit periods to image resolution ranging from coarse image resolution (100 m – 1000 m), medium image resolution (20 m – 30 m) and very high spatial resolution (VHR) (0.5 m – 10 m). Popular satellites used in related studies include LANDSAT, MODIS, IKONIS, Quickbird, WorldView, SPOT and Sentinel to name a few.

Satellites are equipped with special sensors that detect wavelengths across the electromagnetic spectrum. These wavelengths are recorded in the satellite as bands, or images. Different satellites record a different number of bands. For instance, LANDSAT 8

OLI & TIS records 11 bands – one band for aerosol, three bands for visible light, one band for near-infrared, two bands for short wavelength infrared, one band for panchromatic, one for cirrus and two bands for long wavelength infrared (GISGeography, 2019). In contrast, Sentinel-2 records two additional bands (*Figure 2.2*) – one band for aerosol, three for visible light, four for red edge vegetation, one for near-infrared, one for water vapour, and three for short wavelength infrared with one focusing on cirrus (ESA, 2019a).

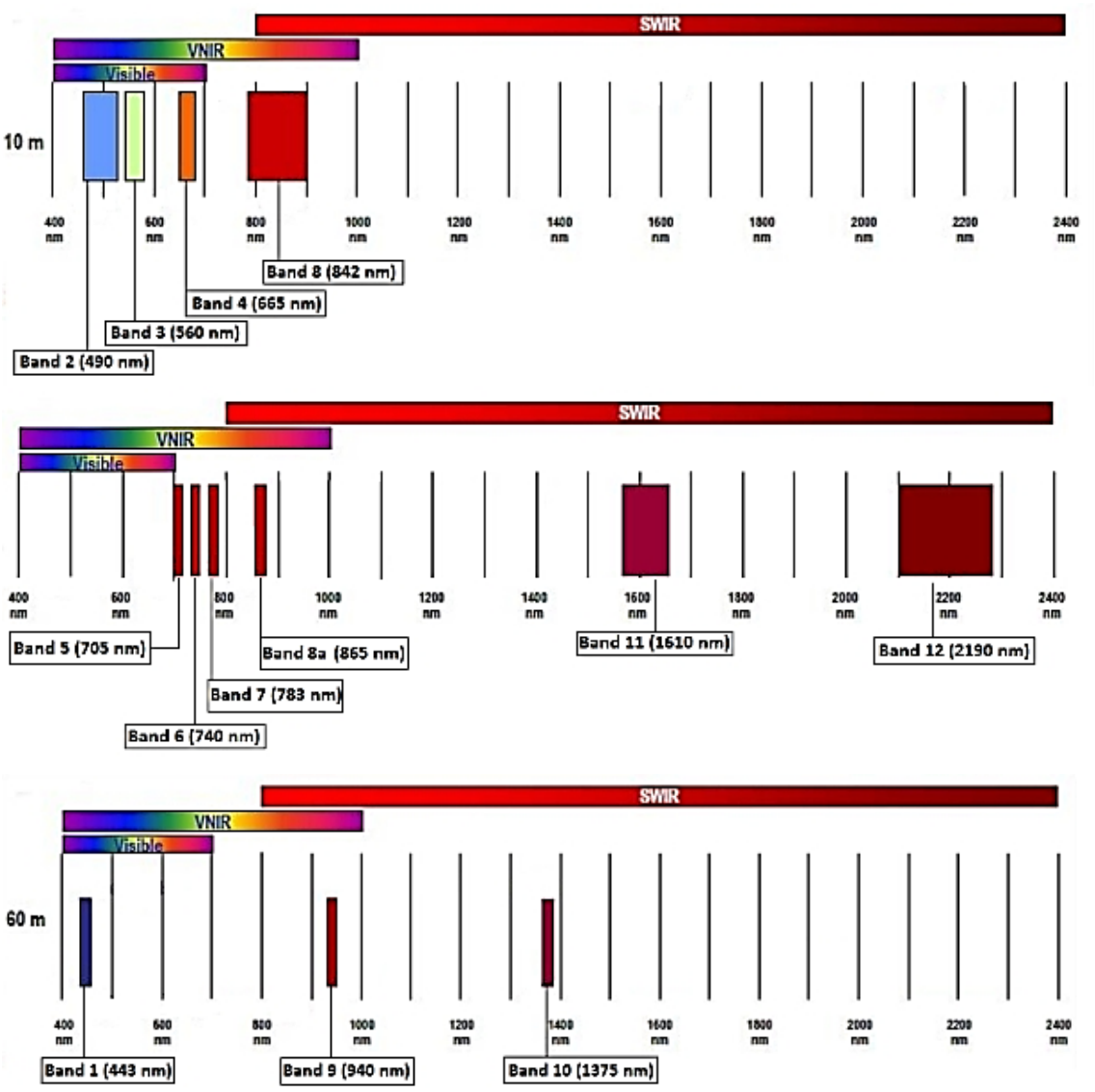

Figure 2.2 | *Sentinel-2 band composition and wavelengths at (a) 10 m, (b) 20 m and (c) 60 m spatial resolution (ESA, 2019b)*

These multispectral images acquired from satellites make it possible to process, classify and estimate biomass, and perform other spectral analysis on vegetation in large forested areas such as natural forests, or plantations, using numerous techniques.

Roy and Ravan, (1996) used satellite remote sensing to estimate biomass values of various homogenous vegetation strata (*Anogelssus pendula, Boswellia serrata, Acacla catechu, Butea monosperma, Riparian* etc) by creating multiple regression equations using extrapolated brightness and wetness parameters from LANDSAT TM multispectral images. The images were used to create False Colour Composites (FCC) for visual interpretation of areas that were bright and wet. The model found a R^2 = 0.77 correlation coefficient between brightness, wetness, and predicted biomass; and a 10.5% error margin between observed and predicted biomass values.

LANDSAT TM and MODIS image data have been used in a study by Bao et al. (2009) to estimate winter wheat biomass. The images were acquired periodically during the growth stages of wheat - from the early-erecting stage, to the grain-filling stage. These images were captured by both satellites as they revisited the location above the study area. Several spectral indices like Normalised Difference Vegetation Index (NDVI), Modified Soil-Adjusted Vegetation Index (MSAVI), Enhanced Vegetation Index (EVI), Renormalized Difference Vegetation Index (RDVI), Normalized Difference Water Index (NDWI) and Structure Insensitive Pigment Index (SIPI) were then calculated using the respective band combinations needed for the indices (red and near-infrared are common bands in calculating vegetation indices). Multiple regression equations subsequently modelled using the indices values and measured biomass values at the known locations to create a relationship model for the prediction of biomass at unknown locations. The models provided good correlation coefficients between some indices and measured biomass, with NDVI showing the best results (Bao et al., 2009). This proved that spectral information acquired from satellite imagery can be used to estimate biomass. NDVI has been affirmed as a highly suitable index for the measure of biomass in forest structures (Carlson and Riziley, 1997; Jones et al., 2007; Galidaki et al., 2017).

Jones et al. (2007) noted strong logarithmic asymptotic correlations between Fractional Vegetative Cover (%VC) and biomass in a published study, backed by research conducted by Carlson and Riziley, (1997). Though not an optical satellite system, the terrestrial-based study used reflectance-based multispectral information captured with a GreenSeeker handheld optical sensor unit (AgriOptics, 2019), produced by NTech Industries, Inc., Ukiah, California. The system electronically separates natural incident light and light produced

from the sensor LEDs, after which a voltage signal from the LEDs is produced that relates to the wavelengths of both red and near-infrared light (Jones et al., 2007). Using this, NDVI is calculated. Relational models calculated and formulae used can be perused in the study by Jones et al. (2007). Relationships using both linear and exponential equations were then used to relate %VC, measured biomass and NDVI. The study found an excellent correlation between biomass and NDVI (R^2 = 0.94), and %VC and biomass (R^2 = 0.91). The %VC is calculated as the fraction of the area that represents vegetation (NDVI), which in the study when compared to biomass levels harvested from the same areas presented excellent correlations (R^2 = 0.91 during Autumn, and R^2 = 0.96 during Spring the next year). The study proved that %VC, derived from multispectral data, could serve as a means of estimating vegetative biomass as well.

Another study by Maack et al. (2015) used WorldView-2 imagery to estimate forest biomass in Chile and Germany. The study compared random forest model performances of different predictor sets namely spectral, textual, and photogrammetric. The model showed that stereo-VHR imagery showed high potential for generating photogrammetric point cloud data that could be used to create Canopy Height Models (CHMs), which is the difference between a Digital Surface Model (DSM) and a Digital Terrain Model (DTM), and could be viable alternatives to LiDAR or SAR (Synthetic Aperture Radar) techniques. Model results varied between the two study sites but modelled biomass best when using a combination of spectral and photogrammetric predictors (Root Mean Square Error (RMSE) 46.60 t/ha) compared to models that either used a single predictor between spectral (RMSE 50.39 t/ha), textural (RMSE 48.55 t/ha) or photogrammetric (RMSE 50.28 t/ha) predictors; or a combination of the textural and photogrammetric (RMSE 46.99) predictors. The next best model used all three predictors (RMSE 46.67 t/ha). Using photogrammetric products like CHMs, coupled with spectral information like an orthomosaic greatly improves biomass estimation (Maack et al., 2015).

2.2.2 Aerial and Terrestrial Laser Scanning in Estimating Biomass

LiDAR data is a product of Aerial and Terrestrial Laser Scanning and is an active remote sensing technology. It determines the distance, or range, and bearing of a target object to the sensor. This is achieved by emitting a laser pulse from the sensor to the target, and in conjunction with the speed of light, measures the time lapse for the emitted laser to reach

its target (Lim et al., 2003). Some more advanced scanners are able to record the full waveform of the returned pulses and can therefore reconstruct some canopy attributes (Brede et al., 2017). Though LiDAR has only gained more popularity in the last few decades in several fields, especially in various engineering disciplines for uses such as pipeline modelling (Skarlatos and Kiparissi, 2012), it has been explored in forestry applications since the late 1970s. One of the earliest studies recorded was a study (Arp, Griesbach and Burns, 1982) which used an aerial laser profile recorder to map tree canopy profiles to determine tree heights in Central American tropical forests.

Applications of aerial LiDAR in forestry assessments have since then greatly increased due to major advances in Global Positioning Systems (GPS) and Inertial Measurement Units (IMU) (Lim et al., 2003). Commercial GPS receivers onboard the aircraft work in tandem with one or more GPS bases or ground stations to provide differentially corrected positions of the aircraft at every point of the flight, while the IMU, also onboard the aircraft, measures the orientation (roll, pitch, and yaw) of the sensor, and by extension the aircraft, during flight.

The information obtained from both these sensors, and the use of the precise clock information downloaded from satellites, allows for the post-processing, either with GNSS or Precise Point Processing (PPP) of the data using proprietary black-box codes in third-party software to calculate trajectories of the aircraft and geo-code the laser data (Lim et al., 2003). Using the precise GPS coordinates and the IMU information (roll, pitch, and yaw) it is possible to calculate the exact position of the LiDAR sensor and its orientation at the moment each laser pulse is emitted, and then using the measured distance from the sensor to the captured object the exact coordinates of each laser point can be calculated. This results in a fully georeferenced LiDAR point cloud of the terrain below, with each point containing information such as horizontal and vertical, as well as other attributes.

Terrain and height models are popular products and an immediate application of LiDAR data (Brede et al., 2017) in Forestry Management Inventories (FMIs) because although they lack spectral or textural information they provide structural information and can therefore be used to estimate forest structures and variables such as Canopy Height (CH) or TH (St-Onge et al., 2008; García et al., 2010; Gonzalez et al., 2010; Simonson et al., 2016; Olofsson and Holmgren, 2017); and if the point density and canopy penetration are high enough,

DBH can be estimated (García et al., 2010; Chisholm et al., 2013; Lamprecht et al., 2015; Brede et al., 2017; Olofsson and Holmgren, 2017; Yurtseven, Akgül and Gülci, 2017).

A prerequisite for the development of DTMs, DSMs, CHMs or calculation of CH using LiDAR data is the identification or classification of some form of ground surface or reference surface below what is believed to be the canopy surface (Lim et al., 2003). To achieve this, points that are interpolated as possible ground points, and represent some sort of reference terrain, are filtered, or classified as such, and the other remaining points are classified as vegetation or buildings/structures using vegetation or building clustering or filtering algorithms embedded in the GIS or processing software, depending on the environment being scanned. The difference between these two surfaces, one surface comprising of only ground points (DTM) and the other ground and vegetation points (DSM), yields the Canopy Height Model (Brede et al., 2017). Tree heights or canopy heights for the individual trees within the terrain model can then be extracted from the overlaid position of these trees. These values, along with DBH values of the same trees, extracted from the point cloud, are entered in regression models as independent variables to estimate tree biomass (Pommerening, 2007; Lim et al., 2003; García et al., 2010).

Despite its success, there are some drawbacks to using LiDAR data. For instance, it is not uncharacteristic of laser scanners to return some spurious points in the point cloud. These are outlier points captured by the sensor during missions and can be caused by errors including atmospheric effects; or errors in the Time Interval Meter (which time-stamps each laser return) (Lim et al., 2003); GPS drift which occurs when the GPS momentarily loses signal from satellites causing the registration of floating points; or in some cases outlier points that are caused by random objects like birds momentarily entering the path of the laser (common in ALS). It is common for these spurious points to be represented as exaggerated spikes in either elevation or depression in the produced terrain models and must therefore be cleaned or filtered out before the generation of the models as these errors could result in an inaccurately modelled terrain. It is often not too challenging to notice these spikes as they form obvious and unnatural deformities in the rendered Digital Elevation Model (DEM) – a digital representation of the terrain. A common issue in some cases where dense forests are captured using LiDAR data is that it is challenging to verify from the point cloud data whether clustered terrain depressions within the stands and below the canopy are actually erroneous points that need to be removed, or whether they

are true representations of the terrain. As such, some amount of ground truthing will always be necessary for verification.

ALS is generally acquired from manned aircraft to cover huge swaths of ground, but this can be a costly campaign due to fuel and establishment costs. Additionally, acquired ALS LiDAR data has a typically low point density, usually in the region of 1 to 10 points/m^2, depending on the flight height and other mission parameters that govern ground sampling distance (GSD). This is highly inefficient for capturing and reconstructing complete tree structures, especially below-canopy tree structures such as stems, branches, twigs, etc (Brede et al., 2017). However, some research have attempted assessing below-canopy structures using low point density ALS data, such as a study by Montealegre et al. (2016a) that achieved good results using ALS data with a point density of 1 point/m^2. Compared to ALS, TLS platforms are better suited at acquiring below-canopy structures and data, such that single canopy elements like stems and branches can be captured. This is because TLS point cloud is very dense – in the order of millions of points from a single scan position. TLS is, however, laborious and time consuming (Brede et al., 2017).

TLS LiDAR can produce high point density data that create elaborate point cloud models of the structures being scanned, eg. *Figure 2.3* below. However, it is also subject to limitations. One additional characteristic of TLS is the loss of data on the far side of the object - tree stems etc - being scanned referred to in this research as ‘shading’. These gaps can often look like shadows cast on the ground and are caused by insufficient scan angles and locations to cover the object from various perspectives. The figure below shows the effect of ‘shading’ caused by scanning trees from just one scan position.

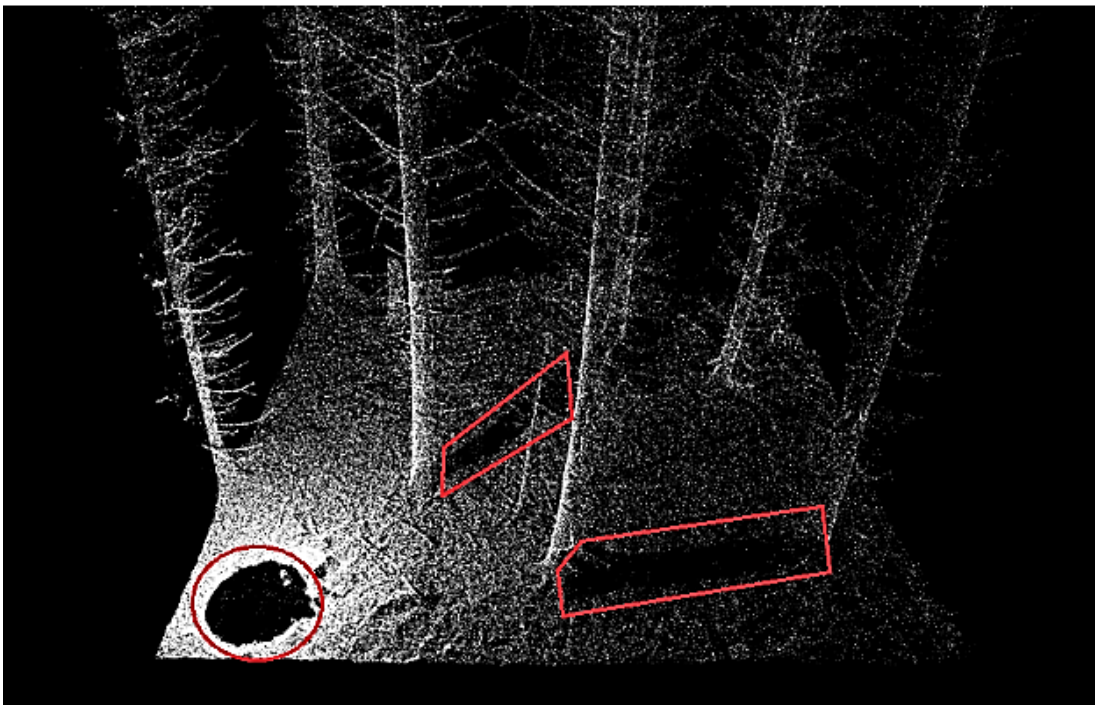

Figure 2.3 | *Shading occurs on the far side of the trees and below the sensor at the scan location (areas in red polygons)* (Olofsson and Holmgren, 2017).

To combat shading, it is usually necessary to have multiple scan locations to cover multiple perspectives of the object being scanned and obtain data of the tree stems that have missing data (Olofsson and Holmgren, 2017). This can unfortunately have the added disadvantage of adding several additional scan locations to manoeuvre around the stand and acquire information from multiple perspectives. A cumbersome task, that not only makes fieldwork arduous and time-consuming but also makes registration and processing of the scans time-consuming because of the sheer number of scan locations and the large LiDAR file sizes which can be demanding on computing power. Nonetheless, LiDAR data has proven to be a successful means of assessing various forest structures and biomass carbon stocks based on encouraging results.

Biomass carbon stock for a Mediterranean forest was estimated in Central Spain using ALS LiDAR height and intensity data (García et al., 2010), which is the measure of the return strength of the laser pulse. Intensity is, in part, a function of the reflectivity or composition of the observed surface. The study showed that intensity-based models provided the most accurate predictions of biomass, showing correlation coefficients of over R = 0.58 for different biomass factions (total aboveground, branches and foliage). When prevailing

species in the mixed-species sample plots were assessed correlation coefficient values increased to R^2 = 0.85 in Black Pine, R^2 = 0.70 in Spanish Juniper and R^2 = 0.90 in Holm Oak.

Another ALS LiDAR data-based study measured forest carbon densities and uncertainties in redwood (Sequoia sempervirens) from ALS LiDAR, Quickbird and field measurements in California found a high correlation between stand-level LiDAR heights and field mean heights in two sites. Correlation between LiDAR heights and field mean heights were *R* = 0.94 and *R* = 0.89 respectively (Gonzalez et al., 2010). Numerous other studies have shown LiDAR data as a superior data acquisition technology for FMIs (Lim et al., 2003).

A 2016 study in Spain attempted using low density ALS LiDAR data to estimate field stand metrics like mean height, mean diameter, timber volume, basal area, etc using LiDAR data with a point density of 1 point/ m^2. Aboveground heights were obtained by producing two different 1 m cell grid DEMs. One, using the classified ground points, and the other, using all the captured LiDAR points. The ground DEM was subtracted from the DEM containing all the points to produce the normalised heights (Montealegre et al., 2016). Tree diameter was measured in the field by calculating the diameter at breast height of all trees with a DBH >7.5 cm at a height above ground of 1.3 m. This approach yielded R^2 of 0.87 for mean height and R^2 of 0.84 for squared mean diameter. This suggests that the approach can yield decent results when assessing stand-level structural variables when using low density point cloud data.

2.2.3 Synthetic Aperture Radar (SAR) in Estimating Biomass

Like LiDAR, RADAR imaging is an active remote sensing technique. As is the case with LiDAR, active sensors provide their own source of illumination to acquire data from a target, but RADAR systems achieve this by using microwaves to acquire this data. Microwaves exist within a very broad region of the electromagnetic spectrum, between 1 cm and 1 m in wavelength (*Figure 2.4*), in contrast to the visible and infrared regions.

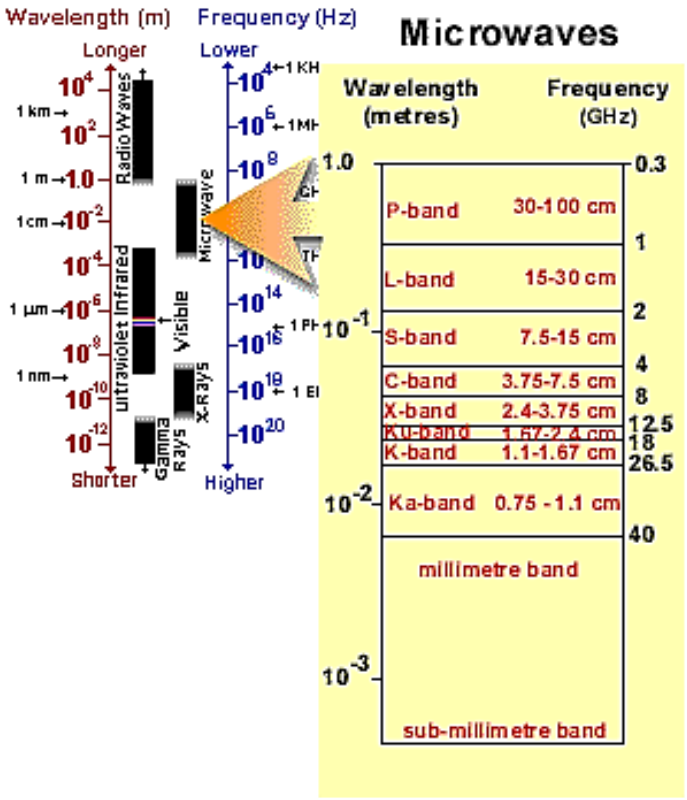

Figure 2.4 | *The microwave region within the electromagnetic spectrum* (CCRS/CCT, 2016a)

Microwave sensors are either imaging or non-imaging (CCRS/CCT, 2016b), with the most common form of microwave imaging being RADAR. RADAR systems, which capture signals within the microwave region of the electromagnetic spectrum, comprise of a transmitter; a receiver; an antenna and some internal electrical systems to process and record the captured data. *Figure 2.4* above displays the several wavelengths or bands that make up the microwave region of the spectrum. Microwave bands, from the shortest bands (Ka, K and Ku) to the longest (the P-band) have been used extensively in acquiring data. Using the processed radar signals, it is possible to model a DEM of the terrain below and acquire three-dimensional information.

A popular technique when using RADAR is SAR, which is an either space borne or aerial side looking radar with a forward moving trajectory. This configuration allows the platform to simulate a large electronic antenna or aperture. To acquire data, the transmitter emits successive bursts or pulses of microwaves at a regular interval and the antenna receives the backscattered portion of the initially transmitted signal (CCRS/CCT, 2016a). The intensity of the backscattered signal helps discern between different features being acquired like vegetation or rooftops, while the time delay between signal transmission and

reception helps range the distance between the sensor and the object being acquired. SAR has become very popular in remote sensing due to several advantages but most notably that microwaves can be used to acquire images in all kinds of weather conditions; they are independent of the time of day; because of the length of the waves, they are able to penetrate through vegetation top-canopy, as well as through the soil. Microwaves are also minimally affected by atmospheric effects; sensitive to dielectric properties (difference between frozen and liquid water); and are quite sensitive to structure. These properties have not only made RADAR technology especially popular in surveillance and mapping but have also seen rising popularity in vegetation mapping and modelling.

The limitation with radar imagery is that it is often grainy and hard to interpret as opposed to optical imagery data, this makes cleaning up of RADAR data arduous, which can require some level of skill. RADAR systems are also not as common as other active sensors like LiDAR so they are often limited to being mounted on high altitude aircraft and/or satellites, as opposed to laser scanners that can additionally be mounted on a tripod (TLS), or mobile platforms like cars. (Colomina and Molina, 2014), however, reports several SAR sensors common or representative of SAR for UAS used in studies in recent years. As with most aerial and space borne platforms coverage may be greatly increased because the platform is at a higher altitude and each image can span large swaths of space - swath width varies typically from a few kilometres to 20 km aerial platforms and from an average 30 km to 500 km in space borne platforms (CCRS/CCT, 2016a) - however, resolution will be compromised. None the less, the various microwave bands have found several uses as is illustrated in the table below –

Table 2.1 | *Commonly used SAR bands, their frequency, wavelength and common uses* (CCRS/CCT, 2016a)

Frequency Band	**Ka**	**Ku**	**X**	**C**	**S**	**L**	**P**
Frequency (Ghz)	40–25	17.6–12	12–7.5	7.5–3.75	3.75–2	2–1	0.5–0.25
Wavelength (cm)	0.75–1.2	1.7–2.5	2.5–4	4–8	8–15	15–30	60–120
Notable Uses		Snow monitoring				Penetration of canopy vegetation, biomass estimation and subsurface imaging	

*****Bands Ka and X are used for High-resolution imagery.

Where band L and P are used for biomass estimation, considerable penetration is possible to image the objects such as forestry or vegetative clusters so that volumetric modelling is possible. This therefore makes volumetric biomass estimations possible and popular with SAR.

Aboveground biomass of a forested area was evaluated by creating an extended water cloud model (EWCM) using Polarimetric Synthetic Aperture Radar (PolSAR) data acquired from Advanced Land Observation Satellite (ALOS) (Kumar et al., 2019). The PolSAR-decomposition-based volume scattering and AGB were used as input model parameters in regression models to derive AGB for the forested area. The approach yielded an AGB value of 92.0 t/ha, while recording R^2 = 0.36 in the linear regression model between the field measured AGB and the AGB output from the model before de-orientation of the PolSAR data; but recorded 59.77 t/ha and R^2 = 0.78 after de-orientation of the PolSAR data.

Another 2009 study used ALOS PALSAR L band (HH and HV polarisation) data to estimate AGB in Kenya (Maina, Odera and Kinyanjui, 2017). The study compared various tree measurements acquired through field data to ALOS PALSAR images. Due to the ALOS PALSAR's use of the L-band frequency cloud free images were obtained, making it possible to accurately estimate AGB of the tropical forests. Regression analysis was performed between the estimated and measured data from various test sites and found a regression value in the first test site of 0.880 for the HV band and 0.520 for the HH band, and 0.708 for the HV band and 0.511 for the HH band in the second test site. Although the study does not indicate why HV polarisation performs better than HH polarisation, the results showed potential for the use of HV PALSAR data in estimating AGB and other tree measurements, especially DEM derived tree height.

2.3 Unmanned Aerial Vehicles (UAV) in Imagery

UAVs, and with the inclusion of a ground control or monitoring system with a data link to the UAV, then called Unmanned Aerial Systems (UASs), are pre-programmed or manually flown winged or multi-rotor flying robots. This is the modern definition of the acronym;

however, this was not always the case. In the late 1880s balloons, hot-air balloons, kites and rockets were some of the first UAVs used in capturing aerial photography. One of the first recorded aerial photographs taken were by Gaspard-Felix Tournachon in Paris in the late 1850s using a hot air balloon (Aber and Babb, 2018). While the first remotely controlled UAVs were developed and used for gunnery practice by the Royal Navy in 1933, the Wright Brothers' had already developed the radio-controlled aircraft, the Hewitt-Sperry automatic airplane, in 1916 (Colomina and Molina, 2014). Unmanned aerial vehicles have since their inception not only seen use in especially military but also increasingly in the various geosciences and engineering disciplines, more so in the last two decades with the increased production of cheap commercially available UAVs. The potential of UAVs however, as a mapping platform, only began being researched and documented in the late 1970s, as is evident by the little research on the matter available before that period.

A 1979 aerial photography study by Przybilla and Wester-Ebbinghaus, which was one of the first studies published on the matter, saw the use of a 3 m long fixed-wing and radio-controlled UAS equipped with an automatic optical camera (format size of about 6 cm by 6 cm). The aircraft, flown at 40 km/h and at a height of 150 m above ground, captured images of the terrain below but the images were unfortunately blurry due to engine vibrations (Wester-Ebbinghaus and Przybilla, 1979). This was expected because in addition to motor vibrations and wind resistance the images are taken from a lightweight moving platform (Mikhail, Bethel and McGlone, 2001).

A year later, in 1980, Przybilla and Wester-Ebbinghaus carried out a similar study, only this time using a radio-controlled rotary-wing model helicopter modelled after the Bell 222 helicopter and carrying a Rolleiflex camera. The aircraft had to be fitted with suppressors this time in an effort to counteract the vibrations caused by the rotary-wing mechanism during flight. With this modification, flight manoeuvrability and stability improved a great deal. Quality images could now be acquired, and from heights between 10 m and 100 m as opposed to 150 m as was the case with the fixed-wing UAV from their previous study (Wester-Ebbinghaus, 1980).

In another study in the year 2000, a radio-controlled model helicopter was fabricated with an aluminium camera mount to help lift a Rolleiflex 6006 camera to capture aerial images of vertical façades at an archaeological site (Theodoridou et al., 2000). The aim of this study

was to produce three-dimensional structures using overlapping images and photogrammetric processes. Previous studies and experiments had shown that motor vibrations were a problem when acquiring quality images with unmanned aerial vehicles so all the connections in the UAV framework had to be reinforced with elastic dampers and silicone-rubber suspension to absorb as much vibration from the rotor and avoid transferring those vibrations to the camera mount. The study however does not describe the nature of the results obtained but a similar study, also in the year 2000, using a fabricated remote-controlled model helicopter equipped with a Kodak DCS460c digital camera to acquire vertical façade aerial imagery of a building for architectural photogrammetric purposes. The study achieved results of an average of ±0.03 mm or ±2 pixel in image coordinates after processing and an average of ±2 cm in all coordinates of the façade and roof points in the resulting photogrammetric point cloud (Zischinsky et al., 2000). Retrofitting these model UAVs with special dampers, the camera mounts are able to help combat motion blur and rotor vibrations to guarantee high quality pictures (Zischinsky et al., 2000).

Rotor-wing UAVs were quite popular in the early 2000s, as such Nagai et al. (2004) also used an unmanned and remotely controlled Subaru RPH2 helicopter equipped with a GPS/IMU and mounted with a Canon EOS D60 CCD (Charged Coupling Device) camera, along with a SICK LMS291 laser scanner to simultaneously capture data from the two sensors to produce a Digital Surface Model. This approach proved that multiple sensors could be loaded on a single unmanned aerial platform to improve feature detection from LiDAR data by adding texture information from the data captured from the CCD camera sensor. The UAV weighed around 330 kg and had a 100 kg payload, while the main rotor had a diameter of 4.8 m. The platform had an operational range of about 3 km and could fly autonomously for ±1 hr. The platform was able to acquire high-resolution data while moving at speeds of 1.8 m/s but could fly as high as 2000 m above mean sea level. This system was first proposed at the 2004 International Society for Photogrammetry and Remote Sensing (ISPRS) congress in Phitsanulok, Thailand and would pave the way for many future platforms aimed at incorporating texture from aerial imagery into LiDAR data captured from both a CCD sensor and laser scanner, respectively. The LiCHy – LiDAR, CCD and Hyperspectral Integrated Airborne Observation System by Pang et al. (2016) was able to achieve this.

Figure 2.5 | *Subaru RPH2 Multi-sensor model helicopter* (Nagai et al., 2004)

Fixed-wing UAVs had begun gaining popularity for civilian use as well by this time, such as the Pegasus UAV system. As with most fixed-wing UAVs, they have the ability to be airborne for lengthy periods and ascend to much higher altitudes, which make them ideal for remote sensing purposes over large areas. However, because they lack the ability to hover over a position they struggle to acquire images at specified acquisition points (Eisenbeiss, 2009). A study by Wang, et al. (2004) utilised a fixed-wing UAV to map buildings by acquiring consecutive images for photogrammetric processing. However, due to motion blur most of the images were unusable and only a single aerial image was used to produce an orthoimage and overlay that on a two-dimensional GIS database to produce three-dimensional models of the buildings. A whole new algorithm had to be developed to achieve this. Studies by Jayathunga, et al. (2018) and Fraser and Congalton (2018) both used fixed-wing UAVs to study heterogeneous forest structures.

It is evident then that by the turn of the 21st century fixed-wing and rotary-wing UAVs were the desired choice of unmanned aerial systems for capturing aerial imagery for a variety of purposes, though with some amendable difficulties. However, other forms of UAVs were still in use such as kites. Aber and Babb (2018) used kite aerial photography (KAP) to collect imagery data and test the results obtained when processed with modern photogrammetry techniques. The study found that although kites provide a low-cost alternative in aerial image acquisition comparative to its winged counterparts, a huge problem is the

irregularity in the source imagery. Unlike typical UAVs, fixed-wing, and rotary-wing UAVs, that are either flown manually or pre-programmed to fly in a line or grid pattern while acquiring imagery, there is so much more variance in camera rotations because of the erratic camera movement while on its ascent or at its desired height. This can result in less images being acquired around the edges of the site. This is a contributing factor to the kite's decreased popularity since the later part of the 20th century (Aber and Babb, 2018). Kites also have the challenge of being tethered – they are held onto by rope or chord by the operator because they are not designed to rise too high above ground while not in direct view of the operator. This can limit the scale that the platform can cover, depending on the length of the rope or chord. Kites are also heavily weather dependant, since less than ideal winds could make controlling them over a predefined path very challenging. This makes it harder to hover over a point (Eisenbeiss, 2009). The University of Bonn in Germany developed a manually controlled kite system with a ~4.1 kW 2 stroke engine. The frame is attached to a paraglider, which serves as its wing, ensuring stable flight.

Although kites are used for some photogrammetric studies, popularity has fallen more on the use of fixed-wing and rotary-wing UAVs. They have found popularity in a number of applications like archaeology surveying and building construction monitoring (Zischinsky, et al., 2000) and (Theodoridou et al., 2000), close range architectural photogrammetry (Carnevali et al., 2018), biomass estimation (Afif-Khouri et al., 2013) and (Meng et al., 2016), building construction progress monitoring (Bognot et al., 2018), assessing species-specific forest inventories (Puliti et al., 2017), monitoring greenhouse emissions from forests in developing countries (Mlambo et al., 2017) and monitoring biodiversity in forests (Bagaram et al., 2018).

Over the last decade, there has been an explosion in cheaper commercially available UAVs. These platforms have seen the replacement of huge liquid fuel powered model helicopters like the ones used by Wester-Ebbinghaus and Przybilla (1979), Wester-Ebbinghaus (1980) and Nagai et al. (2004). A huge contributor to the explosion of these commercially available UAVs is the integration of Lithium-ion Polymer (Li-ion/LiPo) batteries into the frame that allow for an estimated flight time of ±30 min to ± 50 minutes (Jayathunga, Owari and Tsuyuki, 2018). This has led to UAVs being airborne for longer and to fly farther than before resulting in larger area coverage – ideal for mapping large swaths of forest cover. Although smaller in size and weight compared to older UAVs like those referenced earlier, most

current UAVs now come, as a standard, equipped with sensors (Red, Green and Blue (RGB) sensors and in some cases, multispectral sensors) for image capture and several sensors that are necessary for autonomous flight. This is particularly useful as it reduces the chance of human error when remote piloting, which could avert a crash or unwanted system failure.

A comprehensive study by Eisenbeiss (2009) highlights quite extensively the various categories or classifications of UAVs available. Most UAVs used in various sectors and research endeavours presently fall in the M-Class - Micro and Mini UAS - as is suggested in the study put forward by Eisenbeiss (2009), which is the focus UAV class in this dissertation as UAVs in this class have been used and cited in several research papers for their adequate performance relative to cost. This class of UAVs are either fixed-wing or rotary-wing (quadrotor or multirotor) UAVs but with a limited payload of 5 kg (<5 kg).

Further advancements in technology have enabled the integration of smaller low-cost sensors such as Global Navigation Satellite System (GNSS) receivers for navigation, Inertial Navigation Systems (INS) or IMU for orientation, compass, barometers, altimeters, RADAR for obstacle avoidance, and several other sensors into these compact frames. Flight stabilizers are also a common feature for sustained flight, and highly capable optical CCD sensors capable of capturing high-resolution aerial imagery from considerable altitudes. These additions make it possible for UAVs to fly completely autonomously or within a predefined flight path for image acquisition in a photogrammetric block configuration. There are numerous factors to consider when choosing an appropriate UAV, between fixed and rotary-wing UAVs, based on their capabilities and limitations and some of these shall be discussed further in *Section 2.4.1*.

2.4 Modern Digital Photogrammetry

Schmid, in the 1950s, was one of the first few photogrammetrists to engage in digital photogrammetry as he had access to an early version of what is now a computer (Schenk, 2005). Using matrix algebra, he developed the basis of analytical photogrammetry and although over the last few decades numerous improvements have been made to his concept it still serves as a pillar in most photogrammetric algorithms today. Major advancements were made in computer vision and image matching algorithms from early

the 2000s. This, coupled with the improvements in computer components such as the reduction in size of the computer microchip while outputting more computing power, meant that more powerful computer hardware could be created which in turn meant that more powerful software could be developed to handle the requirements of producing high-resolution three-dimensional data. One of the most common techniques used in the image correlation phase of the photogrammetric process is the Area-Based Approach (ABA), as implemented in a study by Naesset (2002). The approach selects an entity to match in one image and searches for this entity throughout another image. Searching for this entity in a number of other images, possibly hundreds or thousands, is computationally intensive so techniques such as a 'whole-to-part' or 'coarse-to-fine' approach are implemented to speed up the process (Tagoe, Rüther and Smit, 2016). A Fourier transform technique is a frequently used alternative when speeding up the processing of image data (Richards J.A., 1993).

The use of computer vision algorithms and digital images captured from digital still cameras aboard Unmanned Aerial Aircraft (UAAs) is one of two modern methods developed to capture three-dimensional structures (Wallace et al., 2016), the other being the use of laser scanners. Using computer vision or photogrammetric techniques, sparse and dense point clouds can be generated from these captured images using SfM. Operating under the principles of traditional stereoscopic photogrammetry, SfM uses clearly defined geometrical features that appear in multiple images captured from multiple overlapping perspectives to create three-dimensional point cloud of the features captured in the images (Wallace et al., 2016). This is achieved, in part, with cleaver computer vision algorithms like Scale Invariant Feature Transform (SIFT) which automatically detects identical features from two different images (Bognot et al., 2018), and bundle adjustment which computes the transformation of mosaicked images based on the Ground Control Points (GCPs), the internal relationship between overlapping images, a supplied camera model and a DEM.

Based on these advancements, it has become possible to match numerous features in hundreds to thousands of overlapping images captured from multiple perspectives to create a richly populated dense point cloud. This ability places the use of UAV_{SfM} in a position along a technology or technique scale that provides a cheaper to access technology than aerial laser scanning which outputs highly precise data but at a high cost

while providing better spatial resolution data compared to freely accessible satellite imagery or RADAR, or slightly pricier high-altitude aerial photogrammetry as in *Figure 2.6* below. This makes the use of SfM particularly useful for processing images acquired from small lightweight fixed-wing or rotary-wing UAVs in modern day photogrammetry.

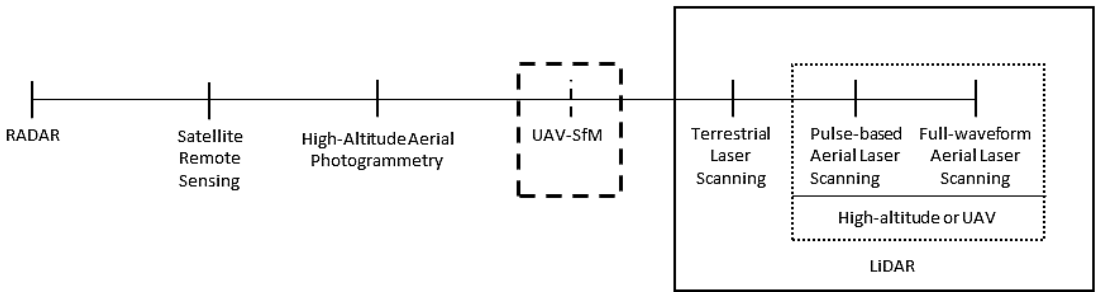

Figure 2.6 | *Technique scale that places UAV_{SfM} in line with other biomass estimation in Photogrammetry and Remote Sensing (PaRS)*

The scale highlights the possible data quality expectation of the various techniques from low to high spatial resolution, RADAR to LiDAR, and inversely highlights the cost of data from costly to low-cost, LiDAR to RADAR.

2.4.1 Fixed-wing and rotary-wing UAVs

The choice between fixed-wing and rotary-wing UAVs for an aerial photogrammetry flight mission are usually dependant on several factors which include but are not limited to weather conditions, scale of project, various flight parameters, need for manoeuvrability in the environment and in some cases, cost. Notably, fixed-wing UAVs are capable of longer sustained flight but suffer from focused, extensive coverage of the site (Fraser and Congalton, 2018), and while rotary-wing UAVs may have the ability to hover and obtain location-specific aerial imagery they subsequently suffer from rapid battery drain. Choosing the appropriate UAV for an aerial mission is crucial. *Table 2.2* below shows some notable differences between the two platforms. Some of the most common examples of fixed-wing UAVs used in FMIs and other research include the Sensefly eBee (Sensefly Ltd, 2014) (*Figure 2.7a*), while for rotary-wing UAVs the DJI Phantom 3 (DJI, 2017a) (*Figure 2.7b*) and the DJI Phantom 4/Pro (DJI, 2017b) (*Figure 3.2*).

Figure 2.7 | *Examples of common commercially available UAVs. (a) A Sensefly eBee UAV (Sensefly Ltd, 2014), and (b) a DJI Phantom 3 Professional UAV* (DJI, 2017a)

Table 2.2 | *General differences between fixed-wing and rotary-wing UAVs for aerial imagery acquisition*

Fixed-wing UAV	Rotary-wing UAV
Requires a runway (approximately 3 m – 5 m) or a mechanised launching sling to project aircraft into air. some models need to be tossed physically forward to initiate flight system.	Also called Vertical Take Off and Landing (VTOL) – Does not need a runway and can take off vertically from a limited area, which is ideal where multiple obstructions are immediately present.
Can fly at much higher altitudes.	Lacks the power to fly at higher altitudes.
On average, they are capable of longer sustained flight (>30 minutes).	Susceptible to reduced flight times on average (<30 minutes).
Unable to hover over specified locations and so they have to perform extensive coverage.	Able to hover and acquire images at specified locations.
Unable to manoeuvre easily between obstacles at lower altitudes.	Able to manoeuvre easily at lower altitudes and in between obstacles.
Fixed-wing UAVs can also carry a larger payload like heavier sensors.	These platforms often handle lighter payloads and are often retrofitted with low-cost and lighter sensors.

Some of the biggest advantages to modern UAVs equipped with low-cost but powerful camera sensors exist in their spatial and temporal resolution (Lisein et al., 2013). When flown at relatively low altitudes UAVs have a spatial resolution in the region of sub-centimetre GSD with incredible detail; and a temporal resolution or revisit period equivalent to however much battery life there is available to make another pass or flight over the study area. They can also be flown at higher altitudes to cater to scale, depending

on whatever phenomenon is to be captured. Images captured also add quality and beneficial information to the data such as texture, which can be a valuable attribute when discerning features. In addition to these, their lightweight and compact nature make most UAVs an ideal and versatile tool for studying phenomena where access is incredibly challenging for a terrestrial approach. The rising popularity of these UAVs has made dense and sparse three-dimensional reconstruction of objects or environments possible through combining the principles of photogrammetry and SfM technology into what is now commonly referred to as 'Structure-from-Motion Photogrammetry'.

Because of the nature of the study sites assessed in this research, the need for manoeuvrability around the forest structures assessed (study areas discussed in Chapter 3) and the objectives outlined in Chapter 1, a rotary-wing UAV is the more appropriate choice for the study and is referred to as the UAV of choice in further chapters. The specific make and model, along with specifications, of the rotary-wing UAV used in this research is extensively discussed further in Chapter 4.

2.4.2 Unmanned Aerial Vehicles in Mapping Forest Variables

Very extensive literature exists on the application of UAVs in biomass estimation, mapping forest variables and forest monitoring. Typically, low altitude UAV imagery is used to assess or estimate forest canopy height, which are a great interest for the estimation of carbon stocks or forest biomass (Lisein et al., 2013). As in the case with biomass estimation, several forest or individual tree attributes can be measured and entered into a regression model as independent variables to ascertain which variables in the model affect biomass the greatest and in most cases calculate individual tree biomass (Jones et al., 2007). In comparison to the use of photogrammetric UAV imagery, several studies over the years have documented excellent results obtained from UAVs equipped with LiDAR sensors that produce a dense georeferenced point cloud. These studies generally document LiDAR's superiority to digital photogrammetric point cloud data. The ability of LiDAR to penetrate forested areas and provide multiple returned signals of the forest floor and other structures allows for the generation of DTMs, DSMs, and the estimation of other forest variables much more easily and effectively than with photogrammetric point cloud data (Lim et al., 2003; Lisein et al., 2013; Brede et al., 2017).

Studies such as Brede et al. (2017) and Lisein et al. (2013) argue strongly that UAV imagery is inappropriate for the determination of forest canopy heights owing to their vast limitations, chiefly their challenge in penetrating above-canopy structures to acquire enough below-canopy ground or terrain information to produce a DTM. A limitation most evident in densely populated forest structures. Limitations in the technique also arise in image matching when mapping areas of high vegetation due to insufficient image coverage of the area; repetitive or monotonous textures; and multi-layered forest structures, or even moving objects like swaying trees (Lisein et al., 2013). The sudden changes in tree crowns caused by change in relief cause multiple omissions that disrupt the image matching process as well. Although these limitations exist and are notable, several studies have reportedly produced digital canopy surface models using photogrammetric methods with satisfactory levels of results in resolution and accuracy (St-Onge et al., 2008). One of the key characteristics of UAV imagery that makes that possible is its high image overlap, which provides a rich view from multiple overlapping perspectives of the structures in the images. This therefore has the potential to accurately and adequately model forest canopy surfaces at a very high temporal, spectral and spatial resolution (Wallace et al., 2016), thus providing relatively accurate estimates of forest variables with metrics.

A study conducted by Kachamba et al. (2016b) used UAS derived point cloud data to estimate the biomass of Miombo woodlands in Malawi. This was achieved by obtaining point cloud data after applying SfM and stereo-imaging algorithms for image alignment and multi-view stereo reconstruction to images acquired from a Sensefly eBee fixed-wing UAV (Sensefly Ltd, 2014) flown at 325 m above ground level (AGL). The images captured were 16.1 Megapixel images consisting of red, green and blue spectral bands. SfM processing was done in Agisoft Photoscan Professional software v1.1.0 (www.agisoft.com) (Agisoft, 2015). Fourteen different DTMs of the Miombo woodlands were generated using different ground filtering methods; and individual tree heights were then extracted from the DTMs and used as independent variables in a regression model to estimate AGB. Although DTMs generally refer to above ground structure-free models of the terrain, and DSMs refer to models of the terrain inclusive of structures, in the models presented by the study, the terms are reversed - DTMs comprise of a structure-inclusive terrain and DSMs comprise of a structure-free terrain.

The study discovered very little deviation (p = 0.985) between the DTM heights when individual tree positions were measured in the models, except for the model based on Shuttle Radar Topography Mission (SRTM) which showed significant differences in the heights measured. This can be attributed to random errors in heights that is characteristic of SRTM data (Kachamba et al., 2016b), making DTMs sourced from this model inaccurate for the determination of AGB. The most optimal model, according to the study, that yielded significantly accurate tree heights when measured was a model developed using unsupervised ground filtering based on a grid search approach, which had a root mean square error (RMSE) of 46.7% and a mean biomass value of 38.99 Mg/ha.

Tree Canopy Height (TCH) is a common variable in most allometric equations; as such, the production of a Normalised Difference Terrain Model (NDTM) or CHM, which is the elevation difference between a DSM and DTM, is quite popular. Relatively high accuracy was obtained in a study conducted by Mohan et al. (2017) in a mixed conifer forest where the applicability of low grade consumer cameras attached to a UAV and the use of SfM algorithms could automatically perform Individual Tree Detection (ITD) using a local-maxima based algorithm on UAV-derived CHMs was investigated. Images were acquired using a DJI Phantom 3 quadcopter fitted with a 12.1 Megapixel PowerShot S100 RGB sensor flown at 115.29 m AGL. The point cloud data was generated using Agisoft Photoscan Professional software v1.0.0 (www.agisoft.com) (Mohan et al., 2017). The study implemented individual tree detection algorithms on the UAV_{SfM} derived CHM to automatically detect the treetops of 358 trees out of a total manually counted 367 trees resulting in an accuracy of (F > 0.80). The study concludes that UAV_{SfM} is a suitable alternative to LiDAR to capture data and produce adequate CHMs for ITD and for the extraction of individual tree heights to be used in biomass regression models.

In a publication of a study based on boreal forests, Puliti et al. (2015) showed the use of UAV_{SfM} derived variables in comparison to both field acquired variables and LiDAR derived variables. LiDAR data was acquired using an Optech ALTM-Gemini laser scanner mounted on a Piper Navajo fixed-wing aircraft. The acquired LiDAR point density was 7.45 points/m^2; whereas the UAV_{SfM} imagery was acquired using a Sensfly eBee fixed-wing UAV (Sensefly Ltd, 2014) fitted with a 12.1 Megapixel Canon PowerShot S110 near-infrared camera (Puliti et al., 2015) and flown at 120 m AGL. Point cloud data for this study was generated using

Agisoft Photoscan Professional software v1.1.0 (www.agisoft.com) (Agisoft, 2015). Images produced consisted of red, green and near-infrared spectral bands.

Due to the limitations in UAV_{SfM} in penetrating top-canopy forests to acquire enough ground imagery to produce ground points in the SfM process ALS data was used. The ALS data was classified, and the ground points were used to create a Triangulated Irregular Network (TIN). This formed the DTM. A DSM was produced using the unclassified UAV_{SfM} points, and the absolute heights of the trees were extracted from the normalised model. Variables included Lorey's Mean Height (hL), Dominant Height (hdom), Stem Number (N), Basal Area (G) and Stem Volume (V). Results were able to show relatively fair to excellent correlations between the two datasets. Correlations of R^2 = 0.71, R^2 = 0.97, R^2 = 0.60, R^2 = 0.60 and R^2 = 0.85 existed for variables (hL), (hdom), (N), (G) and (V) respectively. Their respective mean predicted values also did not differ much from the mean reference values.

Another study by Iizuka et al. (2018) attempted to estimate Japanese Cypress (*Chamaecyparis obtusa*) tree height and diameter at breast height from digital surface models and orthophotos using UAV_{SfM} imagery, and comparing the acquired values to in situ manually measured field measurements. UAV_{SfM} imagery was captured using a DJI Phantom 4 Pro quadcopter UAV (DJI, 2017b) equipped with a 20 Megapixel RGB sensor and flown at 110 m AGL. The images were then processed in Agisoft Photoscan Professional software v1.3.1 (www.agisoft.com) (Agisoft, 2017). A three-dimensional point cloud of the forest structure was created, so were DSMs and DTMs, as well as orthophotos of the study area. To obtain individual TH of the individual trees in the area CHM was calculated by subtracting the DTM from the DSM (Iizuka et al., 2018). These were compared to actual field measured data. Estimating DBH followed a more complicated procedure. Canopy width and area were measured from the orthophotos and recorded, then regression models were created using the orthophoto-extracted canopy width, canopy area and field measured DBH. The regression model was created to see how well canopy structures could predict DBH.

The study however produced a RMSE of 1.712 m or R^2 = 0.2076 when estimating the relationship between estimated and observed TH, but R^2 = 0.7786 when estimating the relationship between canopy width and DBH, and R^2 = 0.7923 when estimating the relationship between canopy area and DBH.

A 2016 study in Portugal attempted to estimate tree variables such as tree position, crown diameter and tree height in *Pinus pinea L*. at the individual tree level (Guerra-Hernández et al., 2016) using low-cost UAV imagery. The study used images acquired from a Sensefly eBee fixed-wing UAV (Sensefly Ltd, 2014) equipped with a 12.1 Megapixel Canon PowerShot S110 RGB camera, and flown at 170 m AGL. The site was flown using double grids to maximise the possibility of covering the entire site from multiple perspectives and improve accuracy. Pix4DMapper software (www.pix4d.com) (Pix4Dcapture, 2019a) was used to produce an orthomosaic, the DSM and the DTM for the study area. Tree heights in the study were measured using a Vertex III hypsometer, to be compared to the UAV_{SfM} CHM derived tree height. The CHM from which the tree heights were extracted from was produced using a modified version of the mixed pixel-and region-based algorithm designed and implemented in a 2013 study by Guerra-Hernández et al. (2016).

Excellent correlation was achieved when field measured, and image derived tree heights were compared with a correlation of R^2 = 0.810 with a RMSE of 4.56%; while crown diameter had a correlation of R^2 = 0.950 with a RMSE of 6.14%. The study concluded that high resolution UAV_{SfM} imagery could accurately play a role in estimating tree variables at the individual tree level for *Pinus pinea L*. trees, but especially so in areas with sparsely populated trees.

CHAPTER 3

Data and Study Area

3.1 Data

Most countries rely almost extensively on their national FMIs for substantial data on forest coverage; biodiversity and forest species variation; forest tree variables such as tree count, basal area, tree height and tree dimeter for the various plant species in their homogeneous and heterogeneous forests (St-Onge et al., 2008; García et al., 2010; Gonzalez et al., 2010; Simonson et al., 2016b; Olofsson and Holmgren, 2017). These large datasets are created and managed by several interested parties concerned with forest management inventories and are limited, or empowered, by their roles and/or responsibilities. The interested parties are a combination of private and government entities, which form two categories namely business-sensitive and proprietary forest inventory data (Dovey, 2014), each with their unique agendas and procedures for acquiring and curating this data. Scientific knowledge and data is also present but owned, in part, by private and academic institutions (Dovey, 2014). Information is therefore very limited to public access. In South Africa, the Department of Agriculture, Forestry and Fisheries (DAFF) is the legal and national custodian of South Africa's forest resources, which spans over 40 million ha of South Africa's total land surface area, but shares the custody of some of the data and information with the Department of Environmental Affairs (DEA) (Dovey, 2014). According to the National Forestry Act (RSA, Act 84 of 1998):

"The minister must carry out or commission research, the research must promote the objectives of forest policy and conform with national policies and programmes related to science and technology. The minister must monitor forests and disseminate the information derived from monitoring to the public in a way that will promote sustainable forest management"

Whereas the DAFF is responsible for the management of forestry data, other entities, both private and public, possess and disseminate forestry data at different levels and in different forms. This gives rise to challenges in acquisition or access to such data, various data formats, format compatibility, redundant data, or simply absence of relevant or useful

data. Another contributing challenge to data access or acquisition that is particularly sensitive to the nature of this research endeavour is the general growing restriction on the use or operation of Remotely Piloted Aircraft Systems (RPAS) (Colomina and Molina, 2014). Due to the constraints mentioned, and the nature of this research undertaking, more weight is on the use of primary data – field acquired data – than on secondary data.

Remotely sensed biomass and carbon stocks estimation is currently, in South Africa, performed on a large scale using medium to high resolution satellite imagery and field methods to produce land cover maps or statistics (Dovey, 2014). According to the 2006 IPCC Guidelines for Carbon Accounting this is a Tier 1 approach (IPCC, 2006) that uses simple methods and default estimation parameters based on these land cover maps that display change in land use (Dovey, 2014), methods that are arduous and time consuming.

When using active-sensor remote sensing techniques like LiDAR and aerial photography in biomass or carbon stocks estimation, biomass is estimated by using tree variables like TH and tree diameter, by method of DBH derived from acquired three-dimensional photogrammetric point cloud or LiDAR data, to produce the necessary models like biomass regression models, or elevation models like DSMs, DTMs and CHMs (Kachamba et al., 2016; Moore, 2010; Lisein et al., 2013; Kumar and Mutanga, 2017). Low to medium point density LiDAR data is often collected during extensive and expensive national expeditions, along with imagery captured using medium to large format cameras to add textural information to the produced orthomosaic, as is now common practice in conventional photogrammetry aboard most high-altitude aircraft (Colomina and Molina, 2014). This is especially common for national development programmes. Though the LiDAR data collected during these expeditions is not primarily used for biomass estimation, in part due to its coarse spatial resolution, it can provide subpar, but comparative, data for estimation when compared to field estimates or estimates that are products of other remote sensing techniques. The use of low altitude UAV photogrammetric data in biomass estimation requires essentially one dataset – photographic imagery acquired from a UAV. However, to compare its results to other techniques and technologies; and assess its accuracies and suitability for biomass estimation, several datasets for various techniques are required.

Below in *Table 3.1* is summarised both the primary and secondary data utilised in this dissertation. Since the research investigates the comparative results of photogrammetric

point cloud to LiDAR, no satellite imagery is used for analysis, but rather for base maps where necessary.

Table 3.1 | *Summary of datasets used in this research*

Data	Source	Notes
DJI Phantom 4 Pro 20MP 5472 x 3648 pixel Nadir and Oblique RGB imagery	DJI Phantom 4 Pro quadcopter www.dji.com/phantom-4-pro (DJI, 2017b)	Nadir, oblique and façade RGB imagery acquired at all study sites between 20 m AGL - 100 m AGL, 0.55 cm/px – 2.73 cm/px GSD, 90% overlap and 80% sidelap (Domingo et al., 2019) between June 2018 and October 2019
DJI Matrice 600 + Riegl miniVUX®-1UAV LiDAR data	Horts Geo-Solutions www.horts-solutions.com	ALS LiDAR data of the heterogeneous forest structure at the UCT study site with GSD of 240.73 points/m^2
High-Altitude low-resolution aerial laser scanning LiDAR data	UCT/CoCT	ALS LiDAR data of the City of Cape Town, 5 km by 5 km grid, measuring 25 km^2, 5.537 points/m^2 acquired in July 2017
Z+F Imager® 5010X laser scanner LiDAR data	Z+F Imager® 5010X laser scanner supplied by UCT	Field surveyed TLS LiDAR data of the heterogeneous forest structure at the UCT study site, 55 122 points/m^2 acquired in May 2019
GCP coordinates	Trimble R8 DGPS Base + Receiver GNSS supplied by UCT	XYZ coordinates of GCPs placed at the study sites, measured, and recorded with a Trimble R8 DGPS in the Hartebeesthoek 1994 coordinate system between June 2018 and October 2019
Diameter at Breast Height field measurements	Rondebosch Common *Pinus pinea* population	30 odd samples of tree diameters using Diameter at Breast Height method, measured, and recorded in cm from trees in the Rondebosch Common Park

3.2 Criteria for Tree Selection and Categorising

Vegetation with a DBH of ≥5 cm are typically regarded as a trees (Theron et al., 2004; Kachamba et al., 2016b) that have *merchantable* or *commercial* volume (Pommerening, 2007) with regards to biomass and are worth recording. In this study, they are categorised as High Vegetation, while vegetation that has a stem or trunk with a DBH of ≤4.999 cm is classified as 'Medium Vegetation'. Grass is categorised as 'Low Vegetation'. The criteria for selecting the trees to be physically measured with a tape and the category they are categorised in when recorded during the field expeditions is illustrated briefly by the flow chart in *Figure 3.1* below. Two categories therefore need to exit for the categorisation of all recorded trees in the research, High Vegetation and Medium Vegetation; and one category for grass. The same tree selection and categorising procedure is necessary for trees assessed in the TLS LiDAR data obtained in field expeditions, ALS LiDAR data obtained from CoCT/UCT and the UAV_{SfM} point cloud in the analysis stage. The classification, selection, and categorisation of the trees in these various datasets are discussed further in Chapter 4.

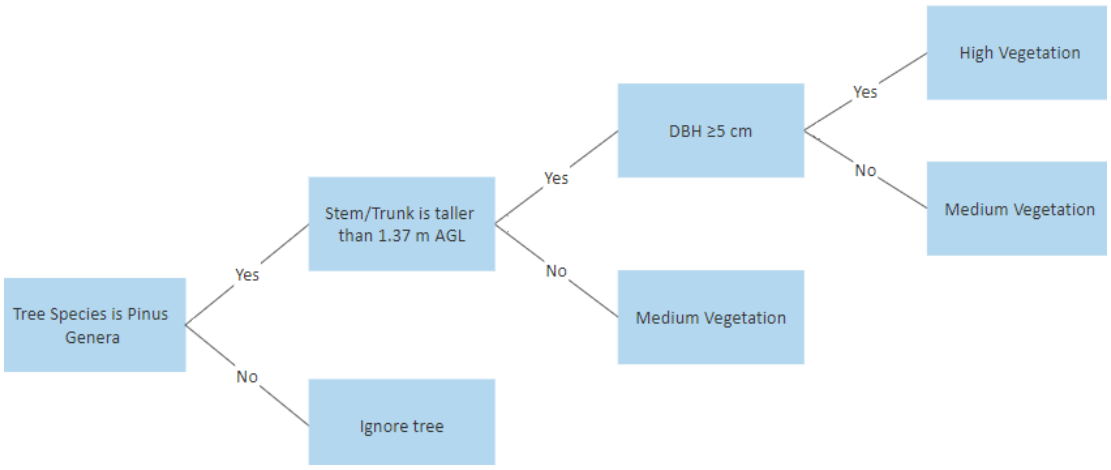

Figure 3.1 | *Decision tree showing criteria for selection of trees to be measured and recorded using field methods.*

3.3 High-Altitude Aerial Laser Scanning LiDAR Data

For this research three ALS LiDAR datasets are acquired from the City of Cape Town through the University of Cape Town - block W08A, block W45C, and block W55D. These datasets are required to provide comparative data to photogrammetric data and test

whether UAV_{SfM} data can yield comparatively accurate measurements of tree variables as ALS data can. Variables to be extracted from ALS data are TH, and where possible, DBH.

All three LiDAR datasets were captured as part of an aerial laser scanning mission over the city of Cape Town during the month of July 2017. Each acquired dataset comprises of a 5 km by 5 km grid spanning 25 km^2, with a point density of 5.537 points/m^2. The criteria for the selection of aerial data from the City of Cape Town and its inclusion in this research is factored by four conditions:

1. Point density – Typically CHMs are derived from the DEMs and DSMs produced using the acquired ALS_{LiDAR} data. This is used for Individual Tree Detection (ITD) and subsequent extraction of TH. To adequately achieve this the acquired ALS point cloud needs to have a point density of at least 5 points/m^2 (Tanhuanpää, Saarinen, Kankare et al., 2017).
2. Availability – The data must also be available to access with minimal limitations to its use thereafter.
3. Recent data – Since the research investigates vegetation, the data must be within an acceptable time period. For this research, it is decided that the data need not be older than three years from the year of the research undertaking. This should ensure that not too much variance should exist between the THs of the trees captured due to growth when measuring THs from both ALS_{LiDAR} and UAV_{SfM} photogrammetric datasets, as sample trees are mature and have been in existence for some time.
4. Coverage of the study areas – Each block, or a combination of blocks, acquired needs to encompass completely the respective study areas, or a combination of study areas, sufficiently in order to satisfy the conditions for producing a CHM for the study areas.

The acquired ALS_{LiDAR} data is post-processed from aircraft trajectory information and the raw laser data captured from an on-board laser scanner. These are processed to provide geocoded LAS files, which undergo initial classification into ground and non-ground points, processed for calibration uncertainties, x, y and z fluctuations, and then final ground is classified. The data received is in a *.las* format and ready to be classified further or used to produce DEMs and DSMs. Ideally, these LAS files would be ready for feature measurement

extraction if the data has already been further classified to include a vegetation class, and vegetation sub-classes (classes like low, medium or high vegetation; or classes by vegetation species) but this remains a challenge when classifying large urban and built-up areas that comprise of structures like houses and other buildings; and objects like cars and street furniture etc. However, since this data is initially acquired primarily to produce DTMs and topographic or contour maps, and not necessarily for vegetation detection, analysis and mapping amongst others, classifying ground points is a much easier process. The LAS files obtained from the CoCT through UCT are pre-classified into the classes indicated below in *Table 3.2*.

Table 3.2 | *Initial LAS data Classification of blocks W08A, W45C and W55D*

Classification Code	Class
1	Unclassified
2	Ground
3	Low Point (Noise)
4	Water
5	Overlap

Obtaining vegetative structures from which to attempt measuring TH and DBH in the available LiDAR data therefore requires either the entire dataset to be reclassified, in the case that the initial classification misclassified some points that visually resemble vegetation due to their positions within the cloud, or the 'Unclassified' points in the dataset need to be reclassified to create distinct vegetation points under the sub-classes: 'High Vegetation', 'Medium Vegetation' and 'Low Vegetation', as the inclusion of unnecessary points misclassified either as ground or vegetation could skew the resulting terrain model which needs to be accurate for the purpose of variable extraction for biomass estimations (Kachamba et al., 2016b). The classification methods and procedures carried out on this dataset are discussed further in Chapter 4.

3.4 DJI Phantom 4 Pro Quadcopter RGB Imagery

To achieve reasonably accurate results when using structure-from-motion and stereo-matching software that use the photogrammetric approach to model three-dimensional

data (Kachamba et al., 2016b) numerous images must be captured from multiple perspectives to create adequate stereo-pairs. These images are captured at all three study areas to create their respective photogrammetric point cloud data to compare to LiDAR data acquired for the three study areas. The UAV chosen and used for capturing the necessary RGB imagery for the UAV_{SfM} aspect of the research to produce the comparative photogrammetric data is the DJI Phantom 4 Pro (www.dji.com/phantom-4-pro) (DJI, 2017b). The drone is equipped with a 20 Megapixel RGB sensor that has an image resolution of 5472 x 3648 pixels in each channel.

Figure 3.2 | *DJI Phantom 4 Pro Quadcopter* (DJI, 2017b)

This particular quadcopter is chosen for numerous reasons including its high resolution image sensor relative to overall frame size, its ability to hover in position when capturing façade imagery (Carnevali et al., 2018); its ease of manoeuvrability when capturing oblique imagery, the inclusion of a high resolution 20 Megapixel RGB camera, as well as a mechanical shutter that is more suitable than an electronic rolling shutter for capturing vegetation that is in constant motion (Topodrone, 2021). The specifications of the on-board camera/RGB sensor are provided in *Table 3.3* below.

Table 3.3 | *Specifications of DJI Phantom 4 Pro UAV*

Camera Features	
Sensor	1” CMOS
Maximum Image Size	5472 x 3648 pixels
Sensor Size	13.2 mm x 8.8 mm
Pixel Size	2.4 µm
Focal Length	8.8 mm

To meet the requirements for the adequate three-dimensional reconstruction of a scene using photogrammetric structure from motion techniques, images captured need to meet several conditions -

1. Images must be captured with a forward overlap of between 60-90% and a side overlap between 30-60%. This ensures that the photogrammetric model has sufficient data when modelling the forest floor or gaps in the forest canopy (Dandois, Olano and Ellis, 2015), as well as enough common features between images to create accurate stereo pairs.
2. A Double-Grid approach must be flown when capturing Nadir (90˚) UAV imagery. The inclusion of images flown North-South and East-West ensures that imagery of the forest canopy, as well as gaps in between, are captured from multiple perspectives. This should render a rich and densely populated model.
3. GSD or image spatial resolution, coverage and even flight duration are all direct functions of altitude AGL (Mesas-Carrascosa et al., 2015). As such, for this research, images must be captured at flight heights that ensure a GSD that allows the identification of features in at least four pixels because in general this is the least number of pixels necessary to identify the smallest object in a captured image (Mesas-Carrascosa et al., 2015). This ensures that features in the image are easily identifiable during the feature matching phase, as well as to provide distinct features to identify clearly and mark as GCPs.
4. To ensure maximum coverage of each study site from multiple perspectives and recreate a three-dimensional point cloud, where necessary, oblique (30˚-45˚) images need to be captured from varying heights.

3.5 DJI Matrice 600 and Riegl MiniVUX®-1UAV LiDAR Data

To test the ability of UAV_{SfM} to accurately model TH and, where possible, DBH and subsequently provide measurements from the photogrammetric point cloud data to estimate tree biomass it is compared to several LiDAR datasets and techniques. In addition to the high-altitude LiDAR data obtained from the CoCT, as well as the terrestrial laser scanning LiDAR data obtained from the Z+F Imager® 5010X, low-altitude LiDAR data acquired from an unmanned aerial vehicle equipped with a laser scanner is also assessed to

compare the accuracy of the UAV_{SfM} dataset, hereon referred to as UAV_{ALS}. The UAV_{ALS} LiDAR data used in this research is acquired from Horts Geo-Solutions (www.horts-solutions.com) and is captured using a DJI Matrice 600 Pro (DJI, 2020) (www.dji.com) with a Riegl miniVUX®-1UAV (*Figure 3.3* below), a survey-grade full waveform laser scanner (RIEGL Laser Measurement Systems GmbH, Horn, Austria) (www.riegl.com).

Figure 3.3 | *DJI Matrice 600 Pro hexacopter UAV* (DJI, 2020)*, and the Riegl miniVUX®-1UAV full waveform LiDAR sensor* (Riegl, 2020)

The UAV_{ALS} data was captured over the University of Cape Town on the 20th of August 2018. The dataset covers an area of 1 084 000 m^2, comprises of 63 377 238 points, and has a point density of 240.73 points/m^2. The data obtained is an un-georeferenced, uncoloured and unclassified LiDAR point cloud in .e57 file format. This data was chosen as it was readily available and is used as a comparison for the UAV_{SfM} TH and DBH trees variables at the UCT study area. The procedure to be followed when processing and classifying the data is discussed in further detail in Chapter 4, however, the specifications of the equipped Riegl miniVUX®-1UAV Laser Scanner are provided in *Table 3.4* below.

Table 3.4 | *Specifications of Riegl miniVUX®-1UAV Laser Scanner*

Characteristics	
Maximum effective measurement rate (kHz)	100
Maximum Pulse Repetition Rate (PRR) (kHz)	100
Minimum|Maximum range (m)	3|330
Laser wavelength (nm)	1550 (near infrared)
Accuracy|Precision (mm)	15|10
Beam divergence (mrad)	1.6 x 0.5
Weight (kg) [1]	1.60

[1] with cooling fan.

3.6 Z+F Imager® 5010X laser scanner LiDAR Data

Measurements of tree variables at the UCT study area derived from TLS LiDAR data, hereon referred to as TLS_{LiDAR}, are required as a comparison for the UAV_{SfM} photogrammetric point cloud derived tree variables. To accomplish this, LiDAR data of the heterogenous forest structure at the UCT study area is acquired during a field survey. The TLS_{LiDAR} acquired provides the basis to compare UAV_{SfM} results to high-altitude LiDAR data, UAV_{ALS} and TLS_{LiDAR}. The TLS_{LiDAR} data used in this research is captured using a Z+F Imager® 5010X Laser Scanner (Zoller + Fröhlich GmbH, Wangen, Germany) (www.zf-laser.com) (Zoller + Fröhlich, 2020a) (*Figure 3.4* below) supplied by the UCT for three reasons –

1. The laser scanner comes equipped with an RGB sensor which captures images in a panoramic view. These images can be used to colourise the LiDAR data acquired.
2. The system uses the built-in GPS and IMU to estimate the scanner's position and orientation at each setup. This helps the registration software Z+F LaserControl® Scout (Zoller + Fröhlich, 2020b) to register the scans before and after each setup.
3. Availability of, and ease of access to, instrument.

Figure 3.4 | *Z+F Imager® 5010X Terrestrial Laser Scanner (Zoller + Fröhlich, 2020a)*

The TLS_{LiDAR} data was captured at the University of Cape Town study area on the 12th of May 2019. The dataset covers an area of 0.01265 km^2, comprises of 103 337 988 points,

and has a point density of 55 122 points/m^2. The data obtained is an un-georeferenced, uncoloured and unclassified LiDAR point cloud in .e57 file format. The procedure to be followed when processing and classifying the data is discussed in further detail in Chapter 4, however, the specifications of the Z+F Imager® 5010X Laser Scanner is provided in *Table 3.5* below.

Table 3.5 | *Specifications of Z+F Imager® 5010X Laser Scanner*

Laser System Characteristics	
Beam divergence (mrad)	< 0.3
Beam Dimeter	approximately 3.5 mm
Minimum distance	0.3 m
Range	187.3 m
Data acquisition rate	Maximum of 1.016 million points/sec
Resolution range	0.1 mm
Linearity error	≤ 1 mm

3.7 Ground Control Points (GCPs)

GCPs are not only especially useful for georeferencing the resulting orthomosaic or ortho-rectified images, but affect the spatial accuracy of the ortho-rectified images based on the distribution and number of GCPs (Mesas-Carrascosa et al., 2015). For this research, GCPs are required to help georeference the images and position the resulting photogrammetric point cloud and acquired LiDAR data for the three study areas on the National Coordinate Reference System, Hartebeesthoek 1994, as well as improve the spatial accuracy of the ortho-rectified images captured. GCPs are also acquired to help register various scans acquired from numerous scan positions during the TLS survey. GCPs must be easily identifiable in imagery acquired from selected flying altitudes, in the case of photogrammetric surveys, and from scan positions during the terrestrial laser scanning survey. As such, these GCPs must take the form of either distinct markers placed on the ground or a surface or must be distinct features located within the immediate environment.

For the aerial photogrammetry missions, the coordinates for the GCPs are measured using a Trimble R8 DGPS Base and Rover GNSS with limits of accuracy set to 0.030 cm on both the

X and Y coordinates, and 0.050 cm on the Z coordinate. This ensures that any GCP is recorded to an accuracy that matches the spatial resolution of the images acquired, which ensures a high accuracy when refining the GCP positions in the photogrammetry software during processing.

3.8 Description of the study areas

The three study areas chosen for this research project are located in Cape Town, which lies along the Western coastline of South Africa at latitude 33°55'33.0" S and longitude 18°25'23.6" E. Cape Town is chosen because of its unique climate in comparison to the rest of the country. It has a winter rainfall Mediterranean climate compared to the subtropical summer rainfall climate experienced by the rest of the country (Tuswa et al., 2019). This makes Cape Town, and the Western Cape as a whole, a unique location for the growth of several vegetation types, including woody homogeneous and heterogeneous *Pinus* forest structures, that are unique to this region of South Africa, and the world as *Pinus* species prefer to grow in Mediterranean climates. Figure 3.5 below shows the relative positions of the three study areas.

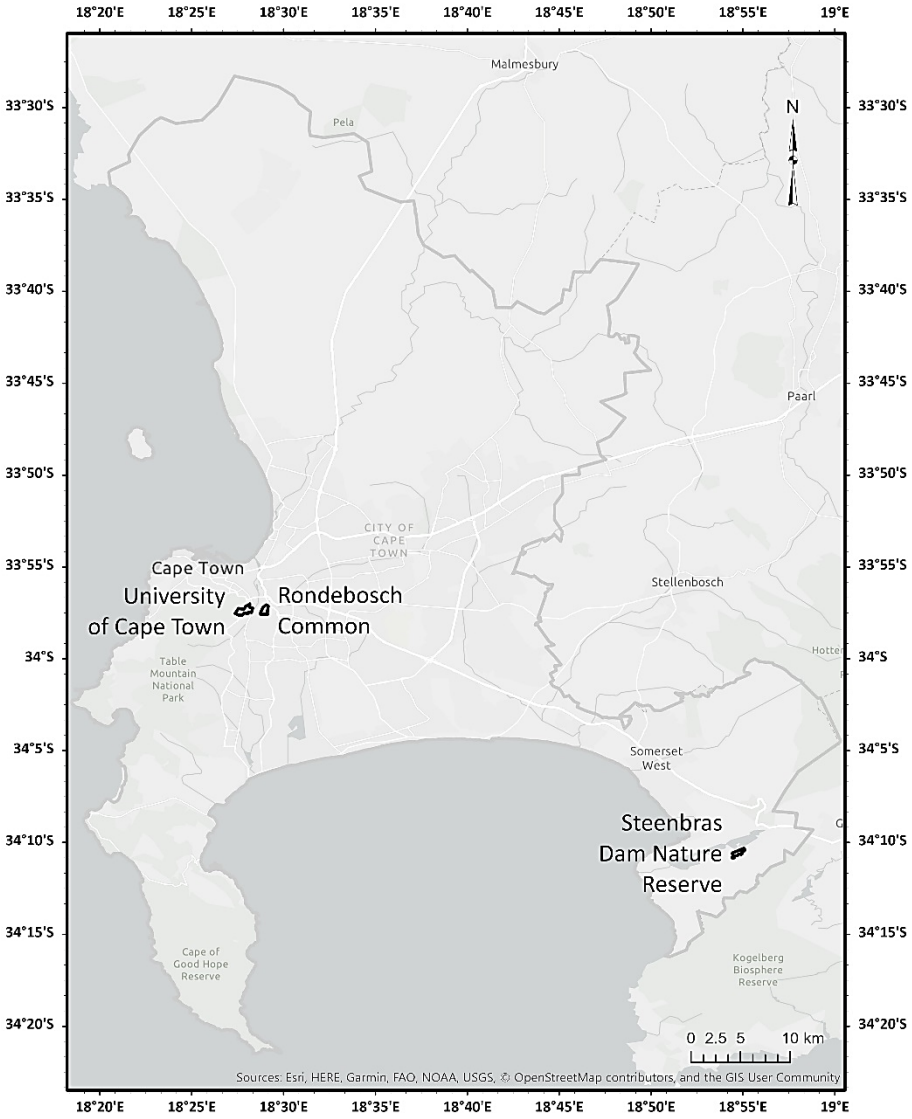

Figure 3.5 | *Study areas used in research (a) University of Cape Town (Left), (b) Rondebosch Common (right), and (c) Steenbras Dam Nature Reserve (far right)*

Land use in the area is a combination of urban areas, plantation forests, cultivated lands and natural vegetation. The area is famously dominated by Fynbos, Protea (Tuswa et al., 2019) and various tree species; but especially the *Pinus* genus, along with its various species that are located across the region and in plantation forests. *Pinus* species most commonly found in plantations and parks in the region are *Pinus pinaster* (Maritime pine), *Pinus pinea* (Stone pine) and *Pinus radiata* (Monterey pine) to name a few species; along with varying species of *Eucalyptus* and sub-species of both genera.

The study areas identified and assessed in this study vary in their structures and differ in their homogeneity and heterogeneity and are therefore intended to study the

effectiveness and accuracy of using a simple and low-cost unmanned aerial vehicle to model them using photogrammetry and structure-from-motion technology and techniques. Both homogeneous and heterogeneous *Pinus* forest structures selected in this research endeavour, as well as their locations, are discussed further in this chapter, in sections *3.9* and *3.10* respectively, however two of the study areas are grouped relatively close to one another in the south western part of the city, the Southern Suburbs, near the Table Mountain National Park, while the other lies further south east of the city close to the Kogelberg Biosphere Reserve.

3.9 Homogeneous Forest Structures

The homogeneous forest structure selected and studied in this research is located at the Rondebosch Common Park in Rondebosch, Cape Town (*Figure 3.5 above*). It lies at latitude 33°57'11.99" S and longitude 18°28'59.99" E, with an elevation of approximately 20 m above mean sea level (MSL). Rondebosch Common in total measures approximately 421 897 m^2 (40 ha) and is populated but sparsely clustered trees specifically *Pinus pinea* (Stone pine), and varying populations of fynbos. The chosen study area at Rondebosch Common, measures an area of approximately 148 m by 148 m, and 21 809.36 m^2 (21 ha) in area, and contains a close but irregularly spaced cluster of over 30 individual trees varying in tree height ranging from 6 m to 21 m.

The tree species visually observed in this study area is *Pinus pinea* (Stone Pine), with no evidence of sub-species under-canopy growth. *Figure 3.6* below shows a simple map indicating the location of this area, which shall for the remainder of the document be referred to as the $H_{omo}FS$, against an RGB base map. This particular site is ideal for the study of the effectiveness of utilising UAVs in assessing homogenous forest structures because of a number of reasons chiefly being the clustered nature of the trees surrounded by bare soil and the absence of undergrowth or sub-species within the trees gaps, or around the cluster, make it possibly ideal to obtain unobstructed images from multiple perspectives of (a) the below-canopy forest structures such as tree trunks from a terrestrial view at various heights and, (b) the tree canopy, as well as some images of the below-canopy forest structures from an aerial view in either or both nadir and oblique flight patterns.

Figure 3.6 | *$H_{omo}FS$ located at Rondebosch Common, Rondebosch*

3.10 Heterogeneous Forest Structures

Inversely, to test the practicality of using UAVs in less ideal and more realistic forest environments, as opposed to the homogeneity and isolated forest clusters with ample space around the structures for low-altitude UAV flight and data capture as in the Rondebosch Common site (*Figure 3.6*), two different heterogeneous *Pinus* forest structures are assessed in this research. The first heterogeneous forest structure identified is located at the University of Cape Town, Rondebosch, at latitude 33°57'16.19" S and longitude 18°27'22.79" E, and an elevation of 175 m above MSL (*Figure 3.5* above and site map *Figure 3.7* below); while the second forest structure is located at the Steenbras Dam Nature Reserve, Gordons Bay, at latitude 34°09'46.80" S and 18°55'12.00" E, with an elevation of 400 m above MSL (*Figure 3.5* above and site map *Figure 3.8* below).

The University of Cape Town study area is for the remainder of the research referred to as $H_{etero}FS_1$, while the Steenbras Dam Nature Reserve study area is referred to as $H_{etero}FS_2$. Both sites are chosen for their relative closeness to actual forestry conditions, individually unique *Pinus* species composition and presence of sub-species or undergrowth present below-canopy that could potentially obstruct image capture of below-canopy forest structures such as tree diameter or ground.

Figure 3.7 | *$H_{etero}FS_1$ located at the University of Cape Town, Rondebosch*

$H_{etero}FS_1$, populated by *Pinus radiata* (Monterey pine), will be used to assess the application of nadir, oblique or tessellated façade imagery captured from multiple perspectives using an unmanned aerial vehicle, or a combination of all three techniques to create a dense and rich photogrammetric model of a heterogeneous forest structure with below-canopy sub-species growth. The study area also serves as the location to capture TLS_{LiDAR} and UAV_{LIDAR} data, in addition to high-altitude LiDAR data acquired, to test against the UAV_{SfM} data.

Figure 3.8 | *$H_{etero}FS_2$ located at the Steenbras Dam Nature Reserve, Gordons Bay*

The study area at the Steenbras Dam Nature Reserve, $H_{etero}FS_2$, represents true forestry conditions as it is an actual plantation primarily established to grow pine trees and eucalyptus for timber production. The dominant *Pinus* species here is *Pinus pinaster* (Maritime Pine), as the species covers over 1 076 000 m^2 (106.2 ha) of land in the forestation. Visual inspection suggests that most of the trees are mature and fully grown, however there is presence of younger trees that populate the below-canopy area.

This study area is chosen to test the use of nadir and oblique imagery obtained from varying heights in an attempt to model photogrammetric point cloud of forest situations that are not only densely populated with other same-age trees, but also younger trees and undergrowth that populate the area below-canopy. This tests the ability to extract tree variables such as DBH and TH from the rendered point cloud and DTM models respectively and estimate individual tree biomass in a challenging environment where true-forestry conditions are most likely found. Extracted variables will be compared to high-altitude LiDAR data and TLS_{LiDAR} where necessary. *Figure 3.5* above shows the study area location relative to the region, while *Figure 3.8* above shows the study area boundaries at the location.

CHAPTER 4

Research Methods

4.1 Introduction

This chapter aims to discuss the sequence of procedures necessary to assess biomass of both homogeneous and heterogeneous *Pinus* forest structures as set out in the aims and objectives listed in Chapter 1. This is achieved here by discussing, in sections, the methodological approach to assessing these respectively unique forest structures. Due to the complexity of the research and the nature of the field conditions following the reconnaissance phase of the research, it is clear the design workflow will not be straight forward and uniform for both forest structure types. However, the workflow does follow similar patterns as the ones adopted by Díaz-Varela et al. (2015), Mlambo et al. (2017), and Fraser et al. (2018), with the most significant changes being in software choices, data processing procedure, data types and point cloud derivatives. These will be discussed in full detail further in the chapter.

There are six over-all phases covered in the research methods for each of the forest structure types and follow the sequence - Reconnaissance, Fieldwork and Flight Planning, Data Capture, Data Processing and Data Analysis, as outlined in *Figure 4.1* below which shows the general workflow diagram of the research. Each of these phases is observed in the handling of both UAV_{SfM} and TLS_{LiDAR} data. However, due to limitations, the first three phases are absent in the handling of the ALS LiDAR data. This is because due to project limitations that are discussed further on in this chapter fieldwork is not possible to effectively carry out and capture the required data using this technique. Instead, accepted high-altitude ALS LiDAR data from the City of Cape Town Municipality (CoCT) and UAV_{LiDAR} data acquired by Horts Geo-Solutions (www.horts-solutions.com) is used as comparative data to assess both the DBH and TH for all forest structure types in the three study areas - $H_{omo}FS$, $H_{etero}FS_1$ and $H_{etero}FS_2$. These datasets acquired are both secondary data and are used because the cost of implementing ALS surveys solely for this project is cost ineffective and impractical, especially at the desired scale. High-altitude ALS data, UAV_{ALS} and TLS_{LiDAR} data are used as comparative data to the UAV_{SfM} because LiDAR data is generally

considered to be very reliable and accurate data for assessing forest structures (Jayathunga et al., 2018; Brede et al., 2017).

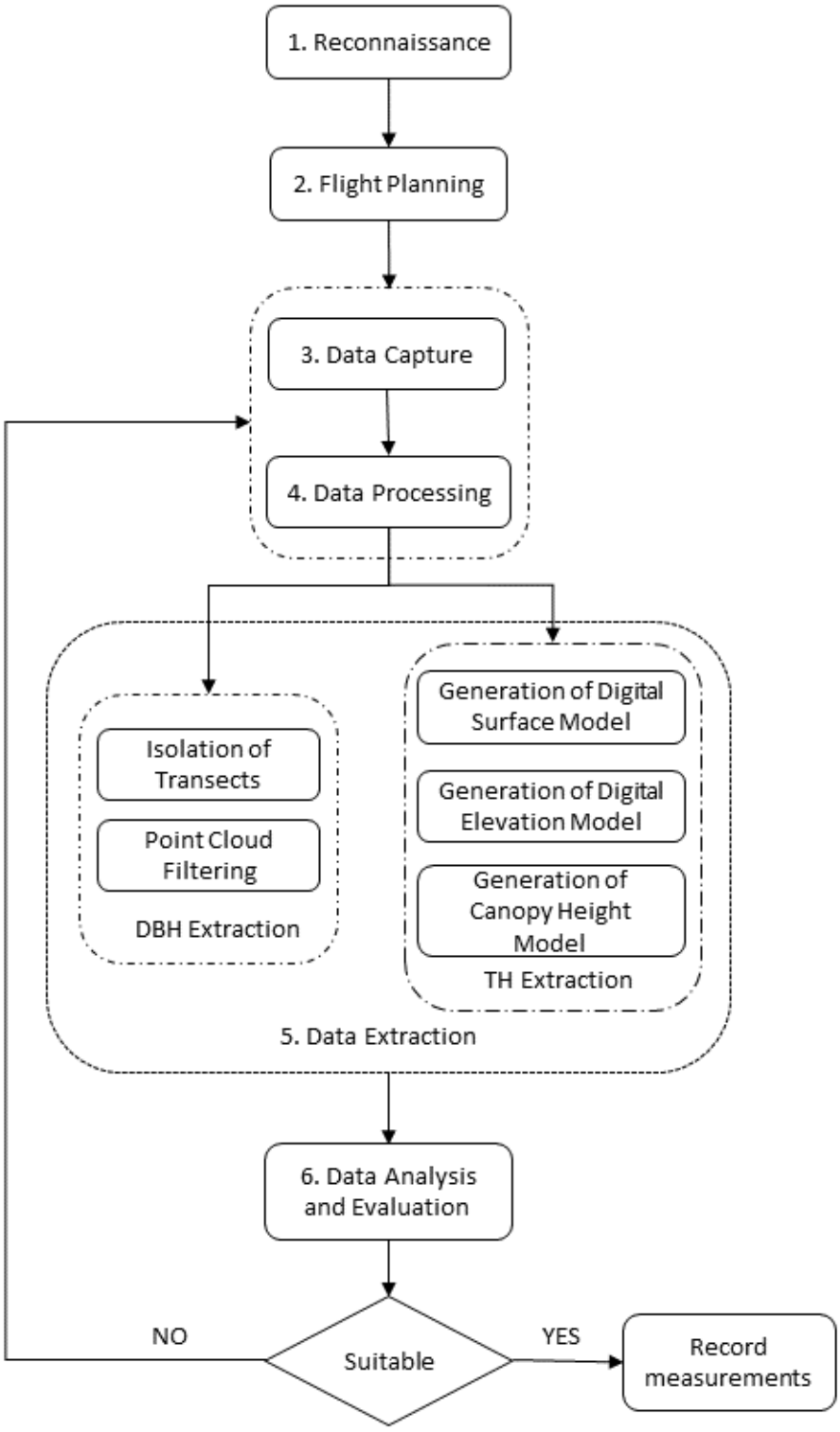

Figure 4.1 | *General workflow diagram of research*

Each dataset – UAV_{SfM}, TLS_{LiDAR} and UAV_{LiDAR} – is discussed in depth in separate sections further in the chapter, in conjunction with the involvement of each of the six phases mentioned above in their respective data collection, processing and analysis procedures.

4.2 Conventional Data Acquisition of Tree Variables for Data Comparison

Preliminary comparative data was collected at study area *$H_{omo}FS$*. The tree diameters of the easily distinguishable trees in the area were measured using conventional methods, before the aerial missions. The trees were first individually counted and since they were uniquely positioned and could easily be identified in a photograph, their GNSS coordinates were not measured. A total of thirty (30) trees were counted and numbered TR1 to TR30. Acquiring DBH data of the trees followed guidelines stipulated in *Section 3.2* and *Figure 3.1* above.

A height of 1.37 m was measured with a tape measure, from the base of the tree where the trunk meets the ground, to "breast height". This figure is standard because it is at a convenient measurement at which an individual does not need to bend or climb on a ladder to take the measurement (Agriculture, 2006). Because the study had no access to calipers that would give the direct DBH values, as was done by Meintjes et al. (2002), Kachamba et al. (2016b), and Meng et al. (2016), more rudimentary means were explored. A piece of yarn string was wrapped around each tree trunk at a height of 1.37 m from the ground. Once the yarn string reached around to the start point, it was cut and marked to indicate that that length was indicative of that specific tree, thus distinguishing it from the others. All the estimated tree DBH measurements were recorded accordingly and respectively. As this reading is the circumference of the tree and not the diameter, a simple conversion or allometric equation, that equates the relationship of the diameter of a circle to its circumference, needed to be applied to acquire the individual tree diameters. The equation used is a mathematical equation used to equate a circle's diameter to its circumference, though this can be modified to suit each species unique structure as suggested by González-Jaramillo, Fries and Bendix (2019) –

$$d = \frac{c}{\pi} \tag{4.1}$$

where d is the diameter, c is the circumference and $\boldsymbol{\pi}$ is equal to 3.14159. This final diameter reading was recorded for each of the thirty trees.

This field survey of the trees using conventional methods to acquire the DBH was done to provide comparative data to the photogrammetric point cloud that was acquired later to test the accuracy of that data compared to conventional methods.

4.3 General UAV_{SfM} Data Acquisition of Tree Variables for Biomass Estimation

The data acquired for this endeavour includes ground control points (GCPs); DBH field measurements of the trees; and nadir, oblique and/or tessellated façade imagery acquired with a UAV (DJI Phantom 4 Pro). Images were acquired at three different study areas and collectively over a period of eleven (11) months, between June 2018 and May 2019. The following sub-sections detail the general workflow for the photogrammetric process from reconnaissance through to analysis and feature extraction.

4.3.1 Reconnaissance

A preliminary inspection of the study area was performed to determine the optimal positions for the placement of GCPs for the image acquisition phase. The logical and even spread of GCPs ensures that all points of interest (POI), in this case the trees to be captured, are within the sphere of influence of the GCPs so that the POIs are georeferenced accurately. The use of GCPs was also decided upon to aid correct shifts and distortions due to possible loss of or poor IMU and GNSS/GPS measurements recorded by the UAV during flight (Puliti, 2017), and possibly improve overall image registration (Dandois, Olano and Ellis, 2015). Where possible, easily identifiable features, such as road markings or curb corners were identified as possible GCPs. Where no easily identifiable features existed, GCPs in the form of 1 m by 1 m black and white mats would be used as an easily identifiable feature from the captured images.

Suitable take-off and landing sites at the study areas were also identified, as well as any obstructions like taller trees or buildings that could hinder the UAV in acquiring the necessary images. The extremities, in terms of horizontal and vertical distances, of the forest clusters to be surveyed were estimated. Gaps in between the trees that formed gaps in the tree canopy were also noted during this phase as it indicated gaps that could allow for the modelling of the below-canopy ground and features. This gave an indication on the

optimal flight patterns to use to acquire as much information as possible from various perspectives.

These factors were necessary for the flight planning phase of the photogrammetric process which would suggest the necessary data capture technique, flight patterns, flight heights, flight areas to be covered and flight time.

4.3.2 Flight Planning

Multiple flight plans were created for each of the three study areas on a mobile phone using the Pix4D Capture mobile application (www.pix4d.com) (Pix4Dcapture, 2019b). The mobile application was selected for several reasons, chiefly being that it is a free to download and use application and has simple but moderately customisable flight plan settings. The application also allows for the programming of a double grid nadir flight pattern, which programmes the UAV to fly in a North to South flight pattern and then in a West to East flight pattern, thereby forming parallel lines across the forest canopy. This is especially useful when attempting to capture multiple nadir images from multiple perspectives across the forest canopy to capture as much detail as possible. A circular flight plan is also possible through the application. This programmes the UAV to fly in a circular pattern around the trees being surveyed, at a set distance from the centre of the forest structure (a specified circle radius) and acquire images at a set camera angle tilt (oblique imagery) that faces the centre of the circle, which is useful for capturing below-canopy features when the UAV is flown at a low enough altitude. These two flight patterns were used when surveying all the three study areas. The circular flight pattern is especially advantageous with multi-rotor UAVs as the camera-facing direction can be independent of the flight direction, and multiple imagery can be acquired at a much slower UAV speed which results in more imagery but covers multiple angles of the scene. This technique also greatly reduces motion blur. Since the application designs the flight plans based on the specific technical capabilities of the UAV in use, such as the sensor size, and desired flight altitude, the flight plans were designed for the DJI Phantom 4 Pro Quadcopter (DJI, 2017b) which has a 20 Megapixel image sensor, which results in a higher resolution image. The UAV model type was entered into the mobile application upon starting the flight planning process. The following sub-sections detail the flight heights planned for the nadir, oblique and tessellated façade flight patterns.

4.3.2.1 Nadir Double Grid Flight Plan

Each nadir double grid was planned with the same basic principles. The first step was to define the flight extremities in the form of a rectangular or polygonal grid around the trees to be surveyed. These were advised by the earlier reconnaissance phase. Designing the boundary was done by creating a rectangular boundary around the trees to be surveyed against a Google Earth base map of the area preloaded on the mobile application. These extremities measured differently for each study area - 125 m by 125 m for $H_{omo}FS$, 102 m by 105 m for $H_{etero}FS_1$, and 115 m by 160 m for $H_{etero}FS_2$. The other settings such as flight altitude, speed and overlap were then adjusted afterwards. *Table 4.1* below highlights the other nadir double grid flight specifications designed for the DJI Phantom 4 Pro Quadcopter at varying heights to capture imagery at the three study areas – $H_{omo}FS$, $H_{etero}FS_1$ and $H_{etero}FS_2$. These specifications vary, as they are each functions of the area to be covered, the approximate tree heights of the forest structures, and unique forestry conditions. By planning a variety of flight altitudes, it would be possible to test later which of the flight heights is most suitable for collecting data for tree variable estimation. This is because the flight altitude and GSD are directly correlated. Although several studies were reviewed before this undertaking, none reviewed the use of a combination of nadir images acquired at different heights. As such, multiple flight plans were planned for the study areas at varying heights with the possibility of combining them into a multivariate height SfM model, in case datasets from any specific height proved insufficient.

Table 4.1 | *Flight plan specifications for nadir double grid flights of the study areas*

Parameters	**Values**		
	$H_{omo}FS$	***$H_{etero}FS_1$***	***$H_{etero}FS_2$***
Flight Altitude (AGL)	40 m and 50 m	50 m, 60 m, 80 m and 100 m	35 m, 50 m and 100 m
Total Approx. Flight Time	17 min	19 min	42 min
Size/Area	125 m by 125 m	102 m by 105 m	115 m by 160 m
GSD	1.10-1.37 cm/px	1.37-2.74 cm/px	0.96-2.74 cm/px
Front and Side Overlap	80%	80%	80%
Flight Speed	5 m/s	5 m/s	5 m/s
Camera Angle	90°	90°	90°
Approx. Number of Images	402	361	826

For example, a nadir flight plan was designed at 40 m AGL for $H_{omo}FS$, as well as a nadir flight plan at 50 m AGL. The 50 m AGL flight plan was designed to capture a wider area, and therefore more features, of the study area to be used in the Structure-from-Motion and image feature matching software in the processing phase of the study to aid with better registration of the imagery, while the 40 m AGL flight plan was designed to capture closer and finer detail to add richer detail to the features captured. Multiple nadir flight plans were also prepared at varying heights for the other two study areas – $H_{etero}FS_1$ and $H_{etero}FS_2$ – at 50 m AGL, 60 m AGL, 80 m AGL and 100 m AGL for $H_{etero}FS_1$, and 35 m AGL, 50 m AGL and 100 m AGL for $H_{etero}FS_2$. Because flight height and GSD have a direct relationship, it was not necessary to manually set the desired GSD on the mobile application as this was automatically adjusted with each adjustment of the flight altitude. In the case with $H_{omo}FS$, setting a flight altitude of 40 m AGL resulted in a GSD of 1.10 cm/px.

The drone speed on the mobile application was set to 'slow', which programmes the drone to fly between 3 m/s and 5 m/s as this greatly reduces motion blur resulting in better suitable imagery. The camera angle was set to capture imagery vertically below, at 90° from the flight direction. To ensure that the images were captured in a manner that would provide adequate stereo pairs during processing, the overall overlap (front and side) was set to 80%. This high overlap is necessary given the nature of the scene being acquired because it ensures that there is increased canopy penetration in an effort to map below-canopy forest structures with nadir and oblique images (Dandois, Olano and Ellis, 2015).

4.3.2.2 Oblique Circular Flight Plan

During the literature review phase of the research, no particular study highlighted the use of oblique imagery or a circular mission in the acquisition of data for tree variable extraction, and thus AGB estimation. This study includes this dataset as a means to acquire below-canopy data on forest structures, like tree trunks, at lower altitudes. A flight plan was again created for each of the study areas using the Pix4D Capture mobile application. The circular missions were designed with a variable radius from the circle centre and with a camera tilt between 0° and 90°. As with the nadir double grid flight plans, flight plans for the circular missions were also designed at varying heights to capture more below-canopy forest structures from multiple perspectives. Flight heights for the study areas were - 20 m

AGL and 30 m AGL for $H_{omo}FS$, 50 m AGL for $H_{etero}FS_1$, and 50 m AGL and 60 m AGL in $H_{etero}FS_2$.

Each of these flight plans included a circular trajectory around the forest structure, set against a Google Earth base map preloaded into the mobile application, and the extremities were adjusted based on observations made during the reconnaissance phase. The flight altitude was then adjusted to result in a suitable GSD. The UAV speed was the then adjusted on the application to 'slow' which translates to 3 m/s to 5 m/s, and the capture angle set to 10° which indicates that an image is captured every 10° of the 360° circle around the forest structure. Both these settings allowed for the UAV to move at a slower speed and capture images at shorter intervals thereby ensuring that numerous images are acquired from multiple perspectives. Pix4D Capture automatically sets the camera angular tilt to 45° when capturing images in the circular mission to provide the oblique imagery. Below in *Table 4.2* is highlighted the various mission parameters designed for the circular mission surveys of the three study areas. The table highlights the flight heights, areas covered, image count, and camera tilt etc.

Table 4.2 | *Flight plan specifications for circular mission flights of the study areas*

Parameters	**Values**		
	$H_{omo}FS$	$H_{etero}FS_1$	$H_{etero}FS_2$
Flight Altitude (AGL)	20 m and 30 m	50 m	30m, 50 m and 60 m
Total Approx. Flight Time	8 min	4 min	26 min
Size/Area	125 m by 125 m	102 m by 105 m	115 m by 160 m
GSD	1.66-1.77 cm/px	1.86 cm/px	1.87-2.35 cm/px
Capture Angle	10°	10°	10°
Flight Speed	3 m/s	3 m/s	3 m/s
Camera Angle	35° and 45°	90°	90°
Approx. Number of Images	247	88	360

4.3.2.3 Tessellated Façade Flight Plan

Although nadir and circular (oblique) mission flight plans were planned for each of the three study areas, the tessellated façade flight plan was planned for only two of the study areas – $H_{etero}FS_1$ and $H_{etero}FS_2$. This flight technique is applied as an alternative to terrestrial photogrammetry, as was used in a study by Carnevali et al. (2018) for close-range photogrammetry for an architectural survey of a historic building, and specifically as an attempt to capture more below-canopy detail in dense forests as would possibly be achieved using a conventional Digital Single-Lens Reflex (DSLR) camera.

This flight technique was not planned in the Pix4D Capture mobile application, as the application does not have a function that supports this flight technique, nor could it be specifically programmed into the DJI Go 4 (www.dji.com) mobile application, the default mobile application for remotely controlling the DJI Phantom 4 Pro UAV from a mobile appliance.

However, it was planned that images would be captured of the forest face. This was achieved by planning to fly parallel to the forest face and at least 15 m from the forest face, resulting in a 0.41 cm/px GSD. For example, for $H_{etero}FS_1$, each individual vertical baseline was approximately about 15 m, with a camera event, where the camera captured an image, occurring every 2 seconds. This, coupled with the UAV speed, ensured that there was at least an 80% overlap between images acquired in the vertical direction. Each horizontal baseline between the vertical baselines was also approximately 2 m in length and with a camera exposure event still occurring every 2 seconds which also ensured at least an 80% overlap between images captured between vertical baselines. This was repeated over the length of the visible façade within the study area, which resulted in at least 30 individual vertical baselines along an 85 m horizontal baseline parallel to the forest façade. *Table 4.3* below highlights the flight parameters designed for the tessellated façade flight of $H_{etero}FS_1$.

Table 4.3 | *Flight plan specifications for the tessellated façade flight of* $H_{etero}FS_1$

Parameters	**Values**
	$\boldsymbol{H_{etero}FS_1}$
Flight Altitude (AGL)	2 m - 15 m
Total Approx. Flight Time	1 hour 5 min
Total Horizontal Baseline	85 m
Vertical Baselines (each)	15 m
GSD	0.41 cm/px
Flight Speed	3 m/s
Camera Angle	0° - 30°
Approx. Number of Images	1255

4.3.3 Data Capture

Each data capture phase of the research for the study areas followed soon after their respective flight plans were created. The general procedure during this phase followed the sequence – place GCPs at ideal positions within perimeter to be flown, survey coordinates for GCPs using GNSS, and perform aerial mission based on previously defined flight parameters.

For the data capture of $H_{omo}FS$, five pre-marks (GCPs) named Pre-mark 1, Pre-mark 2, Pre-mark 3, Pre-mark 4, and Pre-mark 5 were placed around the cluster of trees so that they are not obstructed by any of the trees or their shadows. GCPs printed on standard 60 cm by 60 cm black and white tile sheets were used for this study area. *Figure 4.2* below shows some of the GCPs placed around the study area. These images were captured at 40 m AGL.

Figure 4.2 | *(a) Pre-mark 1, and (b) Pre-mark 3 – two of the five GCPs placed around $H_{omo}FS$*

A Trimble R8 GNSS Base and Receiver was then used survey the GCPs. The Base was set up nearby and powered on to start logging observations. The receiver was then powered on as well in RTK mode. Several Town Survey Marks (TSMs) in the area were then surveyed as control points and checks to do an appropriate coordinate transformation from geographic coordinates to the National Coordinate System, Hartebeesthoek94. The centre of the aerial survey GCPs were then surveyed to within 0.03 m accuracy in both the horizontal and vertical coordinates (*Table 4.4*) and logged in the GPS receiver controller.

Table 4.4 | *GCPs coordinates at $H_{omo}FS$*

Ground Control Point	**Values**		
	X	Y	Z
Pre-mark 1	47806.477	3759121.232	20.146
Pre-mark 2	47906.124	3759141.492	19.858
Pre-mark 3	47874.201	3759198.990	20.086
Pre-mark 4	47819.483	3759204.006	20.549
Pre-mark 5	47791.282	3759194.885	20.204

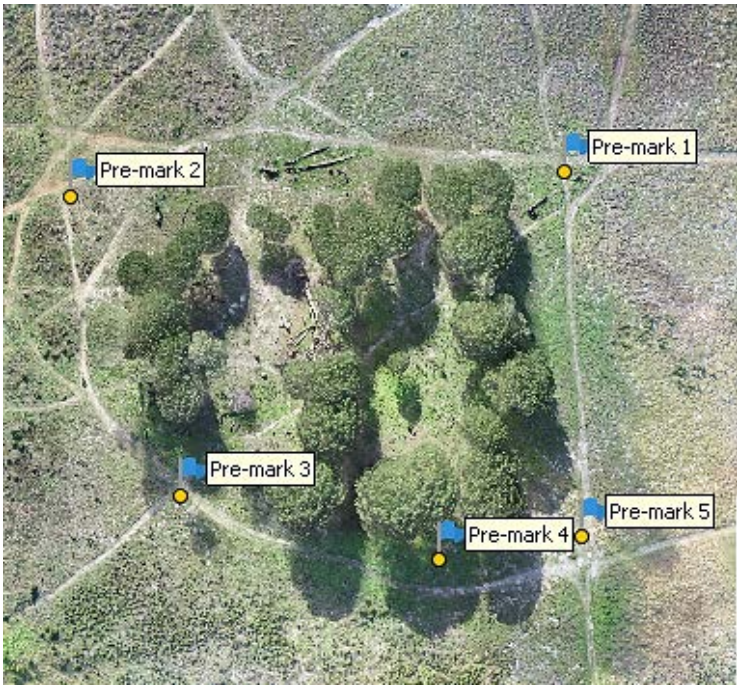

Figure 4.3 | *Relative placement of all GCPs to each other at $H_{omo}FS$*

The DJI Phantom 4 Pro was then assembled and placed near the forest structures but away from any immediate obstructions. The UAV was first turned on. A Samsung Galaxy Note 5 smartphone was connected to the controller with a USB cable and then the controller was turned on. The DJI Go 4 (www.dji.com) mobile application, DJI's proprietary mobile application for remotely piloting various DJI UAV models, was used to set certain parameters on the drone such as obstacle avoidance and camera image capture settings. The camera was set to capture images with a fixed exposure of 1/200 and ISO 100. Once the UAV was able to track more than twelve (12) satellites with its on-board GPS unit, a feature that enables sustained stable flight, and had set the home point for its return, the nadir double grid flight plan was uploaded to the UAV through the Pix4D Capture mobile application. The autonomous aerial mission was then started.

Once the UAV had captured all the images and had landed safely, the circular mission was uploaded to the UAV and that was flown autonomously as well. These plans uploaded to the UAV are as per specifications listed in *Table 4.1* and *Table 4.2* above. Images were acquired over a period of three days, each consisting of one nadir flight and one circular mission – 20th of June 2018, 22nd of June 2018 and the 18th of July 2018 – and around the same time of day to maintain uniformity in the lighting conditions. A total of 649, nadir and oblique, images were captured for $H_{omo}FS$.

$H_{etero}FS_1$ made use of six GCPs for geo-referencing the acquired imagery – GCP1, GCP2, GCP3, GCP4, GCP5 and FUJ. GCP2 to GCP5, and FUJ were 1 m by 1 m black and white tile sheets, while GCP1 was the edge of the end of a road centre line marking adopted as a GCP. The mats were placed on areas that were within the flight design boundary.

Figure 4.4 | *(a) GCP3, (b) GCP2 (between cars), (c) FUJ, and (d) GCP1 – four of the six GCPs placed around* $H_{etero}FS_1$

The receiver, a Trimble R8 DGPS GNSS Receiver, was then powered on in RTK mode and connected to Trimble Virtual Reference Station (VRS). Several TSMs in the area were then surveyed as control points and checks to do an appropriate coordinate transformation from geographic coordinates to the Hartebeesthoek94 coordinate system. The coordinates of the centre of the GCPs and the edge the road marking were then surveyed. All GCPs were surveyed to within 0.03 m accuracy in both the horizontal and vertical coordinates (*Table 4.5*) and logged in the GPS receiver controller. All GCPs were surveyed on the 20th of June 2018.

Table 4.5 | *GCPs coordinates at $H_{etero}FS_1$*

Ground Control Point	Values		
	X	Y	Z
GCP1	50235.902	3759159.792	168.610
GCP2	50163.499	3759201.556	153.285
GCP3	50195.855	3759270.431	153.962
GCP4	50221.543	3759199.806	161.532
GCP5	50163.478	3759198.821	153.345
FUJ	50278.610	3759239.080	167.895

Figure 4.5 | *Relative placement of GCPs to each other at $H_{etero}FS_1$*

The same pre-flight procedures were followed as was with the nadir and oblique aerial survey of $H_{omo}FS$. Once the UAV was able to track more than twelve (12) satellites with its on-board GPS unit and had set the home point for its return, the nadir double grid flight plan was loaded on the Pix4D Capture mobile application for final review, paired to the UAV and uploaded to it. The autonomous aerial mission was then started. Once the UAV had captured all the nadir images and had landed safely, the circular mission was uploaded to the UAV and that was flown autonomously as well. These plans uploaded to the UAV are as per the flight plan specifications listed in *Table 4.1* and *Table 4.2* above. Nadir and

oblique images were acquired over a period of three days, each day consisting of one nadir flight and one circular mission – 12th of February 2019, 23rd of February 2019 and the 10th of May 2019 – and around the same time of day to maintain uniformity in the lighting conditions across all images. A total of 449 nadir and oblique images were captured for $H_{etero}FS_1$.

Approximately 1255 tessellated façade images were captured on the 10th of May 2019 after both the nadir and oblique flights were concluded. The tessellated façade flight was carried out as per the flight plan specifications listed in *Table 4.3,* detailed in *Section 4.2.2.3* and carried out similarly to the survey by Carnevali et al. (2018). To achieve this, 40 targets were laid all over the survey area, in addition to the six 1 m by 1 m GCPs already present in the area laid during the nadir and circular missions. Targets used in this survey were opposing black triangles printed on white A4 sheets, measuring 210 × 297 mm. As this was a façade aerial survey, the targets needed to be captured on a vertical surface and being a forest, solid multi-textured structures were not readily available. Most of the targets were taped or stapled on the trees (*Figure 4.6*) to be surveyed, making sure that several targets could be seen per captured image, forming several stereo pairs. Some other targets were placed on the interlocked ground in the parking lot that adjoined the forest structure, and others were fixed on other structures such as big shipping containers in the area, immovable rocks and other fixed structures in the area.

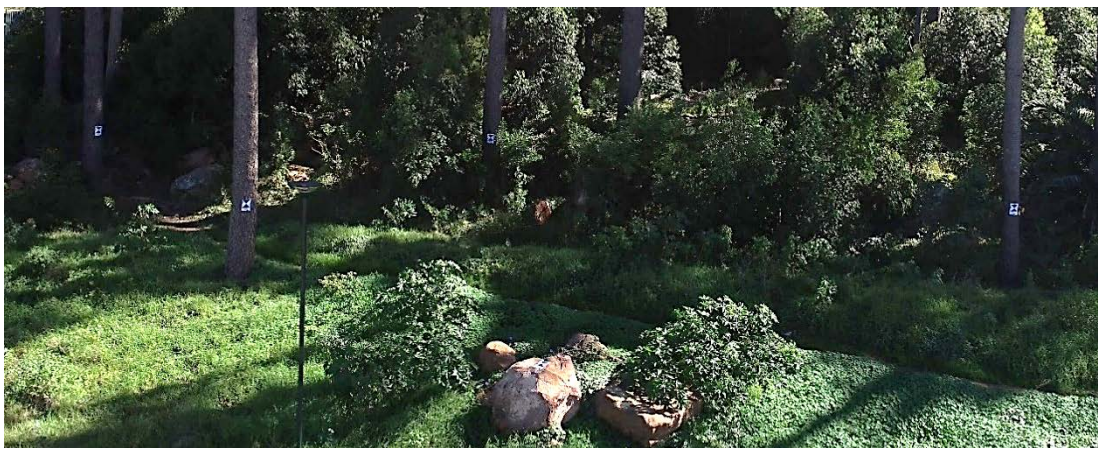

Figure 4.6 | *Scene from $H_{etero}FS_1$ showing the A4 sized targets fixed on the tree trunks*

One of the main overcautious aims for using numerous targets was to provide discernible features to use as control to assist the image matching process when processing images with monotonous features like identical tree trunks that have the same dull texture, or

green bushes or leaves that have the same shiny green shimmer. Because it is an already time-consuming task to establish these targets on the tree trunks, surveying the coordinates with a Total Station to georeference the resulting point cloud would be an equally tedious task. Since Agisoft Metashape is capable of matching distinct features, it was not entirely necessary to assign coordinates to the targets to assist with the accurate matching of features as the GCPs on the ground would both have coordinates on the national coordinate system, which would reference the entire point cloud on the national coordinate system and serve as additional features to help image matching since they appear in numerous images at varying scales. The extracted coordinates of the targets from the point cloud would be used later for the TLS survey at a later phase to register the scans together.

The mission was not flown autonomously, but rather the UAV was programmed to, when remotely piloted, fly in a straight line parallel to the forest face. Doing this allowed the UAV to keep its directional orientation, while giving the freedom to pilot it vertically or horizontally but remain parallel to the forest face, as well as turn the UAV 360° on its vertical axis, about the horizontal plane. This kept the direction of movements uniform.

The tessellated façade aerial survey followed the same procedures as both the nadir and oblique flight procedures. The UAV was set up on a nearby launch position, clear of any obstructions. The event/ camera capture was set to 2 seconds, fixed exposure set to 1/400 and ISO set to 100 on the DJI Go 4 (www.dji.com) mobile application on the Samsung Galaxy Note 5. The tessellated façade survey was flown manually in 'Precision mode' once 12 satellites were being tracked by on the onboard GPS – this assists with stabilising the UAV while in manual flight. The flight lines were manually flown in a 15 m vertical upward path, 2 m horizontal path, 15 m vertical downward path, and 2 m horizontal path pattern to cover the entirety of the forest façade. Capturing a single image every 2 seconds translated into ±90% image overlap providing abundant imagery from multiple perspectives. Capturing all the tessellated façade images took a combined total of 66 minutes.

The third study area captured was $H_{etero}FS_2$. $H_{etero}FS_2$ made use of four GCPs for geo-referencing the acquired imagery – GCP1, GCP2, GCP3, and GCP4. All GCPs used were 1 m by 1 m black and white tile mats draped over a 12 mm round iron rod hammered into the

ground. This was done in case more than one day was required for the aerial mission to adequately capture the scene so placing and surveying the coordinates of the rods would provide a known and fixed position and eliminate the need to survey the centre of the mats before every survey. The centres of the mats were positioned so that they coincided with the centre of the iron rods. As with the other aerial missions, the iron rods, and subsequently, the mats, were placed on areas that were within the flight design boundary.

Figure 4.7 | *(a) GCP1, (b) GCP2, (c) GCP4 – three of the four GCPs placed around* $H_{etero}FS_2$

Due to the location of the study area, there were no known points, such as TSMs close by to survey and do a coordinate transformation to tie the survey to the national coordinate system, so neither RTK nor VRS were an option with $H_{etero}FS_2$. Instead, a Trimble R4 GNSS was used. The static survey was performed, and the coordinates provided, by an independent study investigating wetlands in the Steenbras Dam area. The GNSS base was set up over a 12 mm round iron peg hammered into the ground nearby and surveyed on

both the 19th of July 2018 and the 31st of August 2018. On each of these days the base was on and observing readings for at least three-hours in Static Survey mode. Thereafter, the rover was used in Real Time Kinematic (RTK) survey mode to then survey the four GCPs laid around the study area. The observations acquired on the 31st of August 2018 were then downloaded, along with four other TrigNet (ftp://ftp.trignet.co.za) base stations – Cape Point (CPNT), Steenbras (SBAS), Hermanus (HNUS) and Stellenbosch (STBS) – that were positioned around the study area. The average baseline distances between the trigs were approximately 40 km.

Processing of the data was done after the fieldwork, though most precise ephemeris are only available every 12 days. Because of a time constraint, rapid ephemeris were downloaded to improve coordinate precision.

Continuously Operating Reference Station (CORS) data for the six days leading up to the processing day, at an epoch of 30 seconds, as well as collected RINEX data from the Steenbras CORS to include the latest ITRF2014 estimates were added to the processing. Elevations were however restricted to the SAGEOID2010, which is a hybrid model derived from modelling gravity data, GPS/levelling data and harmonic coefficients. This helps convert ellipsoidal heights obtained from the GNSS to heights on the national height datum, or orthometric heights.

The GCP coordinates were transformed from ITRF2014 to Hartebeesthoek94, the national coordinate system. Average shift between ITRF2014 and Hartebeesthoek94 were approximately 0.40 m and 0.60 m in horizontal coordinates (X and Y). All four GCPs that were measured using RTK were measured to within 0.03 m in both horizontal and vertical positions. All processing was post-processed later in the office using Trimble Business Center v5.00 (www.geospatial.trimble.com) to provide the GCP coordinates on the national coordinate system. *Table 4.6* below shows the coordinates of the four GCPs used at $H_{etero}FS_2$.

Table 4.6 | *GCPs coordinates at $H_{etero}FS_2$*

Ground Control Point	Values		
	X	Y	Z
GCP1	8544.504	3783737.386	396.871
GCP2	8501.952	3783707.737	400.326
GCP3	8582.020	3783701.611	388.399
GCP4	8578.554	3783663.775	383.708

Figure 4.8 | *Relative placement of GCPs to each other at $H_{etero}FS_2$*

Figure 4.8 above shows the positions of the GCPs used at $H_{etero}FS_2$. The same pre-flight procedures were followed as was with the nadir and oblique aerial surveys of $H_{omo}FS$ and $H_{etero}FS_1$. The UAV was set up and placed at an area clear of any obstructions. Once the UAV was able to track more than twelve (12) satellites with its on-board GPS unit and had set the home point for its return, as indicated on the DJI GO 4 (www.dji.com) mobile application, the nadir double grid flight plan was loaded onto the UAV using the Pix4D Capture mobile application. The application was also used for final review of the flight plan before it was uploaded. The autonomous aerial mission was started. Once the UAV had captured all the nadir images, based on the flight parameters listed in *Table 4.1*, and had landed safely, the circular mission was uploaded, based on the flight parameters listed in *Table 4.2*, to the UAV and that was flown autonomously as well. Nadir and oblique images were acquired over a period of five days, each day consisting of one nadir flight and one circular mission – 19th of June 2018, 31st of August 2018, 4th of October 2018, 7th of

February 2019, 10th of December 2018, and the 7th of February 2019 – and around the same time of day to try and maintain the same lighting conditions throughout. A total of 1186 nadir and oblique images were captured for $H_{etero}FS_2$.

4.3.4 Data Processing

Several software were utilised during the processing of the photogrammetric data – from acquiring the images through to producing the point cloud, DTM and orthomosaics. Though some software exist as a 'one-stop shop' for photogrammetric point cloud data, utilising powerful 'black box' technology and techniques to produce them, this research uses various software to process the datasets used. For the purpose of producing, cleaning and analysing the photogrammetric point cloud and subsequent datasets in this research endeavour, the following software were utilised –

1. Agisoft Metashape v1.5.1
2. Blue Marble Global Mapper v18.1, v20.1
3. Autodesk Recap v6.0.0

Each software and its use in the process with producing measurable datasets is elaborated further in the section and the chapter.

4.3.4.1 Processing the photogrammetric point cloud data

Agisoft Metashape is an advanced image-based three-dimensional modelling solution that uses SfM technology and is aimed at creating professional quality three-dimensional content from still images. Photos can be taken from numerous positions, provided that the object to be reconstructed is visible on at least two images to form a coherent stereo-model. The software is fully capable of completely automating the entire process from image alignment through to creating the DEM and the orthomosaic (Agisoft, 2017).
Once all the images were captured for all three study areas using the DJI Phantom 4 Pro in the field, they were imported into the software to be processed into point cloud using the software's SfM technology.

To create the three-dimensional point cloud for *$H_{omo}FS$*, both the nadir imagery and oblique imagery acquired at varied above ground levels during the field work were processed together in Agisoft Metashape. For the processing of this particular dataset, a Lenovo Y70 (Lenovo, 2020) high performance gaming laptop was utilised. The laptop has the following specifications: Intel® Core™ i7 processor, NVIDIA® GTX-860M with 4G VRAM graphics card, and 16GB DDR3L RAM. Though the process is similar throughout all SfM datasets, this section highlights the process carried out with processing the *$H_{omo}FS$* data.

A chunk, a native Agisoft function which allows for separate processing of subsets of a complete image set and subsequent merging of the results, containing all 647 nadir and oblique images was created in Agisoft Metashape v1.5.1 for 'HomoFS'. Though Agisoft Metashape is able to discern the image positions based on the image-embedded geographic coordinates, improvements in calculation and reduction in processing time can be made by adding exterior camera orientation information, especially if the precise image coordinates as well as orientation information (Omega, Phi, and Kappa) have already been calculated from trajectory information. To achieve this, the image WGS84 coordinates were transformed to the national coordinate system for the area (Projection: Transverse Mercator, Datum: Hartebeeshoek94, and Central Meridian: 19) using Global Mapper. These new coordinates were used to improve the accuracy of the image alignment in Agisoft Metashape.

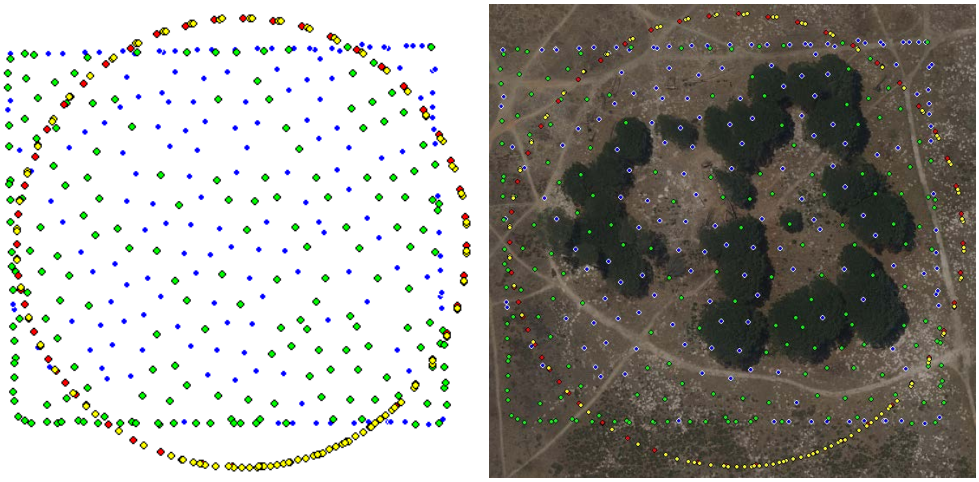

Figure 4.9 | *Image positions at $H_{omo}FS$ showing all nadir images captured at the various heights – Blue (40m) and Green (50m), as well as the oblique images captured at various heights – Red (20m) and Yellow (30m)*

The coordinates were imported into Agisoft Metashape to refine their positions. The images were aligned in order to acquire tie points between the images, a necessary procedure in the production of multi-view three-dimensional reconstruction. The settings used during the alignment as listed in *Table 4.7* below.

Table 4.7 | *Alignment settings used for $H_{omo}FS$*

Parameter	Value
Accuracy	Low
Generic preselection	Yes
Reference preselection	Yes
Key point limit	40 000
Tie point limit	1 000

To ensure that the resulting project is situated on the correct coordinate system and improve the accuracy of the orthomosaic and model by optimising exterior camera orientations, it is necessary to add control to the project. A total of 5 markers – Pre-mark 1 to Pre-mark 5 – were used for $H_{omo}FS$ as GCPs. Five GCPs are used here as it has been proven that a large number of GCPs do not necessarily improve the accuracy of the image or photogrammetric point cloud (González-Jaramillo, Fries and Bendix, 2019). Optimising the images using the GCPs yielded a total error of x = 0.0014 m, y = 0.0066 m and z = 0.0013 m showing excellent agreement between the GCP coordinates and their positions on the images.

A batch file in the software was created to automate the processing of the dense point cloud, the DEM, and the orthomosaic without any further human involvement. The SfM workflow follows a basic procedure: (a) Feature Extraction, (b) Feature Matching, and then (c) Feature Reconstruction (González-Jaramillo, Fries and Bendix, 2019). This produces a dense point cloud of the area. The DEM was created using the Triangulated Irregular network (TIN) method to create a surface. An orthomosaic was also generated, which is a function of the image resolution, which itself is a function of the flight height and image sensor used to capture the images. See Appendix A for Agisoft Metashape processing report for $H_{omo}FS$ detailing specifications, parameters and times recorded during the process. See *Figure 4.10* below for resulting dense point cloud.

The point cloud would be used to create the DSM, DEM and CHM, while the orthomosaic would be draped over the models to help with referencing measurements.

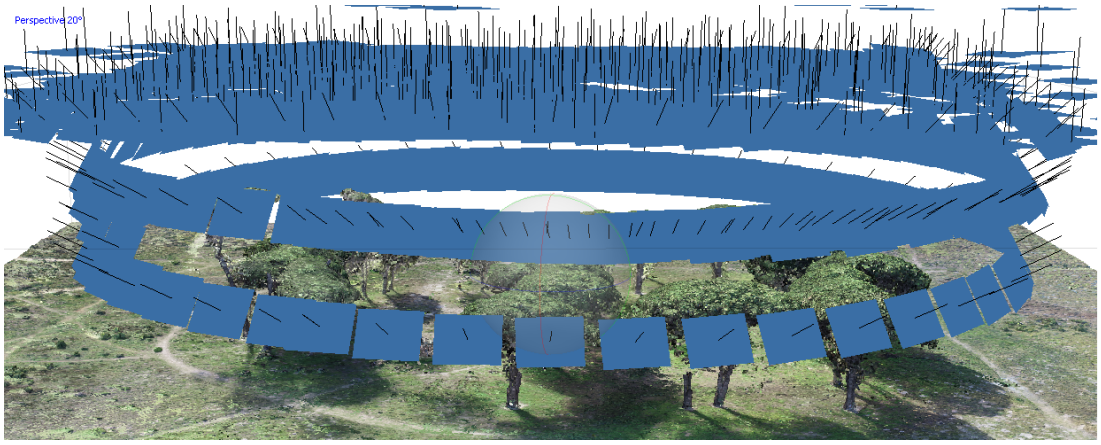

Figure 4.10 | *Image positions of the captured nadir and oblique images at varying heights over the dense cloud of $H_{omo}FS$ within the Agisoft Metashape workspace*

The same procedure was followed for both $H_{etero}FS_1$ and $H_{etero}FS_2$ study areas, and in each case their respective GCPs were used to improve their exterior camera orientations and overall processing accuracy and speed.

An exception to this procedure was made when processing the images acquired during the tessellated façade aerial survey for several reasons. One reason was due to the sheer number of images acquired, being 1255 images. Of these 1255 images acquired, five were unusable as they had too much sun glare in them. These were discarded. Five separate chunks were created in Agisoft Metashape to help speed up the processing time. Images were assigned to the various chunks based on the order in which they were captured. The chunk names and details of how the images were captured are detailed below in *Table 4.8*.

Although Agisoft Metashape is capable of detecting features in clear and coherent images using a Scale-Invariant Feature Transform (SIFT) algorithm, which essentially is a computer vision image detection algorithm capable of discerning local features in an image, the images had to be split up into these five different chunks within the software. Although processing all the imagery as a single image subset (chunk) increases accuracy and the quality of the results, it can be time consuming as the software is processor and RAM intensive, relying heavily on both these components to detect tie points for image matching and dense cloud production. This process slows down considerably once all the

available RAM is assigned to assisting in the processing of the images, often leading to software crash or computer freeze depending on the size of the project or number of images.

Table 4.8 | *Details on the Agisoft Metashape five chunks created for the Tessellated Façade Photogrammetric Survey Mission of* $H_{etero}FS_1$

Agisoft Metashape Chunk	Details
Batch 1	197 images – Images captured around the forest structure on a rectangular perimeter, with an angular camera tilt of 45°.
Batch 2	359 images – Images captured at 0° angular camera tilt, 15 m from the forest face, and moving parallel to the forest face.
Batch 3	295 images – Images captured at 0° angular camera tilt, 15 m from the forest face, and moving parallel to the forest face.
Batch 4	300 images – Images captured at 35° angular camera tilt, 20 m from the forest face, and moving parallel to the forest face.
Batch 5	99 images – Images captured at 35° angular camera tilt, 20 m from the forest face, and moving parallel to the forest face.

Splitting the data into several chunks deters these problems but sacrifices accuracy as it limits the number of image pairs used for each camera during the dense cloud generation stage. This could lead to a noisy point cloud as there is insufficient image overlap or insufficient multi-perspective imagery. The separate chunks can however be merged later into a single chunk, along with tie points and the generated dense cloud. As there were several chunks in this project, the software processed one chunk at a time before moving on to the next one. In this way, the processing power of the computer was not held up consistently. Each chunk was aligned automatically in Agisoft to produce tie points which connected all the images. In each individual chunk, the visible GCPs in each image were placed, and their positions optimised as before. A dense cloud was subsequently produced

for each chunk. Each of these chunks were finally merged into one chunk to create one seamless photogrammetric point cloud of $H_{etero}FS_1$.

A separate experiment was done using all the data as stated above, with the exception of using the GCPs. The processing took 6 hours, as compared to the roughly 18 hours it took to process a previous experiment that used the 40 targets placed on the trees and surrounding structures, and the 6 GCPs placed on flat terrain around the area of interest. This new point cloud (*Figure 4.11 below)* still produced data that was suitable for measurement. As the data does not necessarily need the 40 targets to produce an adequate point cloud, this dataset was used as the primary data for the rest of the research. See Appendix B for the tessellated façade aerial mission processing report.

Figure 4.11 | *Tessellated façade aerial mission point cloud of $H_{etero}FS_1$. The point cloud produced coherent measurable tree trunk structures of the trees in the area.*

Because the tessellated façade aerial survey was designed to acquire below-canopy forest structures, there was no need to create an orthomosaic or a DEM since the tree trunk measurements would be extracted and measured directly from the point cloud.

An attempt was made for capturing tessellated façade imagery of the $H_{etero}FS_2$ site. However, due to the presence of significant undergrowth of a *Pinus* subspecies, a majority of the tree trunks were obstructed from view of the camera thereby making it highly improbable to acquire enough overlapping images of the below-canopy forest structures. Processing of these images in Agisoft Metashape was thus not attempted as the probability of obtaining a successful and usable point cloud was low.

4.3.4.2 Computing the photogrammetric TH and DBH

This section elaborates how the various measurements were extracted for tree height and tree diameter from photogrammetrically produced point cloud data and DSM, DTMs and CHMs for the individual trees across all three study areas within the Global Mapper software. This workflow was identical when processing data for study areas $H_{omo}FS$ and $H_{etero}FS$.

Although photogrammetric point cloud is usually much denser than ALS LiDAR data – 1188.30 points/m^2 point density compared to 2.07 points/m^2 for $H_{omo}FS$ for example – the imported point cloud was not thinned (where every n_{th} point is imported into the dataset) as is common when attempting to create DTMs of ground surfaces from really dense point cloud data because most TIN algorithms achieve this relatively well with much lower point densities. The decision to not thin the point cloud was further motivated because the same point cloud would be used to measure the tree trunks and thinning the dataset could, in some areas, effectively reduce the structural composition of the three-dimensional point cloud representing the tree trunks.

For each study area, a simple naming convention was adopted to help organise data within the Global Mapper project interface. The naming convention followed the sequence: '*Study Area Name_Dataset Source_Capture Date_Point Cloud*'. Photogrammetric point cloud data for $H_{omo}FS$ used was named 'H_{omo}FS_SfM_2018_Point Cloud'. For $H_{etero}FS_1$ and $H_{etero}FS_2$ the datasets were named '$H_{etero}FS_1$_SfM_2019_Point Cloud' and '$H_{etero}FS_2$_SfM_2019_Point Cloud' respectively.

To create the various DSMs, DEMs and CHMs it is necessary to have at least two classes within the data, a ground class consisting of ground points and a vegetation class consisting of vegetation points; or a ground class and any other class, such as a default class, consisting of the other points. In each case, the ground points are necessary for the creation of a DSM and then both classes are necessary for the DEM. In this study, ground and vegetation points are used. An accurate DSM is crucial to the extraction of tree height variables in biomass estimation using photogrammetric and LiDAR data (Kachamba et al., 2016b) and this is dependent on adequately classed ground points within the dataset. Classification of photogrammetric data or LiDAR data generally follows specific stages: (a)

Classification of noise or erroneous points, (b) Classification of ground points, and (c) Classification of non-ground and/or vegetation points. Though the classification of ground and non-ground points (vegetation points) for $H_{omo}FS$ is discussed here, *Table 4.9* below lists the various parameters used in classifying ground and vegetation points for all three study areas. For $H_{omo}FS$, the entire dataset was initially manually classified to a random 'Unclassified' class. This essentially erases and resets to unclassed data any classification previously present in the dataset – the data simply has its initial attributes embedded in it such as a timestamp, GPS coordinates and return type. Though because it is photogrammetric data, the 'return type' present are usually the first and last return.

Erroneous or noisy points within the 'Unclassified' class were classified to a 'Noise' class using the software's 'Automatic Noise Classification' tool, which does so using an algorithm based on user-entered parameters. The simple algorithm searches through the data in grids or bins, also specified, and classifies all points below 1 m, and above 30 m, of the average point cloud level as noise points, with a maximum allowed variance from the local average of 3 standard deviations. The software does this by creating a preliminary modelled 3D curved surface representing the possible ground level and searching for erroneous points that don't match the attributes of their nearest neighbour (Blue Marble Geographics, 2017b). These values were chosen and used when classifying the data in all three study areas because none of the trees exceed 30 m in relative height (±20 m AGL for $H_{omo}FS$ and ±340 m AGL for $H_{etero}FS_2$ for instance) so any points above that would be erroneous or unnecessary. Conversely, any point lower than 1 m of the average point cloud level would also most likely be an erroneous point and therefore unnecessary. This was done to prevent any random spikes or dips in the resulting DSM or DEM and therefore prevent any inaccuracies during measurement.

Table 4.9 | *Ground and vegetation classification parameters used for Photogrammetric point cloud in Blue Marble Global Mapper*

Ground Classification			
Parameters	$H_{omo}FS$	$H_{etero}FS_1$	$H_{etero}FS_2$
Base Bin Size	1 m	1 m	1 m
Minimum Height	0.3 m	0.3 m	0.3 m
Maximum Height	10 m	10 m	10 m
Terrain Slope	3°	3°	3°

Vegetation Classification			
Base Bin Size	0.4 m	2 m	0.4 m
Minimum Height Above Ground	2 m	2 m	2 m
Max Co-Planar Distance	0.08 m	0.08 m	0.08 m
Minimum Vegetation Distance	0.15 m	0.15 m	0.15 m
Max Co-Planar Angle Difference	5°	5°	5°

The 'Automatic Ground Classification' tool within the software was tailored to classify the remaining points in the 'Unclassified' class to the 'Ground' class by searching each individual point and all points within a search area of 1 m bin/grid of those points that could also be ground points. The software does this by removing points that are likely not ground points, and then comparing the remaining points to a modelled three-dimensional surface within the specified bin sizes. To improve the accuracy, the algorithm was restricted to only search and classify points within 0.30 m above the average ground level represented by the modelled curved surface and consider only points within a terrain slope angle of 3° to 5° because the terrain is relatively flat, as is the case with $H_{omo}FS$. *Figure 4.12* below shows a transect of the $H_{omo}FS$ dataset depicting both the unclassified and ground points.

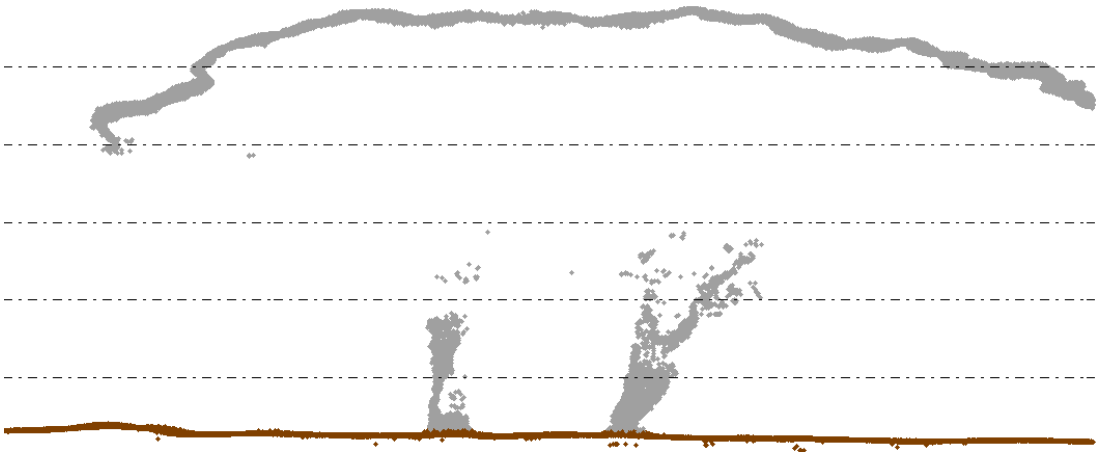

Figure 4.12 | *Difference between ground points (brown points) and default points (grey points) in the $H_{omo}FS$ study area.*

Since there was a clear distinction between ground and non-ground (unclassified) points that were necessary to produce both the DSM and DEM respectively, terrain modelling could have followed immediately after, however, due to the selection criteria outlined in

Figure 3.1 above it is necessary to classify the remaining unclassified points to vegetation points and group them into either the 'High Vegetation' or 'Medium Vegetation' classes. This was done so that only the high vegetation point cloud data would be used later to produce the DEM, once the medium vegetation was filtered out. Achieving this classification was done using the 'Automatic Non-Ground Classification' tool within the software, which is a joint building and vegetation classification tool – classifies unclassified points into both vegetation and building points. The software does this by searching through the dataset and fitting the points within each bin/grid to a calculated best-fit planar surface. Points found close to one another, and that fit this best-fit line, are classified as buildings as this could represent a roof or a wall; while points that are far from the best-fit line are classified as vegetation as they are more sporadic (Blue Marble Geographics, 2017b). The parameters listed in *Table 4.9* indicate the entered search criteria for the algorithm. A limitation with classification algorithms include misclassification, where obvious structures like parts of trees are misclassified as buildings, and is a function of ill-suited input values for the algorithm (*Figure 4.13*). This can be fixed by either attempting several iterations with different variables on a subset of the data to test how the values will work on the whole dataset, or by manually reclassifying these misclassified points to their appropriate classes. As such, there will always be an element of scrutiny of the data through human intervention.

To achieve the classification of vegetation points within the dataset the search criteria in the algorithm was restricted to search within 0.40 m of every unclassified point for other points that could be vegetation points as well – points that are too far from a calculated best-fit line. A minimum height above ground was set to 0.50 m so that only unclassified points above 0.50 m from the classified ground level would be considered in the classification process. The maximum co-planar distance was set to 0.03 m. This specifies the maximum Root Mean Square Error (RMSE) from a best-fit plane, so points much further from the best-fit line are most likely be vegetaion points and will be classified as such. A maximum co-planar angular difference of 10° was used to specify the maximum angle between two best-fit adjacent planes to search within to increase the possibilty of detecting vegetation points.

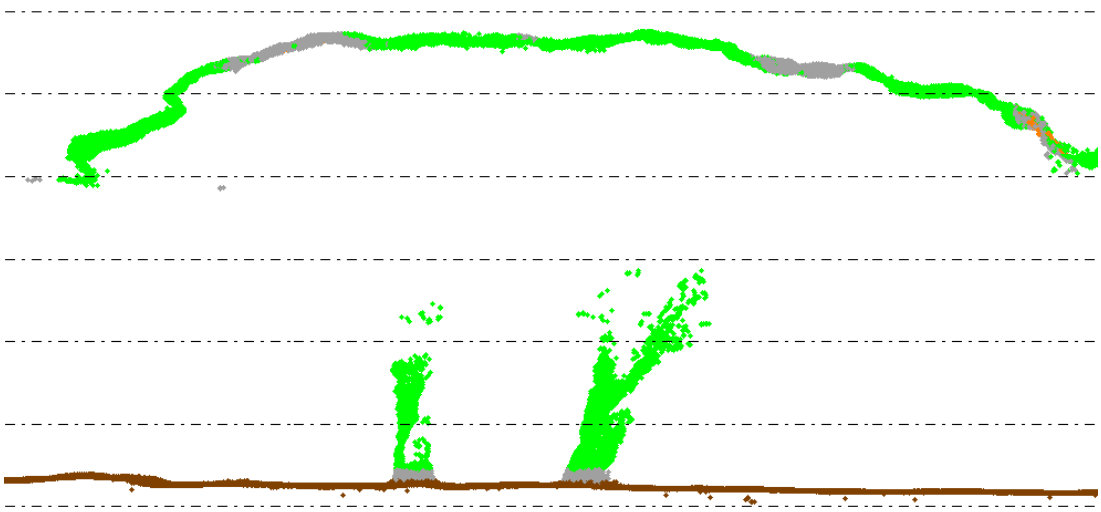

Figure 4.13 | *Transect through part of $H_{omo}FS$ showing ground points (brown), default points (grey) and vegetation points (green). Some misclassified building points exist in the top right corner of the image (orange points), a result of inefficient classification algorithms in the software.*

All misclassified points were manually classified to their appropriate classes based on visual inspection of their spatial (relative position of the misclassified points to other properly classified points) and visual attributes (RGB colour of points) these points were reclassified to improve the overall accuracy of the point cloud. The point cloud was filtered to remove all other points but the ground and vegetation points, both necessary to produce both the DSM and DEM respectively.

To calculate tree height an accurate and suitable surface model is necessary. DSMs are created using only the classified ground points, free of erroneous points that create sudden peaks or valleys in the model that are not true representations of the actual surface observed. These surfaces, which are essentially a mass combination of multiple triangular facets created using each point as a triangle vertex, are achieved using Triangular Irregular Network (TIN) algorithms embedded into the software. DSMs for each of the study areas were created using only the classified ground points and Global Mapper's 'Create Elevation Grid' tool which creates a DEM using the provided points. Although there are different gridding methods available, the method used here is Triangulation, which uses a triangulated irregular network (TIN) to connect the numerous points by their known elevations (Blue Marble Geographics, 2017c). This creates a three-dimensional model comprising of numerous triangular facets that cover the entire area containing any point

feature with elevation values. The grid spacing/resolution was set to 0.10 m as this was sufficiently accurate enough to depict a relatively flat terrain that represents the real-world surface, as well as not be particularly lengthy to process, as the higher the resolution the lengthier the processing time. The naming conventions for the DSMs produced followed the sequence: '*Study Area Name_Dataset Source_Capture Date_DEM Type_Ground Resolution*', as this made it easier to identify the dataset to use during analysis amidst all the models and datasets. For instance, the DSM for $H_{omo}FS$ is 'HomoFS_SfM_2018_DSM_10cm', $H_{etero}FS_1$ is 'HeteroFS$_1$_SfM_2019_DSM_10cm' and $H_{etero}FS_2$ is 'HeteroFS$_2$_SfM_2019_DSM_10cm', where SfM denotes Structure from Motion and is data acquired using the DJI Phantom 4 Pro.

The same procedure was followed for the creation of the DEMs, which are essentially elevation models that depict all structures on the terrain including buildings and trees. To create the DEMs for the three study areas, the High Vegetation and Medium Vegetation points were also filtered into the project. Using a grid spacing/resolution of 0.10 m, the various DEMs were created. Naming conventions followed the same sequence as with the DSMs. For example, for study area $H_{omo}FS$ the resulting DEM is 'H$_{omo}$FS_SfM_2018_DEM_10cm', $H_{etero}FS_1$ is 'H$_{etero}$FS$_1$_SfM_2019_DEM_10cm' and $H_{etero}FS_2$ is 'H$_{etero}$FS$_2$_SfM_2019_DEM_10cm'. To finally extract the tree heights of the individual trees a difference in the surfaces needed to be obtained which is a Canopy Height Model, a prerequisite as suggested by Lim et al. (2003) and González-Jaramillo, Fries and Bendix (2019). The CHM for each of the study areas was based on the formula below –

$$CHM = DEM - DSM \tag{4.2}$$

where ***CHM*** is the study area Canopy Height Model, ***DEM*** is the respective Digital Elevation Model created using a combination of the classified ground and vegetation points, and ***DSM*** is the respective Digital Surface Model created using only the classified ground points. The CHM, or Normalised Difference Height Model (NDHM), yields the absolute height of the structures in the study area – the trees – because both the DEM and DSM have the same reference floor. *Figure 4.14* displays the various DSMs, DEMs and CHMs for the various datasets.

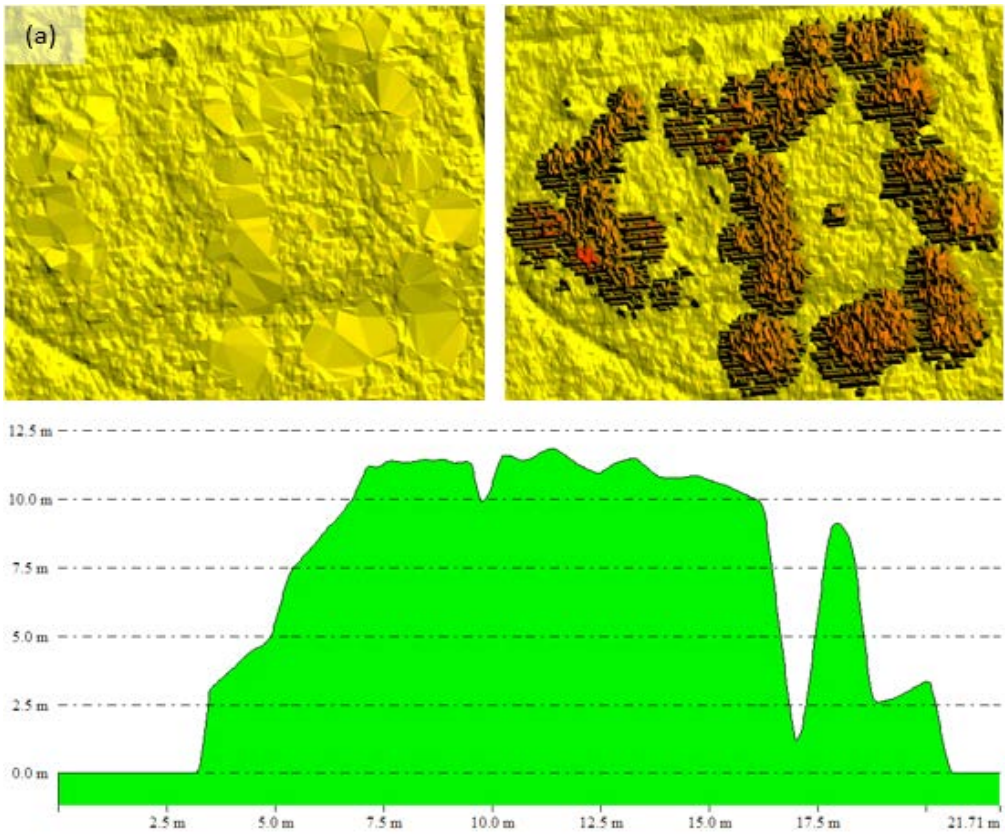
(a)
12.5 m
10.0 m
7.5 m
5.0 m
2.5 m
0.0 m
2.5 m
5.0 m
7.5 m
10.0 m
12.5 m
15.0 m
17.5 m
21.71 m

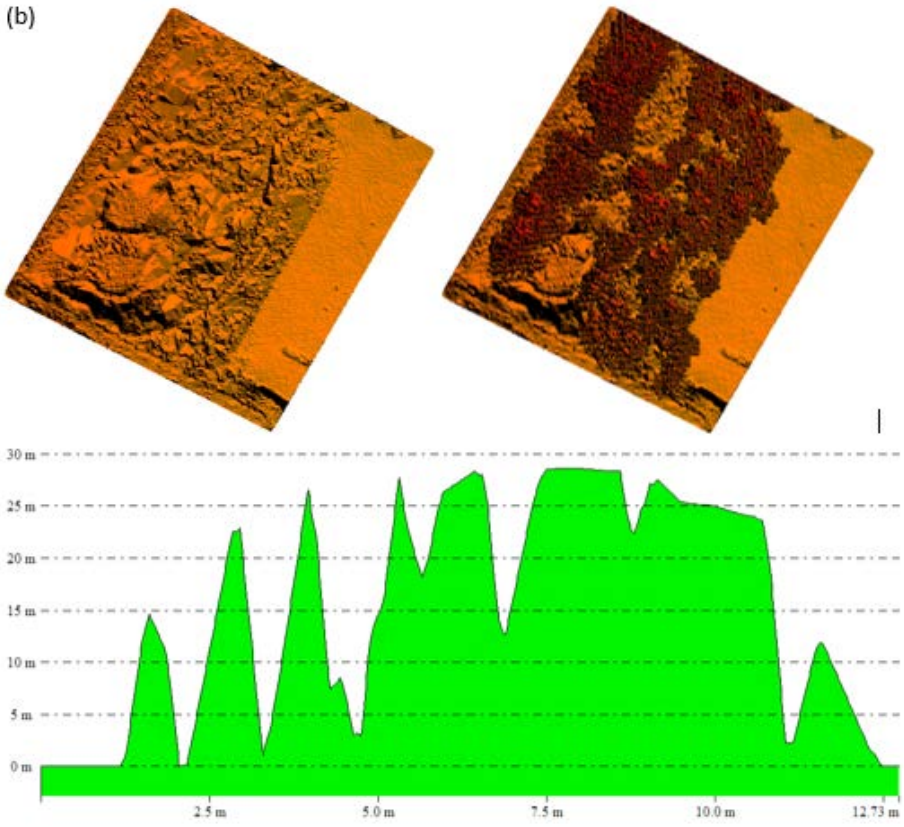
(b)
30 m
25 m
20 m
15 m
10 m
5 m
0 m
2.5 m
5.0 m
7.5 m
10.0 m
12.73 m

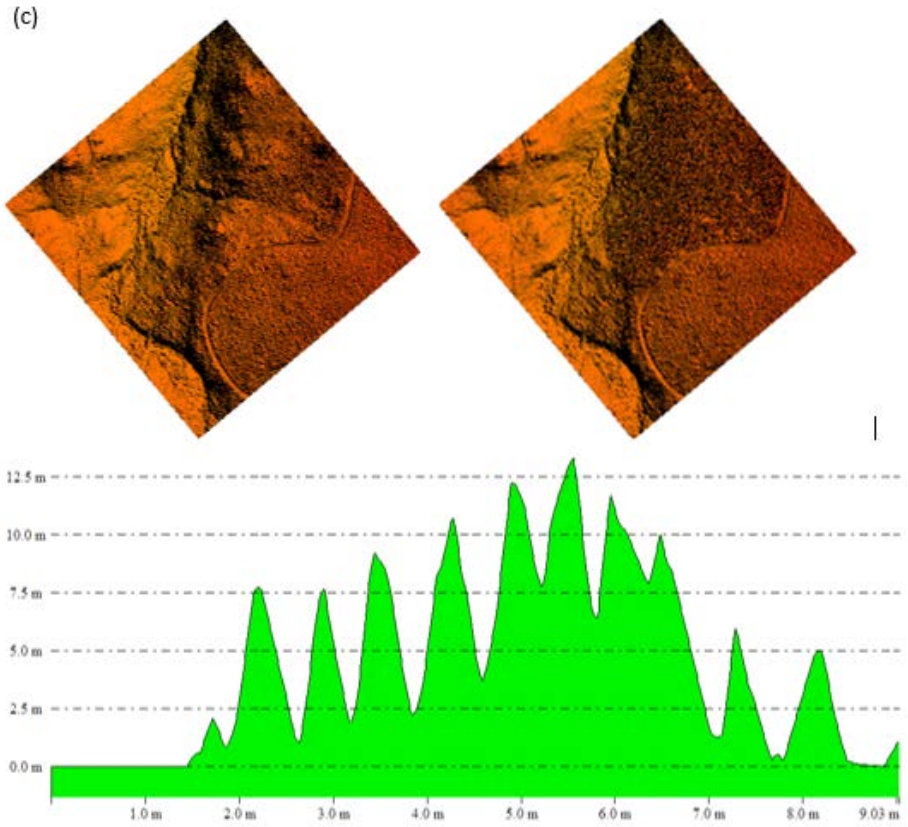

Figure 4.14 | *(a) DSM, DEM and transect through CHM of $H_{omo}FS_1$, (b) DSM, DEM and transect through CHM of $H_{etero}FS_1$, and (c) DSM, DEM and transect through CHM of $H_{etero}FS_2$.* The resulting CHM is a difference between the initial two models. Consisting of a normalised plane i.e. ground level is zero (0 m), this gives the absolute height of the structures in the area.

Extracting the individual tree diameters at breast height required a manual approach within the software, as the algorithm within the software is unable to achieve this. The initial obvious drawback with this approach is that it would be tedious if the number of tree diameters to analyse is large. Since this research endeavour applies a sampling method, this was not the case, with the number of sampled trees in any of the study areas not being more than $n = 50$, a manageable amount to execute manually.

The same procedure for extracting the tree diameters was implemented throughout all the photogrammetric point cloud datasets. To achieve this, the point cloud data was loaded into the workspace and filtered to only display the ground, medium vegetation, and high vegetation points. All the vegetation points above 1.37 m (DBH) from the average ground were selected and temporarily reclassified into a random class, as well as all vegetation

points below 1.00 m above the average ground level. This produced several vertical 0.37 m long stem cylinders of high vegetation points that formed the trunks as was done by Olofsson and Holmgren (2017). These cylinders were used to measure the diameters of the tree trunks.

Circular vector features were created from the visible high vegetation point cloud data by creating 'best-fit' circles of the cylinders that represented the individual tree trunks, as was done in a 2017 ALS and TLS comparison study by Brede et al. (2017) when assessing DBH in *Douglas Fir*, *Old Beech* and *Oak*. Though this method may work for some plant species with trunks that seem averagely cylindrical in structure such as *Pinus radiata*, *Douglas Fir* etc., this may not be the case with all other tree species. Adjustments for a best-fit planar model must be made based on the trunk structure.

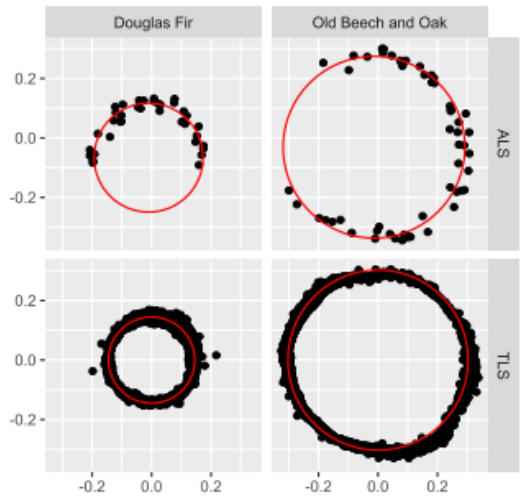

Figure 4.15 | *Image extracted from* (Brede et al., 2017) *showing best-fit circles fitted to the extracted LiDAR points of Douglas Fir, Old Beech and Oak.*

A point feature was then created at the centre of each sample tree circle where the trunks appeared and labelled *Tree_1, Tree_2, Tree_3, Tree_n*…etc. Two distance measurements were taken across the circles, perpendicular to each other, to obtain two diameter readings. Both the readings were recorded in a spreadsheet and the average of the readings was calculated as the diameter of the tree at breast height (DBH). This was repeated for all the analysed trees in the sample data.

Extracting the Tree Height for the selected trees in each of the study areas was achieved using the resulting relative CHMs (*Figure 4.14* above), created and described in *Section 4.3.4.2* above, and a profile tool in Global Mapper project interface. To achieve this, the orthophoto of the relative study area being analysed was overlaid over its relative CHM. This, in conjunction with the tree positions placed, helped more accurately estimate where the position of each of the trees/CHM peak is for a measurement to be obtained. A transect with a swath width of 4.00 m was drawn over the centre of each of the sample trees visible in the overlaid orthophoto. This displayed the structures in a two-dimensional view. Due to the structure of different tree species the swath will have to be adjusted to accommodate any peaks during assessments. For this study, several iterations on the swath width were assessed to determine the adequate value of a 4.00 m swath was wide enough to cover the peak of each tree in case the orthophoto is marginally inaccurate. Minimum and maximum elevation locations in each transect were extracted within the software to create a point at both the lowest and highest points in the transect. This produced the absolute elevation of the sample tree. Another transect was drawn in a perpendicular direction from the previous transect and the highest point reading was observed. Both observations were recorded, and the average of the observations recorded as the absolute TH of the sample tree. This procedure was repeated for each of the sample trees in each of the study area projects.

4.4 ALS Data Acquisition of Tree Variables for Biomass Estimation

Processing and measuring the tree DBH and TH from the acquired low-resolution airborne LiDAR data for all the study areas followed an identical procedure as the one laid out in *Section 4.3.4.2* for photogrammetric point cloud data, with the biggest differences being the naming conventions used to name the various datasets. As this was secondary and acquired data, there was no reconnaissance, flight planning, or data capture phase related to this dataset. The procedure outlined below elaborates how the various measurements were extracted for tree height and tree diameter from the acquired low-resolution LiDAR data for the individual trees across the study areas.

4.4.1 Computing the ALS TH and DBH

Low-resolution LiDAR data acquired from the University of Cape Town, supplied by the City of Cape Town, was used to analyse all three study areas. These were provided in 5 km x 5 km tiles/blocks consisting of LiDAR points. Block W45C covered areas around *$H_{omo}FS$*, block W55D covered areas around *$H_{etero}FS_1$*, while block W08A covered areas around *$H_{etero}FS_2$*. The exception to having one source of airborne low-resolution LiDAR data was *$H_{etero}FS_1$*, which had an additional LiDAR dataset captured using a Riegl miniVUX®-1UAV full waveform LiDAR sensor attached to a DJI Matrice 600 Pro. The data was flown by, and supplied by, Horts Geo-Solutions (www.horts-solutions.com) on the 20th of August 2018.

For each study area, the same naming convention previously used was adopted to help organise data within the Global Mapper project interface. This naming convention followed the sequence: '*Study Area Name_Dataset Source_Capture Date_LiDAR*'. The study area perimeters were used to crop the study areas from the loaded LiDAR data. This was done to reduce the need to process unnecessary data which in turn would greatly reduce processing time. For *$H_{omo}FS$* the cropped LiDAR data was named 'H_{omo}FS_ALS_2017_LAS'. For *$H_{etero}FS_1$* and *$H_{etero}FS_2$* the cropped datasets were named '$H_{etero}FS_1$_ALS_2017_LAS' and '$H_{etero}FS_2$_ALS_2017_LAS' respectively. The additional LiDAR data captured for *$H_{etero}FS_1$*, supplied by Horts Geo-Solutions, was cropped and named as '$H_{etero}FS_1$_UAV_2018_LAS'.

The LiDAR data obtained from the City of Cape Town was in its final product state – all relevant classification had already occurred including classification of points into noise, ground, water, overlap, and unclassified points. However, as mentioned previously, to conform to the classification criteria mentioned in *Figure 3.1*, the unclassified points had to undergo a classification process to obtain vegetation points, as no previously classified vegetation points existed. The unclassified points were classified into both vegetation and building points. The dataset was divided into bin/grids and within these the points were fitted to a calculated best-fit planar surface. Points found close to one another, and that fit this best-fit line, are classified as buildings as they could represent roofs or walls; while points that are far from the best-fit line are classified as vegetation (Blue Marble Geographics, 2017b).

A quick quality control (QC) process was performed on the cropped data, before classification of vegetation points, to ensure that all current and existing points in the dataset were logically classed into the existing classes. *Figure 4.16* below displays the data composition of block W45C, as was obtained, and the various classes.

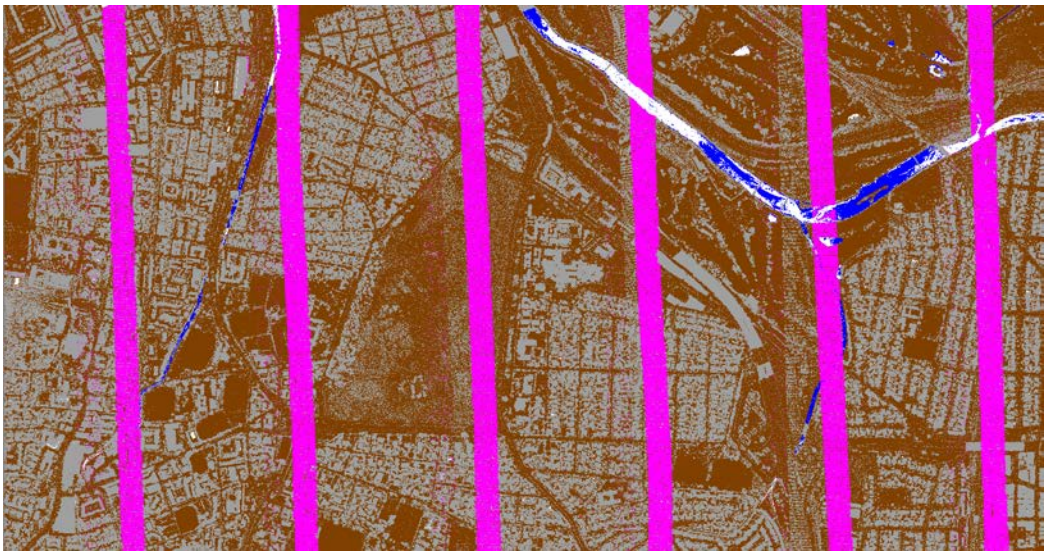

Figure 4.16 | *LiDAR data from block W45C around the $H_{omo}FS$ area. Image shows the different classes present in the dataset at the time of acquisition – brown (ground), blue (water), pink (overlap), red (noise) and grey (unclassified).*

Table 4.10 below presents the vegetation classification parameters used when classifying the LiDAR data in blocks W45C, W55D and W08A for all three study areas. The table also includes the parameters used for the ground and vegetation classification of the Riegl LiDAR data for $H_{etero}FS_1$ as this was obtained unclassified.

Table 4.10 | *Ground and vegetation classification parameters used for ALS_{LiDAR} data*

	Ground Classification			
Parameters	$H_{omo}FS$	$H_{etero}FS_1ALS$	$H_{etero}FS_2$	$H_{etero}FS_1UAV$
Base Bin Size	-	-	-	0.5 m
Minimum Height	-	-	-	0.3 m
Maximum Height	-	-	-	100 m
Terrain Slope	-	-	-	5°

	Vegetation Classification			
Base Bin Size	0.4 m	1 m	0.4 m	*2 point spaces*
Min. Height Above Ground	2 m	0.25 m	2 m	*0.5 m*
Max Co-Planar Distance	0.08 m	0.03 m	0.08m	0.08 m
Min. Vegetation Distance	0.15 m	0.15 m	0.15 m	0.15 m
Max Co-Planar Angle Difference	5°	5°	5°	5°

Using the parameters in *Table 4.10* all vegetation in the ALS LiDAR data for each of the study areas, as well as the ground class in the $H_{etero}FS_1UAV$ data, were correctly classified following similar procedures as stated in Section 4.3.4.2 above. *Figure 4.17*, *Figure 4.18*, and *Figure 4.19* and *Figure 4.20* show the classified LiDAR data for $H_{omo}FS$, $H_{etero}FS_1ALS$, $H_{etero}FS_1UAV$ and $H_{etero}FS_{2,}$ respectively.

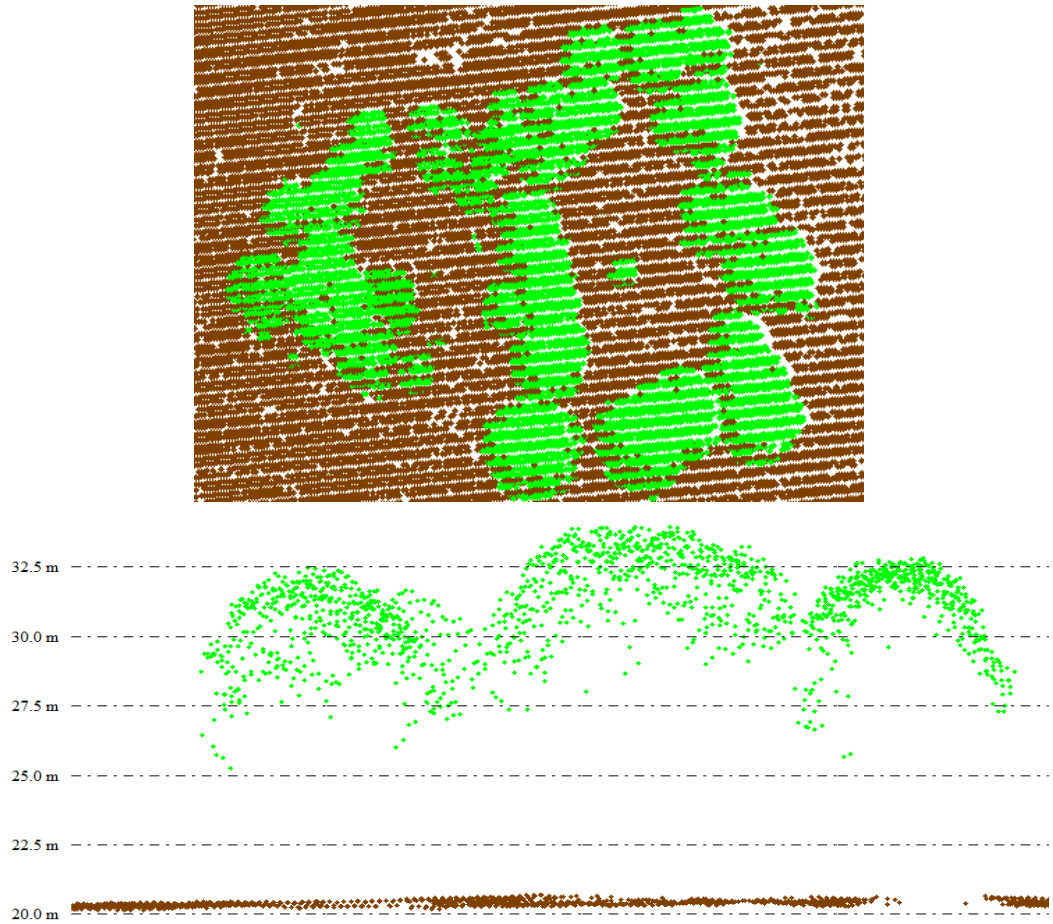

Figure 4.17 | *Classified ALS LiDAR data for $H_{omo}FS$ showing ground (brown points) and vegetation (green points). (a) A top view of the area, and (b) Transect through three trees at the south of the area.*

Though *Figure 4.17* shows a transect of the LiDAR data, an observation was made that there is no LiDAR data captured for the tree trunks, or any sub-canopy structures. A possible explanation for this might be that the scan angle during data collection was too close to nadir, or much too narrow, which rendered it difficult to acquire any under-canopy structures that weren't immediately below the flying aircraft. One possible implication of this is that the 2017 ALS_{LiDAR} data is largely unsuitable for assessing and comparing DBH data for this research endeavour.

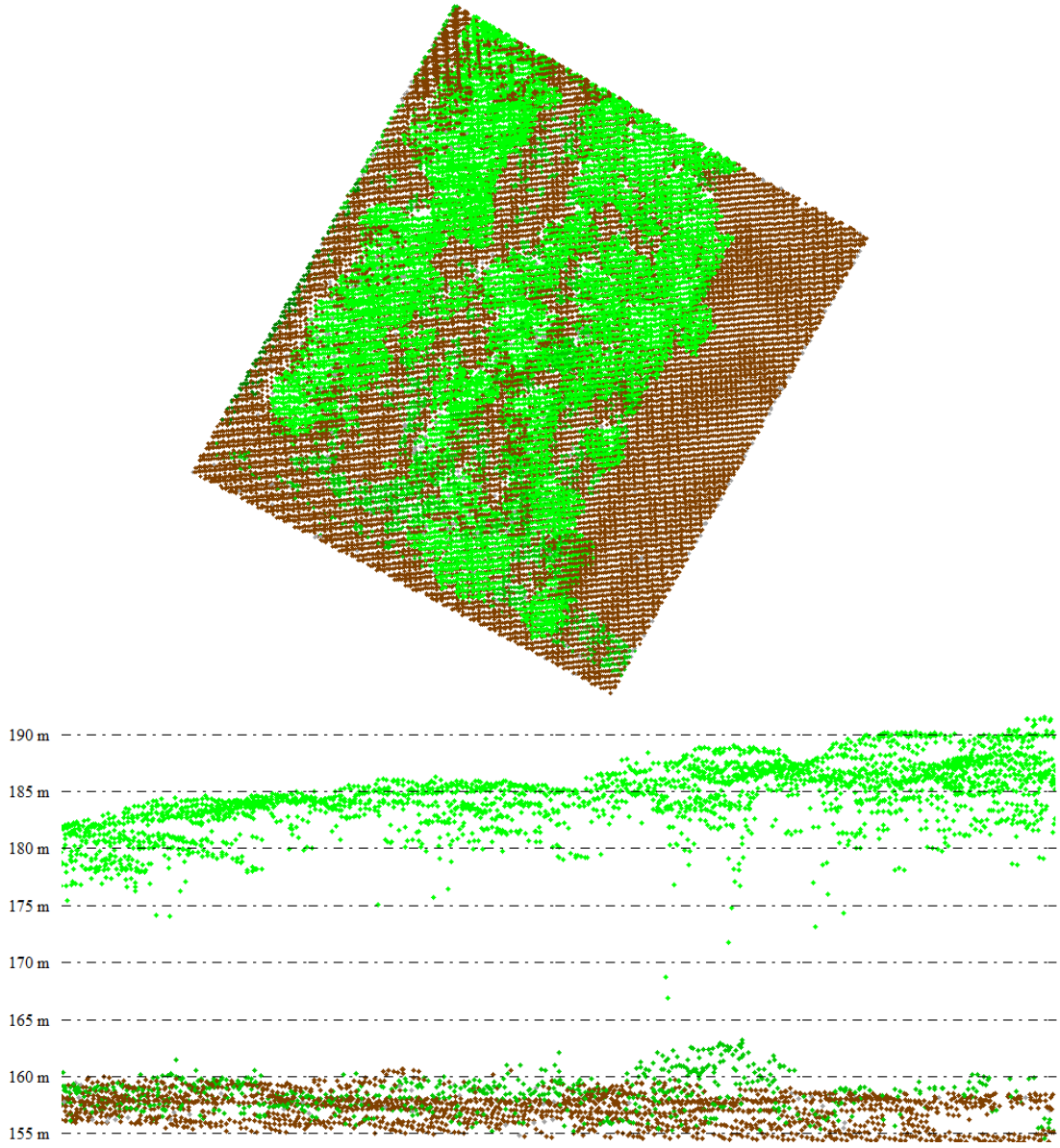

Figure 4.18 | *Classified ALS LiDAR data for $H_{etero}FS_1ALS$ showing ground (brown points) and vegetation (green points). (a) A top view of the area, and (b) a transect through a treeline at the eastern side of the area.*

As with the $H_{omo}FS$ data, indicated in *Figure 4.17*, an inadequate amount of below-canopy LiDAR data was captured to assess and make the comparison to UAV_{SfM} data. This data also proved to be inadequate for assessing DBH. *Figure 4.19* below however shows the classified data acquired from the Riegl miniVUX of the same area.

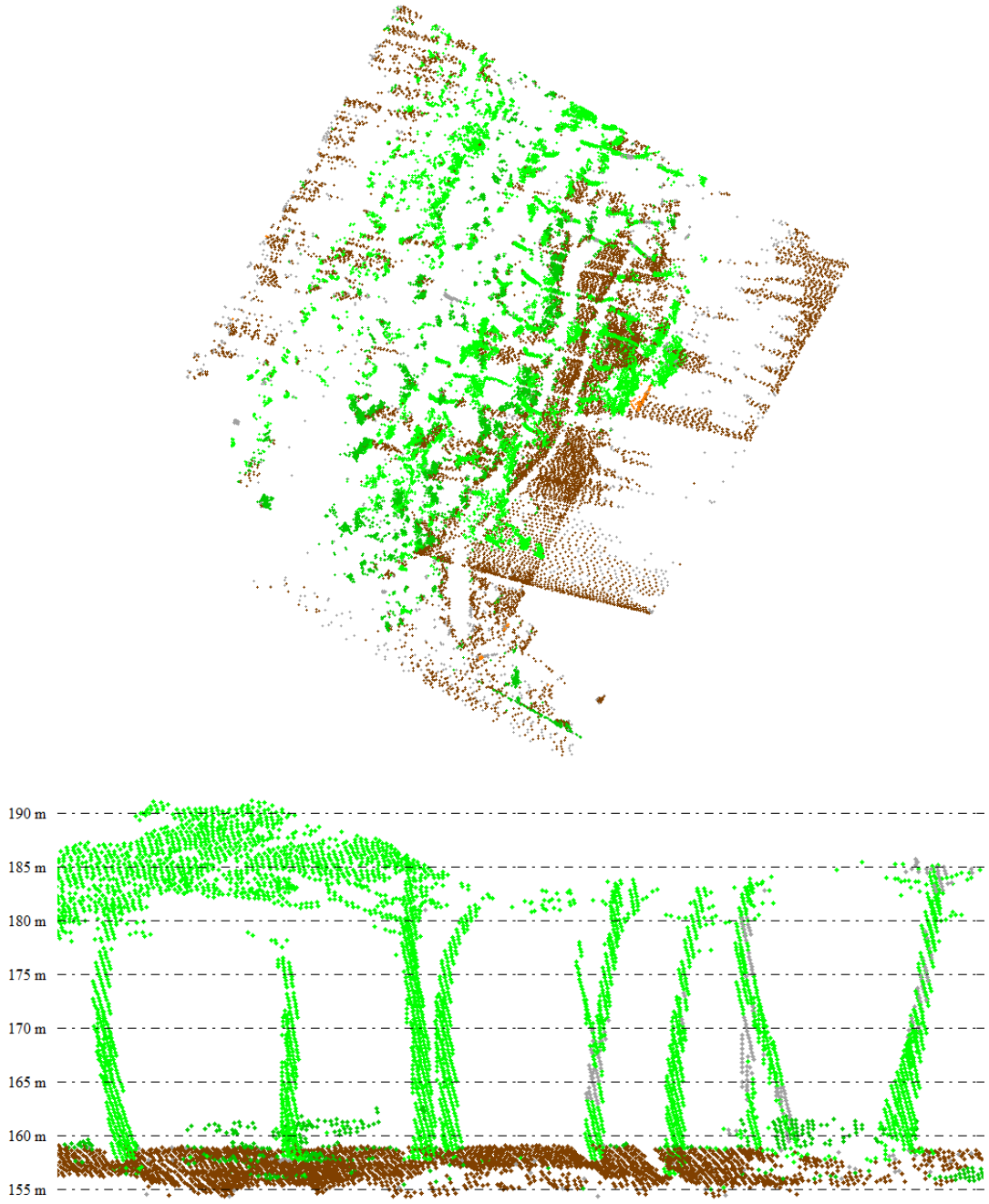

Figure 4.19 | *Classified UAV LiDAR data for $H_{etero}FS_1$UAV showing ground (brown points) and vegetation (green points). (a) A top view of the area, and (b) a transect through the same tree line as in Figure 4.17.*

It should be noted that although the $H_{etero}FS_1UAV$ data was acquired using a Riegl miniVUX®-1UAV laser scanner at less than 120 m AGL the point density is low, a mere 10.977 points/m^2. There are also inadequate ground points and some tree structures seem incomplete as is apparent in *Figure 4.18(a)* above. This contradictory observation may be attributed to the possibility that this study area is on the outskirts of the main focus area of the original survey – which was the survey of the central buildings of the University of Cape Town. This $H_{etero}FS_1UAV$ data was captured at the edges of the scan lines as the UAV moved about its trajectory, thereby creating a sparse and streaky point cloud. Attempts were made to organise the recapture of this area exclusively during the data capture phase of the research endeavour but that was ultimately not possible, and the plan was abandoned. As is apparent in the figures, the LiDAR data provides some below-canopy data but in some areas lacks top-canopy data, an apparent opposite of the $H_{etero}FS_1ALS$ data in *Figure 4.18(b)*. Due to these irregularities, the $H_{etero}FS_1ALS$ data was used to assess TH while the $H_{etero}FS_1UAV$ data would be used to assess DBH data.

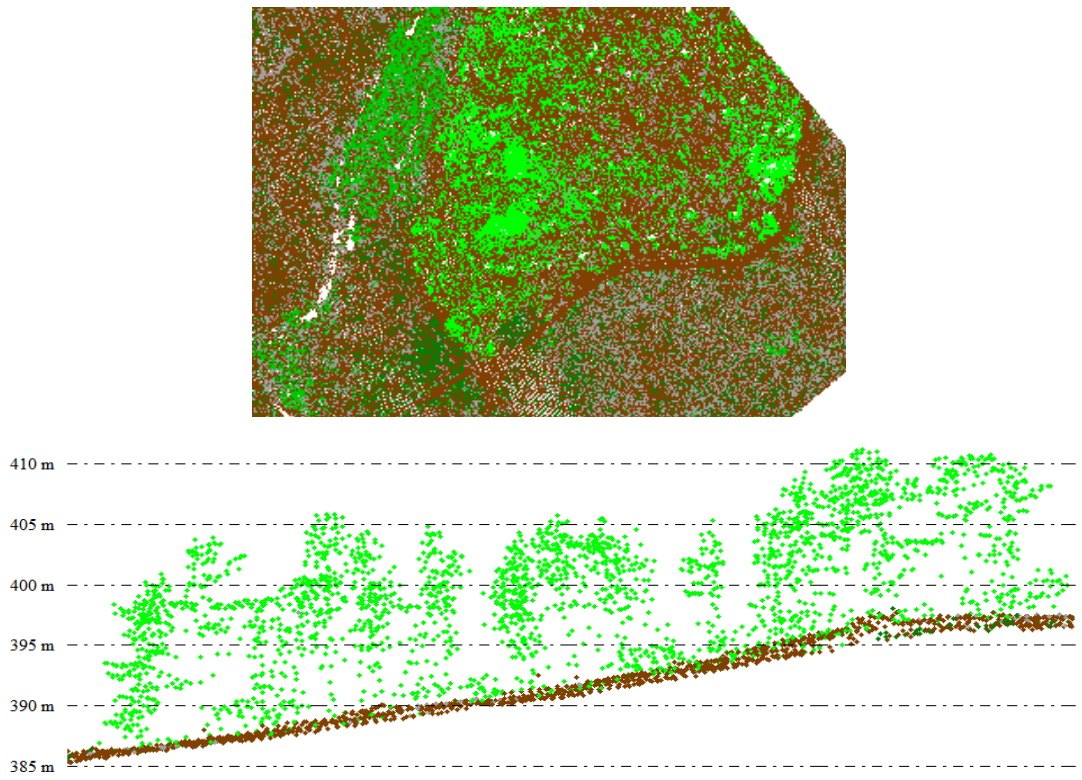

Figure 4.20 | *Classified UAV LiDAR data for $H_{etero}FS_2$ showing ground (brown points) and vegetation (green points). (a) A top view of the area, and (b) a transect through the western edge of the area.*

As in *Section 4.3.4.2*, individual DSMs, DEMs and CHMs were created for each of the study areas using the classified point cloud datasets. DSMs for each of the study areas were created using only the classified ground point. Although there are different gridding methods available, the method used here is Triangulation, which uses a Triangulated Irregular Network (TIN) to connect the numerous points by their known elevations (Blue Marble Geographics, 2017c). The grid spacing/resolution used was 0.10 m as this was sufficiently accurate enough to depict a relatively flat terrain that represents the real-world surface. The naming conventions for the DSMs produced followed a similar sequence as the one stated above: '*Study Area Name_Dataset Source_Capture Date_DEM Type_Ground Resolution'*. The DSM for $H_{omo}FS$ was named 'HomoFS_ALS_2017_DSM_10cm', $H_{etero}FS_1ALS$ is 'HeteroFS_1_ALS_2017_DSM_10cm' and $H_{etero}FS_2$ is 'HeteroFS_2_ALS_2017_DSM_10cm'.

To create the DEMs for the three study areas, the High Vegetation and Medium Vegetation points were used along with the ground points. A grid spacing/resolution of 0.10 m was used to create the Triangulated Irregular Network (TIN) models for the various DEMs. Naming conventions followed the same sequence as with the DSMs. For study area $H_{omo}FS$ the resulting DEM was 'H_{omo}FS_ALS_2017_DEM_10cm', for $H_{etero}FS_1$ the DEM was '$H_{etero}FS_1$_ALS_2017_DEM_10cm' and for $H_{etero}FS_2$ the DEM was '$H_{etero}FS_2$_ALS_2017_DEM_10cm'. Using *Formula 4.2* in *Section 4.3.4.2*, the CHM for each dataset was created and named accordingly - 'H_{omo}FS_ALS_2017_CHM_10cm', '$H_{etero}FS_1$_ALS_2017_CHM_10cm', and '$H_{etero}FS_2$_ALS_2017_CHM_10cm'.

As is evident in *Figure 4.17* and *Figure 4.18* above that although LiDAR information is available for the forest structures there is no abundant below-canopy LiDAR data. The exception being *Figure 4.20* of $H_{etero}FS_2$ which depicts below-canopy LiDAR data. However, the challenge with this particular dataset is that although there is LiDAR data present, it is difficult to identify clear structures that could denote tree trunks, making tree DBH extraction challenging but possible for TH extraction. For this reason, the ALS data acquired from the City of Cape Town was unsuitable for analysing DBH measurements for this research endeavour. *Figure 4.19* displays an image of the Riegl miniVUX®-1UAV data captured of site $H_{etero}FS_1$. The image shows clear and abundant LiDAR data of below-canopy forest structures. This suggests that the data was suitable to use to extract tree DBH.

All the classified vegetation points above 1.37 m (DBH) from the average ground were temporarily reclassified into a random class, as well as all vegetation points below 1.00 m above the average ground level. This produced various 0.37 m stem vertical cylinders of high vegetation points that represented the trunks. Circular vector features within the software were created from the visible high vegetation point cloud by creating 'best-fit' circles of the cylinders that represented the individual tree trunks, as recommended by Brede et al. (2017). Since the tree positions had already been labelled previously, ie. *Tree_1, Tree_2, Tree_3, Tree_n*…etc, distance measurements were taken across the circles, and then again perpendicular to the initial measurement and the averaged to record the average DBH of the trees.

The same procedure was followed, as described in *Section 4.3.4.2* above, for the extraction of TH in the SfM photogrammetric point cloud data. A transect with a swath width of 4.00 m was drawn over the centre of the peak/crown of each of the sample trees visible in the overlaid orthophoto (*Figure 4.21* below). A minimum and maximum elevation location was created at the bottom and at the top of every position a tree was represented on the CHM. This produced the absolute elevation of each sample tree. Another transect was then drawn in a perpendicular direction from the previous transect and the highest point reading was observed. Both observations were recorded, and the average of the observations recorded as the absolute TH of the sample tree. This procedure was repeated for each of the sample trees in each of the study area.

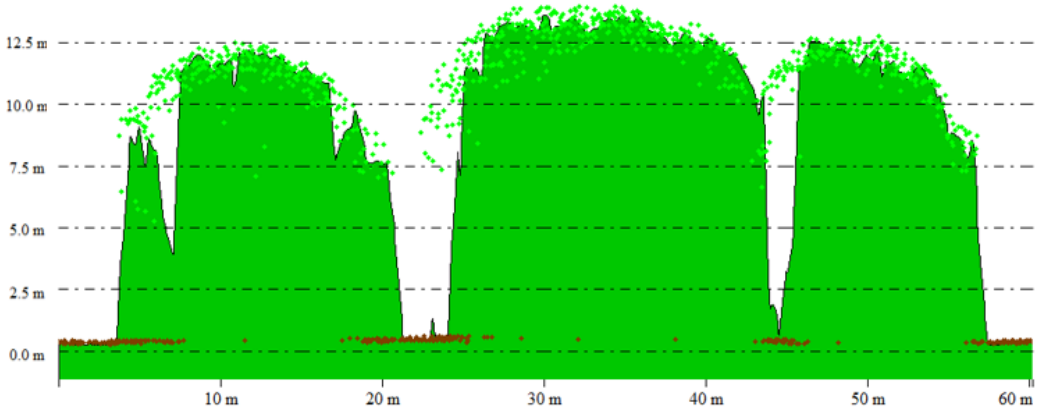

Figure 4.21 | *Transect showing point cloud of three trees over the CHM of $H_{omo}FS$ and their relative TH*

4.5 TLS Data Acquisition of Tree Variables for Biomass Estimation

The TLS survey was conducted to provide comparable data to validate both the ALS and UAV_{SfM} surveys and was conducted at both $H_{etero}FS_1$ and $H_{etero}FS_2$. The data acquired from this endeavour included surveyed and extracted ground control points (GCPs) and targets; and terrestrial laser scans captured using a Z+F Imager® 5010X Terrestrial Laser Scanner (Zoller + Fröhlich, 2020a) on the 26th of April for $H_{etero}FS_2$, and then five days later on the 10th of May 2019 for $H_{etero}FS_1$. However, due to unforeseen circumstances, some of the targets placed on the tree trunks at $H_{etero}FS_2$ were not secure enough and fell off during fieldwork and were only noticed at a later point. In addition to that, rampant subspecies growth below-canopy meant that various obstructions existed between scan positions and the targets; as well as the absence of various distinct features to use as supplementary targets. Another challenge with the survey was that due to the thick forest canopy, the inbuilt GPS unit on the laser scanner lost signal often with satellites, making referencing of scans in real-time quite challenging – a feature most suitable for environments where distinct features are scarce. These challenges meant that the scans could not be registered with high enough accuracy and low enough residuals to constitute an accurate and successful survey, as the forest had several monotonous features that would make distinct feature recognition challenging. The TLS survey for $H_{etero}FS_2$ was thus discarded as a return to site to repeat the survey was also not possible within a reasonable timeframe.

The following sub-sections therefore detail the general workflow and methods applied for the terrestrial laser scanning survey of $H_{etero}FS_1$, and the process from reconnaissance and planning through to analysis and TH and DBH extraction.

4.5.1 Reconnaissance and Planning

A preliminary inspection of the study area was performed to determine the optimal positions for the placement of the targets on the tree trunks. This was done prior to the UAV_{SfM} flight of the area because the targets would play significant roles in both the UAV_{SfM} and TLS_{LiDAR} surveys. The placements of these targets had to be logical and inter-visible from multiple scan locations. A total of 46 targets were used for the survey of the area – two of the original GCPs used in the UAV survey, and 44 newly placed targets. The targets

used in this survey were opposing black triangles printed on white A4 sheets, measuring 210 × 297 mm (*Figure 4.22* below).

Figure 4.22 | *Two of the 44 TLS targets taped to individual tree trunks and features at* $H_{etero}FS_1$

This would enable, after processing the UAV_{SfM} data, for the extraction of the coordinates of the targets to register the terrestrial scans later. This approach was chosen to reduce the overall time spent in the field if a Total Station were included in the endeavour to survey and extract the coordinates of the targets. Several other features in the area where also observed to serve as reference features for the scans, including several storage containers in the parking lot. Possible scan locations and paths through the trees to achieve these scans were identified. It should be noted that two observations were made after this phase of the research endeavour –

- Wrapping the targets around the tree trunks with tape did not offer much stability as in some cases, eventually, the tape would either dry up and loosen their bonds on the tree causing the targets to unwrap and thus not be flush with the trunk surface which could hamper accuracies when being surveyed. Press-tacks would have offered a more stable solution for holding the targets up.
- An unnecessary number of targets were used for this phase. No more than 6 targets would be enough to register the entire survey given the scale (González-Jaramillo, Fries and Bendix, 2019). This is also attributed to the fact that the scanner has an internal GPS and IMU unit that both assist with orientation and pre-registering the scans in the field.

4.5.2 Data Capturing

A total of 13 scans, K1 to K13, were acquired during this survey, each from levelled instrument of 1.75 m instrument height. Because it was necessary to obtain as detailed as possible a scan of the trees and surroundings, all scans were scanned at high intensity, though this is not common practice for scanning closer objects. On this setting the rotating mirror spins faster, and the pulse emitter emits a stronger energy beam, which makes this setting more suited for scanning structures further away. Higher density scans are also a function of high intensity scans. *Figure 4.23* below shows the path through the site from the first scan to the last. Each consecutive scan position, about 16 m apart, had common targets to help with registration later and connect each scan to one another.

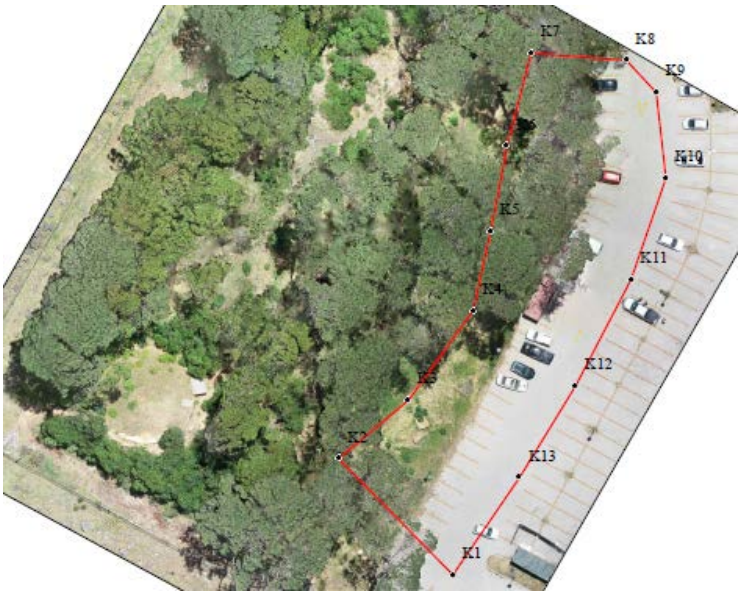

Figure 4.23 | *Scan positions K1 to K13 (black dots) and the traverse (red line) of the TLS survey at* $H_{etero}FS_1$

The Z+F Imager® 5010X Terrestrial Laser Scanner comes equipped with both an internal GPS and IMU, enabling scans to be registered in real-time to an accuracy of a few centimetres (Zoller + Fröhlich, 2020a). However, the inclusion of registering with targets post-survey adds millimetre accuracy registration to provide a seamless cloud. Both the GPS and IMU were active and recording during the time of data capture.

4.5.3 Processing

Several software were used to process the scans from the conclusion of the data capture phase (registration in Z+F LaserControl® v6.0.0), to the point where feature measurement extraction was possible (Blue Marble Global Mapper v20.1). This section discusses in further detail the procedure followed.

Z+F LaserControl® v9.0.2.24038 (Zoller + Fröhlich, 2020b) was used to register the scans. Since the laser scanner has an internal IMU and GPS the scans had relatively accurate orientation, however in the software interface the scans had to be moved and rotated slightly to assist the software in registering the consecutive scans. As registration is the initial step in processing point cloud and three-dimensional modelling (Lachat, Landes and Grussenmeyer, 2018), this stage is crucial to the overall quality of the dataset because if any significant errors exist, they can easily propagate and/or increase through the dataset. Most software register the data, which consist of several point clouds (global registration), by either using targets to register the data, or by finding patterns in the several features that exist in the scene, or a combination of both. For this reason, sufficient overlap must exist between adjacent scans.

The registration typically consists of a three-dimensional similarity transformation (*Formula 4.3*, suggested by Lachat, Landes and Grussenmeyer (2018) which is applied to several point clouds to transform them to the reference frame. A 6 or 7 parameter similarity transformation is usually used and depends on whether there is a scale factor and if such said scale factor is uniform in all directions (Lachat, Landes and Grussenmeyer, 2018).

$$X_i^B = R_{A\to B}\, X_i^A + t_{A\to B} \tag{4.3}$$

where $X_i = [x_i y_i z_i]^T$ are three dimensional coordinates in either A or B, $R_{A\to B}$ is a 3 x 3 orthogonal matrix, and $t_{A\to B} = [t_x t_y t_z]^T$ is a translation vector.

At each scan position every visible target was identified and at the centre where the opposing triangles meet the target name was placed and assigned. It was imperative that at least two targets from each scan position shared a line of sight from consecutive scan locations to assist with cloud-to-cloud registration. To add more reference points to the

scans, various features and surfaces in the scene were referenced as supplementary targets. *Figure 4.24* below shows some of the targets, as well as some of the features, used during registration of the scans.

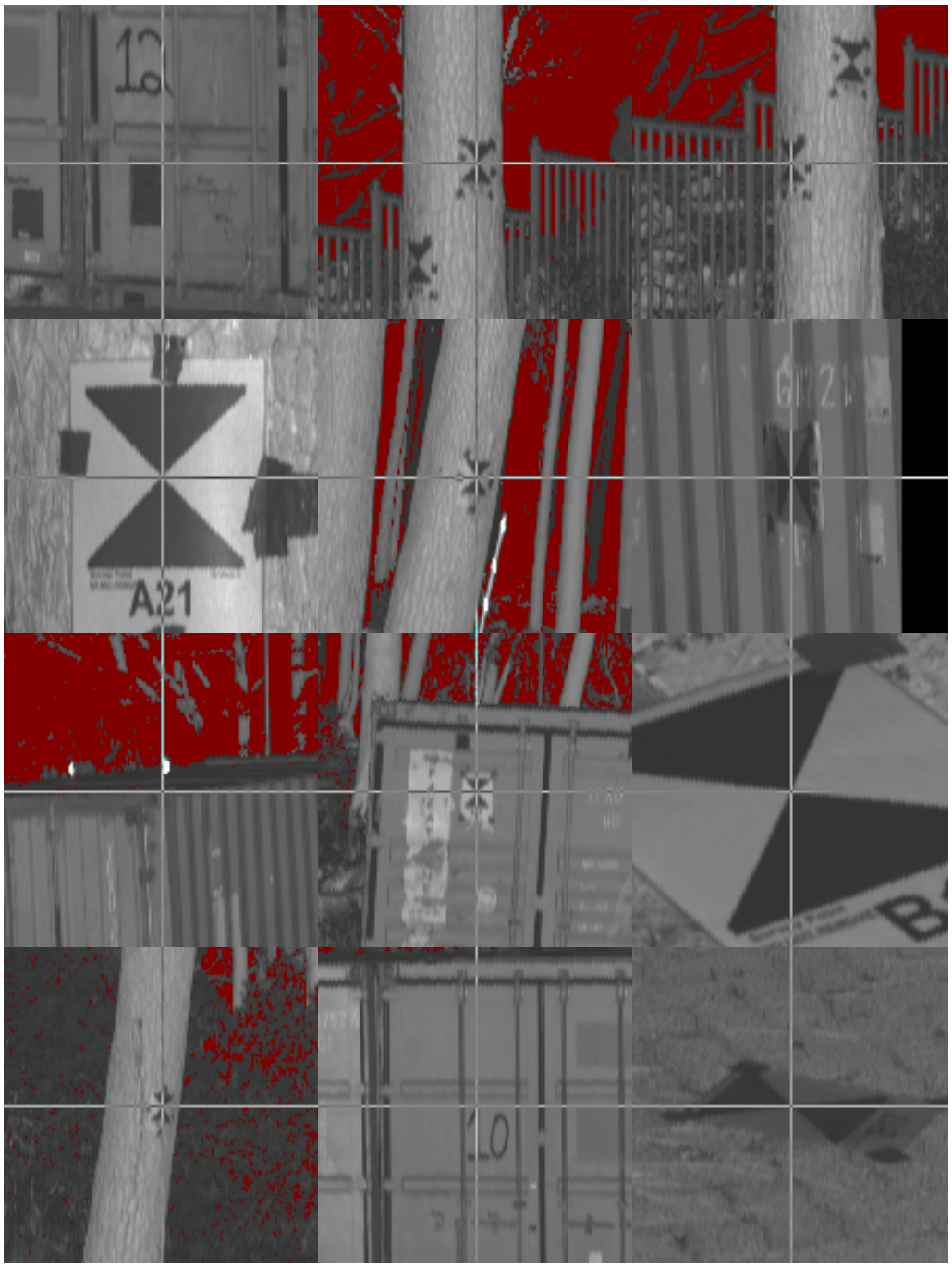

Figure 4.24 | *Several targets and reference features scanned during the fieldwork and referenced within the Z+F LaserControl software interface during registration of the scans*

The registration process is generally performed in a two-prong process – coarse and fine alignment. Part of the coarse alignment involves manually rotating and aligning some of

the scan positions the scanner had failed to align to within centimetre accuracy. Since the Z+F Imager® 5010X pre-aligns the point cloud during fieldwork, the clouds are finely registered using an Iterative Closest Points (ICP) algorithm which attempts to minimise the difference between two sets of point cloud. The table below displays the accuracy of the overall registration endeavour.

Table 4.11 | *Statistics on the TLS registration of $H_{etero}FS_1$*

Total number of targets (A4 sheets and supplementary features)	148
Number of disabled targets	5
Average Deviation	15.1 mm
Standard Deviation	8.5 mm
Maximum Deviation	48.5 mm

These accuracies were accepted as adequate for the purposes of the survey, with the average deviation being 15.1 mm/1.51 cm, and the maximum deviation being 48.5 mm/4.85 cm.

The removal of excessive noise points, unwanted objects in the scans and the compilation of all the scans into one composite scan was done in Autodesk Recap v6.0.0. All the scan positions were indexed and loaded into a singular workspace and interface. *Figure 4.25* below shows a seamless composite point cloud consisting of all 13 TLS scan positions for $H_{etero}FS_1$.

Figure 4.25 | *Composite TLS LiDAR scan of $H_{etero}FS_1$ showing tree trunks and other vegetation in the area*

Erroneous points in the cloud caused by backscatter from particles such as dust were cleaned manually deleting them within the project space. *Figure 4.26 (a)* shows some of these erroneous points in the dataset, enclosed in blue rectangles. These noise points in the dataset can occur frequently in areas with high dust, water vapour content, or even glossy leaves on vegetation as these refract the laser beams to or from the sensor. Unnecessary features from the cloud such as the cars in the parking lot, streetlamps, and shipping containers found on site were also deleted from the dataset as they served no purpose.

Figure 4.26 | *(**a**) Erroneous points (in blue boxes) present in the dataset. These points are most likely a result of backscatter caused by heavy presence of dust in the area during scanning, (**b**) Structures present in the point cloud – cars, shipping containers, streetlamps – prior to being removed.*

4.5.4 Computing TH and DBH

This section details the modelling and analysis of the LiDAR data acquired during the TLS survey of $H_{etero}FS_1$, as well as the classification of the LiDAR data, and through to the extraction of the various measurements required. Some of the challenges encountered during processing the data are also discussed here.

All 103 337 988 points of the composite LiDAR scans were to be used to during the analysis. The point cloud had a point density of 55 102 points/m^2, and a point spacing of 0.004259 m. The point cloud was subject to the standard naming convention so far adopted for this research endeavour, '*Study Area Name_Dataset Source_Capture Date_LiDAR*'. As such the TLS LiDAR data was named 'HeteroFS1_TLS_2019_LiDAR'. Since neither Z+F LaserControl nor Autodesk Recap employ a classification algorithm on the point cloud data, all points present during the initial analysis were thus unclassified.

One of the immediate shortcomings of the data acquired was that, when viewed from a top view in Global Mapper, the data lacked detail on the north to north-western region of the study area (blue polygon in *Figure 4.27* below). A possible explanation for this shortcoming is the absence of a TLS traverse around this area resulting in insufficient data acquired during the data collection phase to provide ground and vegetation points to assist in creating both a sufficient DSM and DEM. This lack of sufficient coverage (*Figure 4.27* below) meant that this particular dataset could not be used to produce the CHM requisite for extracting TH for all trees present in the dataset, but only the areas with enough ground points and vegetation points to create the necessary models. Both the TLS TH data, and the ALS TH data acquired and processed, mentioned above in *Section 4.4.1* were compared to the SfM TH data, while the TLS data was used for the extraction of the DBH data where possible. The immediate area of interest thus was reduced further to the area around the trees in this dataset that coincided with the trees in both the ALS and SfM datasets (red polygon in *Figure 4.27* below). As this research endeavour tests SfM acquisition of trees for biomass estimation by sampling trees in various datasets, this was not deemed as detrimental to the success of the research.

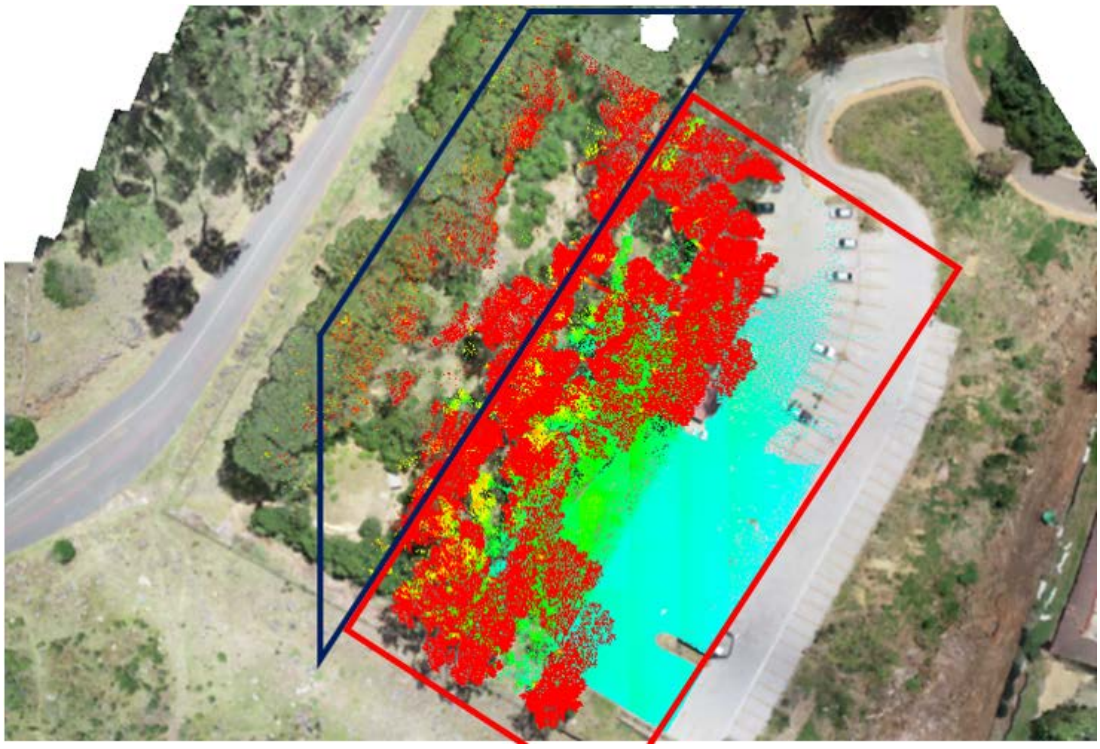

Figure 4.27 | *Point cloud colourised by Height Above Ground overlaid on an orthomosaic showing the section of $H_{etero}FS_1$ with missing TLS LiDAR data (blue polygon)*

In alignment with previous practices so far in the research endeavour, and with the selection criteria outlined in *Figure 3.1* in Chapter 3, the LiDAR data was classified to yield both ground and vegetation points. It was determined that an approximate relative 40 m difference exists between the ground and the highest feature, the tallest tree within the study area. Noise points were classified as all points below 1 m from the average ground height, or the last return in the data, as well as all points above 42 m from this average ground level, with a maximum allowed variance from the local average of 3 standard deviations. Points further than the indicated standard deviations from the average were identified as noise points and classified as such. Classification of the remaining unclassified points to ground points was done by searching each individual point and all points within a search area/grid of 1 m x 1 m and fitting those points to a preliminary calculated three-dimensional curve based on the available points. To improve the accuracy, the algorithm was restricted to only search and classify points within 0.30 m of the average points and consider only points within a terrain slope angle of 5° because the terrain is relatively flat. All points within this search criteria were classified as ground, while points that were identified to be outside the criteria remained as unclassified points. The table below highlights the parameters used during the classification of the TLS dataset for $H_{etero}FS_1$.

Table 4.12 | *Parameters used during Ground and Vegetation classification of $H_{etero}FS_1$ TLS LiDAR Data in Blue Marble Global Mapper*

Ground Classification	
Base Bin Size	1 m
Minimum Height	0.3 m
Maximum Height	50 m
Expected Terrain Slope	5°
Vegetation Classification	
Base Bin Size	0.4 m
Minimum Height Above Ground	1 m
Max Co-Planar Distance	0.08 m
Minimum Vegetation Distance	0.15 m
Max Co-Planar Angle Difference	5°

The trees and other vegetation in the area were also classified using the parameters indicated in *Table 4.12*. The classification procedure followed the same procedure as was done with classifying vegetation points in both the ALS and SfM datasets. A QC was performed to assess that all points in the dataset were adequately classified.

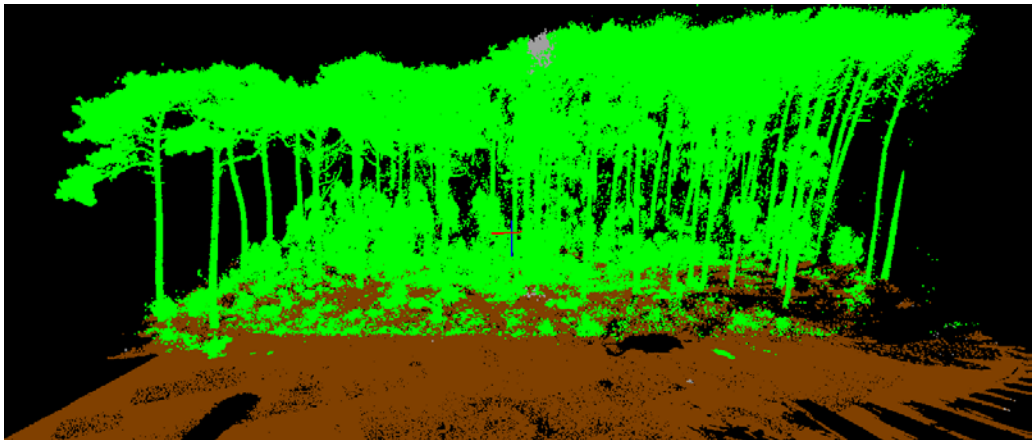

Figure 4.28 | *$H_{etero}FS_1$* point cloud classified into ground (brown) and vegetation (green)

The same procedure for extracting the tree diameters implemented when extracting DBH for both the SfM and ALS data was implemented here. To achieve this, only the ground and vegetation points were used. All the vegetation points above 1.37 m (DBH) above the average ground level were selected and temporarily reclassified into a random class, as

well as all vegetation points below 1.00 m above the average ground. This gave a 0.37 m cylinder of points in the vegetation class to form the trunks of the tree.

Circular vector features were created from the loaded point cloud that resembled the circular trunks of the trees. Best-fit circles were created around the point cloud that resembled the individual tree trunks. Two perpendicular measurements were taken across each circle to obtain two diameter readings. Both the readings were recorded, and the average of the readings was calculated as the diameter of the tree at breast height (DBH). This was repeated for all the labelled trees with circular vector data indicating a tree trunk. *Figure 4.29* below displays the best-fit circles that were created using the vegetation point cloud, which is similar to the technique that Brede et al. (2017) used in a similar study.

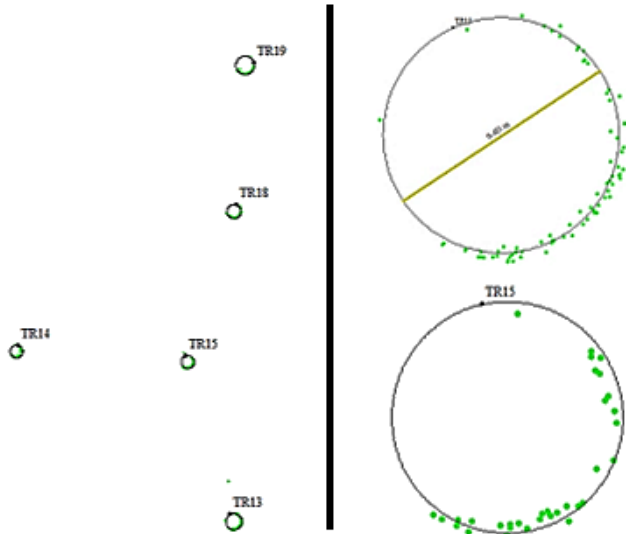

Figure 4.29 | *Best-fit vector data and DBH extracted from the tree vegetation point cloud of* $H_{etero}FS_1$. ***Left*** *– Five trees clumped together,* ***right*** *– close view of Tree 13 with measurement across for DBH (0.481 m) and Tree 15*

4.5.5 Considerations with UAV_{SfM} Acquisition of Forest Structures

The study highlights the efficacy of multi-rotor UAVs in capturing data for photogrammetric point cloud assessment of forest structures. Beyond the obvious limitations such as battery power and flight restrictions, the multi-rotor UAV was able to capture imagery at proximity to the forest face using low flight altitudes, and oblique flight patterns, but especially with the use of the tessellated façade flight pattern. Other factors that abet improved accuracies include proper planning, gridded flight patterns, higher-resolution cameras, and flying at optimal atmospheric conditions (little to no wind, high noon) to name a few, including

image overlap. These affect the temporal, spectral and spatial resolution of the data, all of which affect the accuracy of which canopy and below-forest structures are reproduced.

In this study, UAV_{SfM} was assessed for its efficacy in estimating homogeneous and heterogeneous *Pinus* forest structures for biomass estimation, and by extension, forest inventory etc. This was done by comparing UAV_{SfM} to LiDAR data acquired from three different platforms – an aerial laser scanner aboard an aircraft, a terrestrial laser scanner, and a laser scanner aboard a UAV (ALS_{LiDAR}, TLS_{LiDAR}, and UAV_{LiDAR} respectively) – to see if UAV_{SfM} is a suitable alternative to LiDAR data for forest inventory and assessment purposes. However, these are two innately different technologies and techniques in that LiDAR uses laser beams that penetrate through the small gaps in forest canopy or surrounding vegetation, and UAV_{SfM} uses RGB imagery to produce stereo models and thus reproduce photogrammetric point cloud of the scene. As such, analysis and scrutiny of data must be done with caution, and with a consideration of accuracy requirements and purpose of the data in mind.

Validating UAV_{SfM} data therefore becomes paramount to assessing its efficacy in capturing forest structures but validating the accuracies of photogrammetric results is challenging, especially when validating them against field measurements as it is challenging producing three-dimensional structures using field measurements alone, owing to the conventional ways they are obtained. For this reason, and that LiDAR data is generally more accurate (Iglhaut et al., 2019), LiDAR data was used to validate the photogrammetric point cloud. Another key challenge with UAV_{SfM} is image overlap. To recreate a sufficient model, excess imagery from multiple perspectives is necessary to create a seamless photogrammetric model of all structures in the scene. This was especially challenging in this study when attempting to acquire imagery of the tree trunks, especially at $H_{etero}FS_1$ which is a dense forest structure that presents multiple challenges for data acquisition using a UAV. Although attempts were made to capture the below-forest structures from the front and sides of the forest face, images should be captured from within the forest boundary itself as well to cover various perspectives of each tree trunk.

The results obtained from measuring the DBH and TH of the trees in $H_{omo}FS$, $H_{etero}FS_1$ and $H_{etero}FS_2$ using the SfM, ALS and TLS data and their comparisons are presented in the next chapter, Chapter 5: Results and Discussion.

CHAPTER 5

Results and Discussion

5.1 Results

This chapter outlines the results obtained during the experiments performed throughout the research endeavour, in line with the aims and objectives stipulated in Chapter 1. The results reflect the comparison of Unmanned Aerial Vehicle Structure-from-motion photogrammetric data (UAV_{SfM}) to Terrestrial Laser Scanner data (TLS_{LiDAR}), Aerial Laser Scanner data (ALS_{LiDAR}) and Unmanned Aerial Vehicle LiDAR data (UAV_{LiDAR}) throughout two *Pinus* forest structures, namely Homogenous Forest Structure ($H_{omo}FS$), and Heterogeneous Forest Structure 1 ($H_{etero}FS_1$). Results for Heterogenous Forest Structure 2 ($H_{etero}FS_2$) are excluded from this chapter as results from both the ALS_{LiDAR} and UAV_{SfM} surveys for the site were structurally inadequate. The ALS_{LiDAR} data obtained could produce a CHM but extracting the tree heights was challenging as some trees were to close together to distinguish the individual trees within the data. Conversely, tree trunks were not reproduced adequately due to the low point density, as such the DBH could not be extracted. The discussions section of this chapter further discusses the results obtained for $H_{omo}FS$ and $H_{etero}FS_1$, as well as offers possible explanations and interpretations for the results.

5.1.1 Evaluating the utility of UAV_{SfM} datasets to TLS_{LiDAR}, ALS_{LiDAR} and UAV_{LiDAR}

To evaluate the utility of UAV_{SfM} derived point cloud data against the other data derived from LiDAR sensors in this research, various statistical tools were applied. Pearson's correlation (Pearson's *R*) (Maina, Odera and Kinyanjui, 2017; Jayathunga, Owari and Tsuyuki, 2018; Kachamba et al., 2016), provided in *Formula 5.1* below, was used extensively on the results to measure how well the various LiDAR datasets relate to their UAV_{SfM} dataset counterparts – the strength of the relationship between both variables. The correlation coefficient formula shows a linear relationship between two sets of data being compared.

$$r = \frac{n(\Sigma xy) - (\Sigma x)(\Sigma y)}{\sqrt{[n\Sigma x^2 - (\Sigma x)^2][n\Sigma y^2 - (\Sigma y)^2]}} \quad (5.1)$$

where n is the total population number; x represents UAV_{SfM} DBH or TH values; and y represents the various LiDAR dataset DBH or TH values. The accuracy of Pearson's *R* obtained for the DBH and TH data was validated using the leave-one-out cross validation (CV) technique as suggested by Jayathunga, Owari and Tsuyuki (2018). The Root Mean Square Error (RMSE) of the data was also determined using the following formula –

$$RMSE = \sqrt{\frac{\Sigma_{i=1}^{n}(y_i - \hat{y}_i)^2}{n}} \tag{5.2}$$

where n is the number of samples, y_i; is the observed LiDAR DBH or TH value; and $\hat{y}_i$ is the UAV_{SfM} DBH or TH value. This was done to evaluate the average separation from the best-fit line of each sample measurement.

5.1.2 General UAV_{SfM} and LiDAR Point Cloud Properties Observed from Results

Transects of points through parts of $H_{omo}FS$ and $H_{etero}FS_1$ are shown in *Figure 5.1* for illustration purposes. In general, photogrammetric point cloud was limited in that, in certain areas, it was unable to reconstruct some structures that are either below-canopy, or that were covered by extensive forest canopy or other structures. This created gaps in the dataset, unlike LiDAR which could penetrate small gaps in forest canopy and gaps between below-canopy forest structures to render ground points, which are crucial for the production of accurate DSMs (Kachamba et al., 2016). Because the ALS_{LiDAR} datasets utilised in this research endeavour are low-resolution LiDAR data, the number of ground points were much lower compared to photogrammetric point cloud as they had a low point density but succeeded at reproducing the ground area a lot more effectively as compared to photogrammetric point cloud. This is because effectively reproducing ground using the latter data for an area is a function of the survey area having large open spaces that are clearly visible from the air through the camera and free of low vegetation such as grass and other obstructions.

The point density in the photogrammetric point cloud was also generally much denser than the low-resolution LiDAR and as such when sufficient imagery of the forest structure was captured from multiple unobstructed perspectives (tessellated façade) produced rich point cloud capable of adequate feature extraction of tree trunks. However, this advantage can

be lost should there be any obstructions such as below-canopy shrubs or subspecies in front or near the tree trunks, or inadequate images of the scene to properly provide a multi-view perspective of the structures.

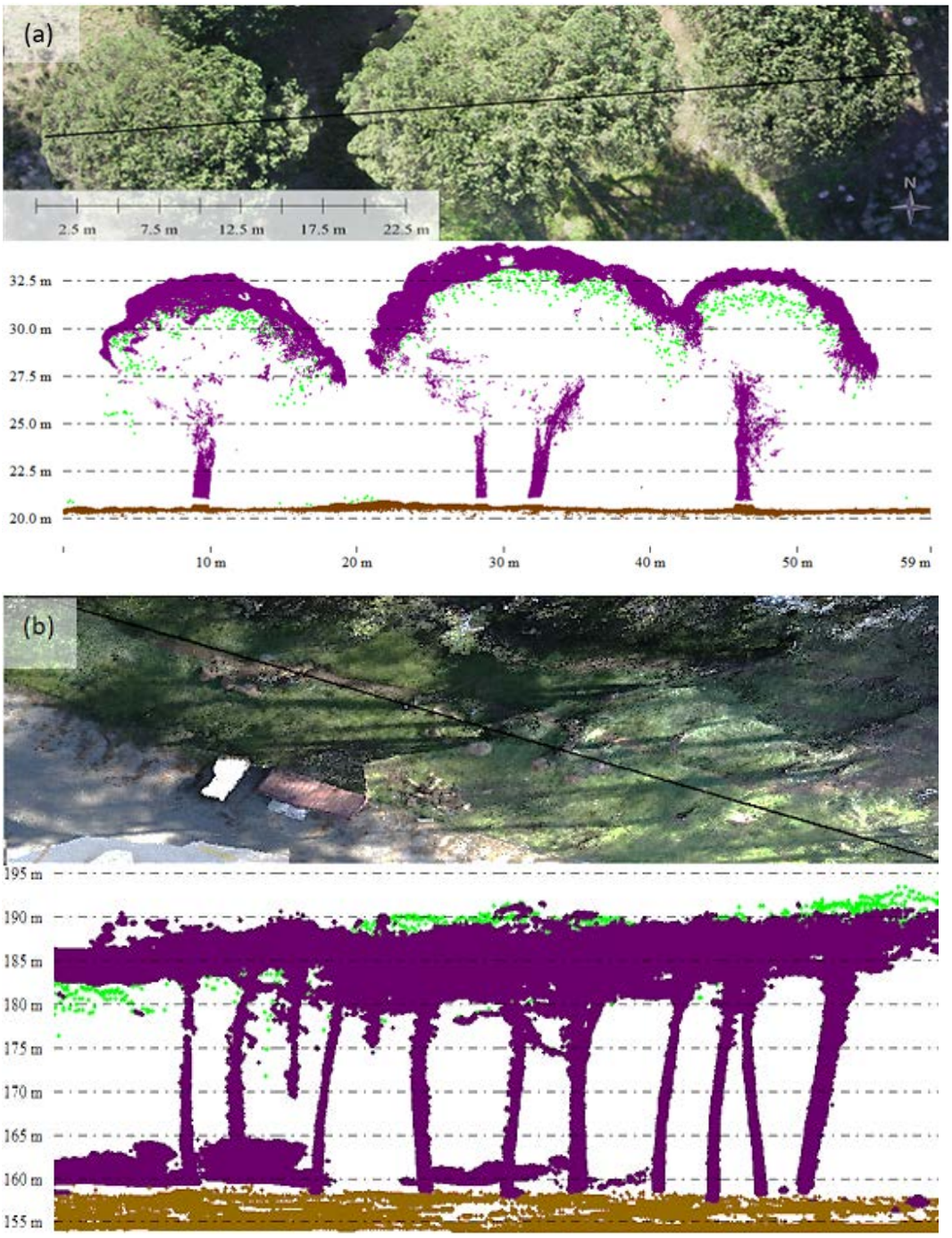

Figure 5.1 | *UAV_{SfM} vegetation (purple points), ALS_{LiDAR} vegetation (green points), and ground points in both datasets (brown). (**a**) Transect through section of $H_{omo}FS$; and (**b**) Transect through section of $H_{etero}FS_1$.*

Figure 5.1(b) above illustrates how dense the UAV_{SfM} is compared to the ALS_{LiDAR}, dense enough to reproduce tree trunks. The ALS_{LiDAR} data was unable to reproduce any below-canopy forest structures. The figure also illustrates that in some areas the UAV_{SfM} data reproduced the treetops on par with the LiDAR data, and in some areas did not. This is most likely a function of SfM photogrammetry's limitation at reconstructing monotonous vegetative surfaces.

5.1.3 UAV_{SfM} against TLS_{LiDAR}, UAV_{LiDAR} and Field Measured DBH

UAV_{SfM} DBH measurements were compared to field measured DBH values at $H_{omo}FS$ using a total of 32 sample trees in the area, while at $H_{etero}FS_1$ the same comparison was done but with TLS_{LiDAR} and UAV_{LiDAR} DBH data using 20 sample trees in both instances. For the former comparison, a generally adequate coefficient of determination of R^2 = 0.5955 (59.55%) was obtained, signifying a medium correlation. A stark difference between the variables in the UAV_{SfM} against field measurements comparison, minimum difference of 0.008 m, and the maximum difference of 0.438 m, is suggestive of challenges in reconstructing full and accurate tree trunks in various instances using photogrammetry – a function of inadequate scene coverage caused by insufficient image cover from multiple perspectives. For the latter comparison, $H_{etero}FS_1$, an adequate agreement of R^2 = 0.5237 (52.37%) was also obtained when comparing UAV_{SfM} DBH to TLS_{LiDAR} DBH, while a poor agreement of R^2 = 0.1114 (11.14%) was obtained when comparing UAV_{SfM} DBH to UAV_{LiDAR} DBH.

The UAV_{SfM} DBH against UAV_{LiDAR} bar chart below highlights the disparity between the two datasets. In it, there is a stark difference in measurements for *Tree 3*, while *Tree 4* and *Tree 9* DBH were not measured in the UAV_{LiDAR} data. This was because the UAV_{LiDAR} data acquired failed to properly acquire the full extent of *Tree 3*'s trunk making extraction of the actual diameter challenging, while LiDAR data for *Tree 4* and *Tree 9* were unavailable altogether. The low resolution of the UAV_{LiDAR} data is shown below in *Figure 5.3*.

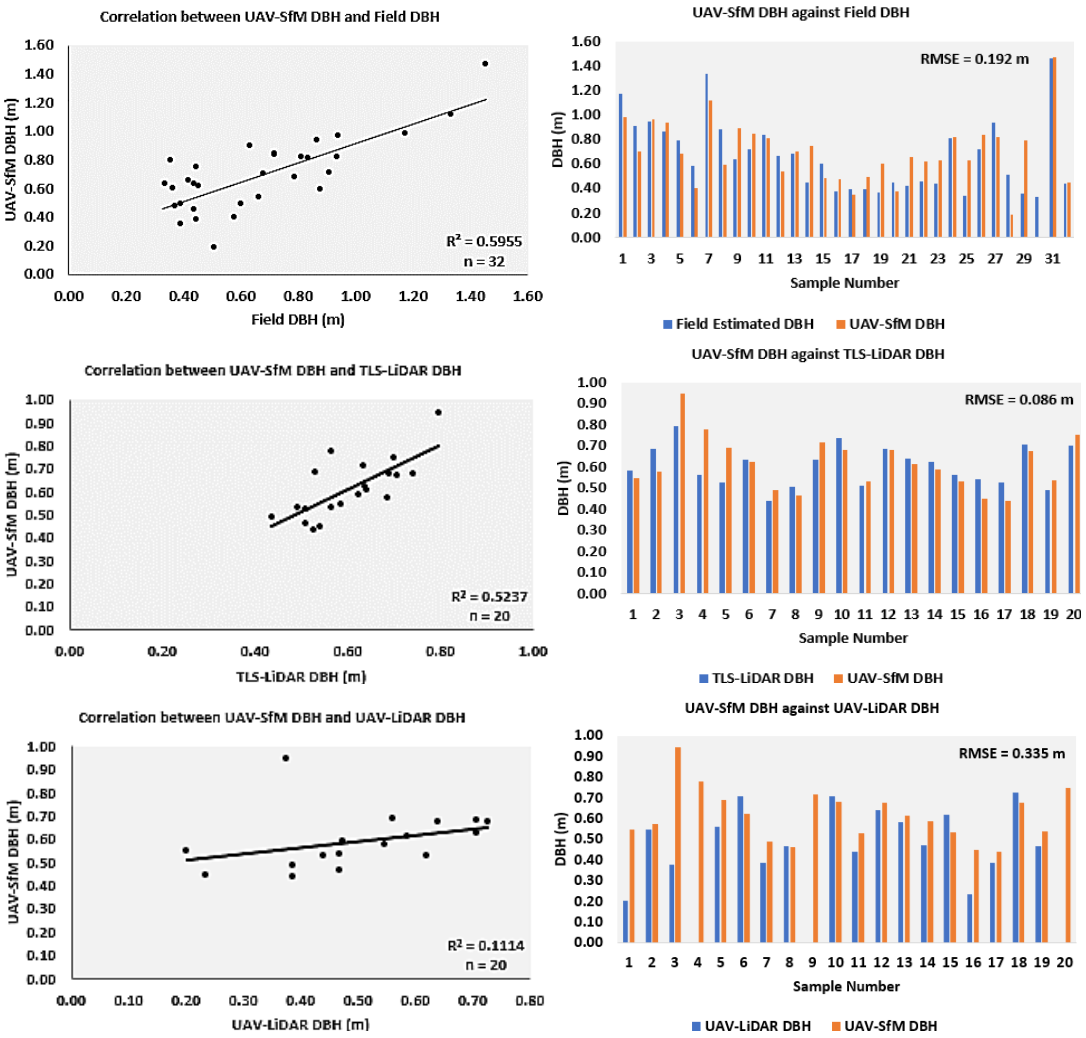

Figure 5.2 | *Comparison of UAV_{SfM} DBH to field measurement DBH, TLS_{LiDAR} and UAV_{LiDAR} DBH. Each dot represents a tree trunk DBH measurement.* ***Top row*** *– DBH comparison of UAV_{SfM} to field measured DBH at $H_{omo}FS$,* ***middle row*** *– DBH comparison of UAV_{SfM} to TLS_{LiDAR} DBH at $H_{etero}FS_1$, and* ***bottom row*** *- DBH comparison of UAV_{SfM} to UAV_{LiDAR} at $H_{etero}FS_1$.*

The poor relationship between the DBH values of the UAV_{SfM} and UAV_{LiDAR} comparison is made further apparent with the Pearson's *R* evaluation where the relationship had a value of r = 0.3337 (33.37%) signifying huge disparity between the measurements in the two datasets, compared to r = 0.7237 (72.37%) for UAV_{SfM} against TLS_{LiDAR}, and r = 0.7717 (77.17%) for UAV_{SfM} against field measurements. The RMSE for each data pair also highlighted the same indication with RMSE = 0.335 m; RMSE = 0.086 m; and RMSE = 0.192 m for UAV_{SfM} against UAV_{LiDAR}, UAV_{SfM} against TLS_{LiDAR}, and UAV_{SfM} against field measurements, respectively.

This poor relationship between UAV_{SfM} and UAV_{LiDAR} can be explained by the insufficient data acquired during the UAV survey and is evident in *Figure 5.3* below. The study area was in the outskirts of the project area for the actual original intended UAV survey done by Horts Geo-Solutions, as such, sparse LiDAR data was acquired. This meant that tree trunks were not fully captured, and as a result most measurements extracted from the tree trunk point cloud were a fraction of the actual measurement.

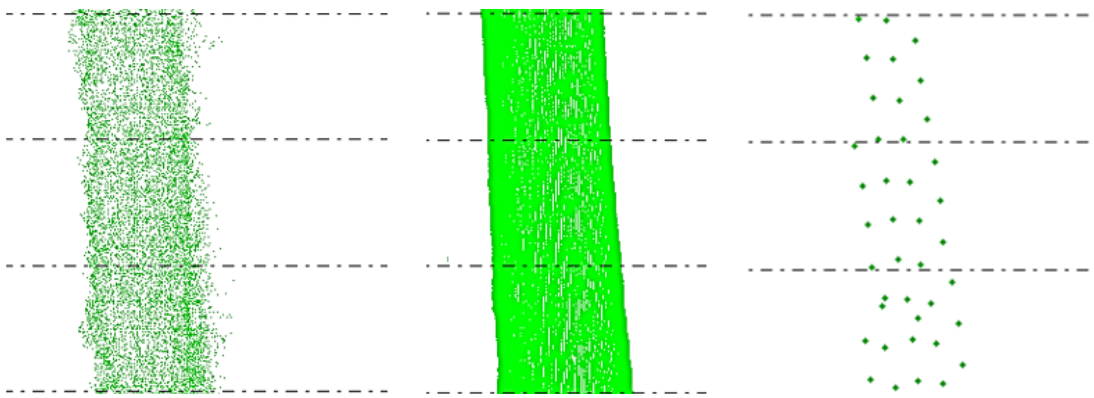

Figure 5.3 | *Comparison of UAV_{SfM} point density of a tree trunk to TLS_{LiDAR} and UAV_{LiDAR} data of the same tree trunk.* ***Left*** *– UAV_{SfM} tree trunk,* ***middle*** *– TLS_{LiDAR} tree trunk, and* ***right*** *– UAV_{LiDAR} tree trunk.*

The figure above shows the sparse LiDAR data available for the UAV_{LiDAR} dataset and highlights the results obtained that suggest a closer relationship between UAV_{SfM} and TLS_{LiDAR} data. As the point density of the UAV_{LiDAR} data is much lower, and most of the tree trunks were not fully captured during the survey, edge detection of the tree trunks was not completely successful, thereby producing structures that are not as definitive as the UAV_{SfM} and TLS_{LiDAR} counterparts, which made measurements extracted from the data inaccurate.

5.1.4 UAV_{SfM} against TLS_{LiDAR} and ALS_{LiDAR} TH

As with the DBH measurements, UAV_{SfM} TH measurements were compared to both TLS_{LiDAR} and ALS_{LiDAR} TH measurements. When assessing $H_{omo}FS$ 30 sample trees were used to evaluate the coefficient of determination between UAV_{SfM} and ALS_{LiDAR} data, where a value of R^2 = 0.9258 (92.58%) was obtained signifying an excellent correlation between the two datasets. Similarly, 20 sample trees were used in assessing the utility of UAV_{SfM} in estimating TH against TLS_{LiDAR} and ALS_{LiDAR} in $H_{etero}FS_1$. For UAV_{SfM} against TLS_{LiDAR}, a

coefficient of determination of R^2 = 0.8614 (86.14%) was achieved, signifying a great correlation between the two sets of data. A Pearson's *R* value of *r* = 0.9280 (92.80%) was also achieved, indicating a strong association between the two. However, a RMSE = 2.131 m value was achieved for this comparison which shows the average separation from the line of best fit between these two variables. On average, the UAV_{SfM} TH values were higher than the TLS_{LiDAR} values. This is suggestive of the ineffectiveness of TLS to acquire top-canopy structures in dense forest structures with closed canopies, since this is a ground-based measurement technique as opposed to UAV_{SfM} which is an aerial measurement technique.

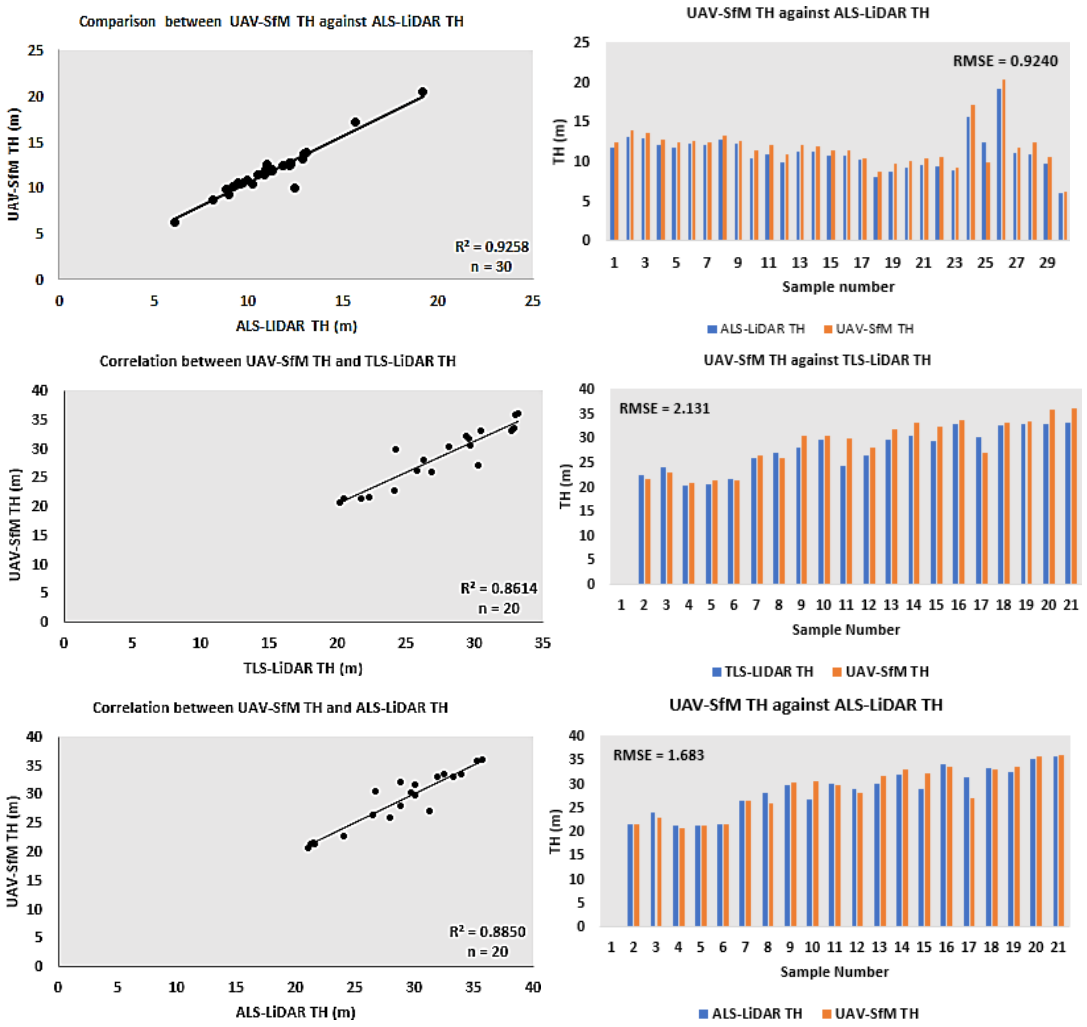

Figure 5.4 | *Scatter plot and bar chart comparison of UAV_{SfM} TH to TLS_{LiDAR} and ALS_{LiDAR} TH. Each dot represents a tree trunk DBH measurement.* ***Top row*** *– TH comparison of UAV_{SfM} to ALS_{LiDAR} at $H_{omo}FS$,* ***middle row*** *– TH comparison of UAV_{SfM} to TLS_{LiDAR} at $H_{etero}FS_1$, and* ***bottom row*** *- TH comparison of UAV_{SfM} to ALS_{LiDAR} at $H_{etero}FS_1$.*

When UAV_{SfM} was compared to ALS_{LiDAR}, a coefficient of determination of R^2 = 0.8850 (88.50%) was achieved, with a Pearson *R* value of *r* = 0.9407 (94.07%) and a RMSE = 1.683. These all indicate good correlation between the two data variables. It can be noted here that UAV_{SfM} performs slightly better when compared to ALS_{LiDAR} than when compared to TLS_{LiDAR} when considering R^2. This could be attributed to the fact that both datasets are acquired from airborne vehicles and as such are able to acquire the full top canopy. The lower RMSE value also signifies that there is lower separation from the line of best fit between the two datasets.

The larger separation between UAV_{SfM} and TLS_{LiDAR} is expected as since this is tree height that is assessed, it is logical that tree heights measured from the ground using a Terrestrial Laser Scanner would not scan the full extent of the top canopy from the ground, leaving various sections of the top canopy absent from the final compilation, and thus an unrealistic representation of the actual forest canopy. UAV_{SfM} TH, which is obtained from an aerial advantage, would succeed better at capturing the top canopy of the forest structure.

The table below displays the statistical metrics of the research endeavour, highlighting results presented in this chapter.

Table 5.1 | *Statistical metrics of the comparison of UAV_{SfM} to UAV_{LiDAR}, ALS_{LiDAR}, TLS_{LiDAR} and field measurements*

$H_{omo}FS$				$H_{etero}FS_1$							
DBH (m)		TH (m)		DBH (m)				TH (m)			
UAV_{SfM}	Field Values	UAV_{SfM}	ALS_{LiDAR}	UAV_{SfM}	TLS_{LiDAR}	UAV_{SfM}	UAV_{LiDAR}	UAV_{SfM}	TLS_{LiDAR}	UAV_{SfM}	ALS_{LiDAR}
0.985	1.175	12.437	11.762	0.548	0.583	0.548	0.201	21.577	22.327	21.577	21.491
0.705	0.912	13.89	13.072	0.576	0.685	0.576	0.546	22.819	24.106	22.819	23.981
0.964	0.940	13.659	12.897	0.945	0.794	0.945	0.376	20.746	20.186	20.746	21.058
0.933	0.866	12.728	12.113	0.778	0.562	0.778	**	21.262	20.424	21.262	21.233
0.679	0.788	12.466	11.810	0.690	0.528	0.690	0.562	21.402	21.674	21.402	21.561
0.399	0.579	12.531	12.208	0.625	0.636	0.625	0.707	26.291	25.811	26.291	26.512
1.113	1.334	12.349	12.135	0.488	0.436	0.488	0.386	25.869	26.864	25.869	27.976
0.594	0.878	13.193	12.814	0.464	0.508	0.464	0.467	30.327	28.120	30.327	29.678
0.894	0.633	12.622	12.245	0.717	0.633	0.717	**	30.488	29.676	30.488	26.695
0.841	0.719	11.406	10.464	0.681	0.739	0.681	0.706	29.802	24.189	29.802	30.061
0.809	0.837	12.036	10.887	0.529	0.509	0.529	0.441	27.968	26.305	27.968	28.823
0.537	0.664	10.877	9.882	0.678	0.687	0.678	0.639	31.630	29.618	31.630	30.002
0.699	0.680	12.011	11.271	0.613	0.640	0.613	0.585	32.970	30.408	32.970	31.893
0.749	0.446	11.899	11.226	0.588	0.624	0.588	0.473	32.187	29.403	32.187	28.767
0.487	0.602	11.482	10.767	0.532	0.562	0.532	0.619	33.615	32.855	33.615	33.932
0.475	0.375	11.424	10.816	0.448	0.539	0.448	0.235	27.031	30.264	27.031	31.295
0.348	0.393	10.345	10.189	0.439	0.526	0.439	0.387	32.976	32.665	32.976	33.220
0.490	0.391	8.642	8.077	0.677	0.705	0.677	0.726	33.409	32.761	33.409	32.523
0.603	0.365	9.770	8.787	0.537	0.492	0.537	0.467	35.791	32.953	35.791	35.209
0.378	0.446	10.081	9.162	0.750	0.699	0.750	**	36.052	33.130	36.052	35.685
0.658	0.420	10.413	9.572	***0.604**	***0.615**	**RMSE 0.3350**		**RMSE 2.1310**		**RMSE 1.6834**	
0.616	0.455	10.555	9.419	**RMSE 0.0860**		**r = 0.3334**		**r = 0.9280**		**r = 0.9407**	
0.633	0.440	9.244	8.919	**r = 0.7237**							
0.820	0.812	17.085	15.62								
0.631	0.339	9.920	12.388								
0.834	0.719	20.386	19.195								
0.815	0.938	11.794	11.091								
0.182	0.508	12.502	10.959								
0.794	0.356	10.554	9.678								
**	0.327	6.267	6.090								

1.469	1.456	**RMSE 0.9241**
0.451	0.438	**r = 0.9622**
***0.663**	***0.668**	
RMSE 0.1923		
r = 0.7717		

*Denotes the average measurement.

**Denotes a measurement that could not be extracted from the respective cloud data.

5.2 Discussion

5.2.1 Performance of UAV_{SfM} in assessing Homo- and Heterogeneous *Pinus* Forest Structures

The results obtained in this study indicate that UAV_{SfM} techniques can provide fair assessments of homogeneous and heterogeneous forest structures, with estimates being comparable to high-cost LiDAR, whether aerial or terrestrial. Several observations were made of UAV_{SfM} point cloud for assessing DBH and TH.

Firstly, in almost all instances UAV_{SfM} performed well at reconstructing ground surfaces and reproducing ground points but only where there were large enough gaps between the trees so that sufficient imagery could be captured during the nadir and oblique flights (*Figure 4.3* and *Figure 4.10*) but failed at acquiring this where trees were more closely clustered together or had closed top-canopies like in $H_{etero}FS_1$ and $H_{etero}FS_2$. Photogrammetry is only able to recreate structures within the scene that are clearly visible in multiple images acquired from multiple perspectives, unlike LiDAR that is able to penetrate the top-canopy of the forest structure and recreate the forest floor or below-canopy structures (Jayathunga, Owari and Tsuyuki, 2018). The occlusion of substantial data, such as tree trunks and the terrain in certain areas is a function of the dense forest canopy cover. This is a common digital photogrammetry limitation, often referred to as 'dead ground', caused by top-canopy structures obscuring the ground and causing omission of data.

The research results obtained on the use of UAV_{SfM} techniques in this research is further supported by other works such as González-Jaramillo, Fries and Bendix (2019) and Jayathunga, Owari and Tsuyuki (2018) that suggest that although the technique is capable of capturing vegetated terrain, such terrain must be sparsely vegetated. This is especially necessary if below-canopy variables such as DBH need to be extracted from reconstructed tree trunks. It is for this reason that this research endeavour used a combination of nadir, oblique and tessellated façade techniques to capture as much below-canopy detail from various perspectives to create concise reconstructed tree trunks, especially in dense forest structures like $H_{etero}FS_1$. To this effect, most of the tree trunks were reconstructed well and represented, structurally, the tree trunks from the front view (*Figure 4.11*). However,

because of insufficient imagery from multiple perspectives all around each tree trunk, structural failure in the reconstructed trunks occurred on the opposite side of the trunks. This affected the estimation of the circles or ellipsis generated when extracted vector data from the point cloud to assist with estimating DBH. This suggests that UAV_{SfM} techniques, in addition, face challenges in forest structures with sporadic tree growth. The tessellated façade technique could capture additional below-canopy data to recreate the tree trunks as the flight path moved parallel to the forest face. In some plantation settings, the trees are planted in rows and columns. This is an obvious advantage as a UAV could be successfully manoeuvred through the rows and columns to capture data systematically, but in forest structures with sporadic tree growth, sub-species growth, and bushes, the challenge to acquire this is much higher. Another challenge with this approach is the loss of GPS signal within the forest caused by the closed and obstructive forest canopy. This raises stability issues as the UAV is not GPS-assisted. To achieve a successful flight would require more skill in manoeuvring the UAV through the forest space using the manual flight mode. The inclusion of techniques such as terrestrial SfM used by Iglhaut et al. (2019) could also offer a solution to this challenge. This technique involves using a DSLR camera to capture images of the below-forest canopy structures from multiple perspectives to generate photogrammetric point cloud data.

Secondly, the UAV_{SfM} techniques introduced overestimations in the CHM (TH) compared to ALS_{LiDAR} for both $H_{omo}FS$ and $H_{etero}FS_1$, consistent with results obtained by Kameyama and Sugiura (2020). The RMSE for the UAV_{SfM} against ALS_{LiDAR} for $H_{omo}FS$, and UAV_{SfM} against ALS_{LiDAR} for $H_{etero}FS_1$ were 0.9240 m and 1.6834 m, respectively. A possible suggestion for the overestimation of this TH is the presence of the low-resolution ALS_{LiDAR} data used, which was unable to estimate properly each tree crown. Since UAV_{SfM} generally produced higher density point cloud from multiple perspective imagery, a richer dataset is achieved to estimate the actual TH. This is further evident in the UAV_{SfM} against TLS_{LiDAR} comparison of $H_{etero}FS_1$ where a RMSE of 2.1310 was achieved, as the TLS survey was unable to capture the exact tree crown of each tree being a terrestrial data capture technique. However, with correlations of R^2 = 0.9250 (92.50%), R^2 = 0.8850 (88.50%), and R^2 = 0.8614 (86.14%) respectively (*Figure 5.4*), it is evident that TH can be estimated with significant success using UAV_{SfM} techniques.

When assessing DBH however, UAV_{SfM} performs with adequate success. In this study, it was discovered that a poor correlation existed between UAV_{SfM} and UAV_{LiDAR} with R^2 = 0.1114 (11.14%) and a RMSE of 0.3350 (*Figure 4.19*). This is inconsistent with previous studies but can be explained by the low resolution UAV_{LiDAR} data available for this study which failed to capture enough LiDAR data, below- or above-canopy, to successfully extract accurate measurements. In contrast, UAV_{SfM} performed relatively well against field measurements in $H_{omo}FS$, and against TLS_{LiDAR} in $H_{etero}FS_1$ with R^2 = 0.5955 (59.55%) and R^2 = 0.5237 (52.37%), respectively (*Figure 5.2*). The best fit was achieved between UAV_{SfM} against TLS_{LiDAR} with RMSE = 0.086 signifying that the measurements extracted from the UAV_{SfM} data were closely similar to their TLS_{LiDAR} counterparts within ±0.011 m. UAV_{SfM} against field measurements also had a RMSE of 0.192 suggesting a low disparity between the two variables.

The results obtained in this study suggest that UAV_{SfM} techniques perform significantly well in estimating TH in both homogeneous and heterogeneous forest structures, but only moderately well at estimating DBH in both forest structures. The results demonstrated that UAV_{SfM} can yield estimations comparable to LiDAR data, and suggest the potential use of the technology in forest inventory acquisition and prediction, which is consistent to previous studies in the field.

CHAPTER 6

6.1 Conclusion

The study intended to evaluate the efficacy of using multi-rotor UAVs in acquiring and assessing two allometric variables necessary for rudimentary biomass estimation of forests, in this case, homogeneous and heterogenous *Pinus* forest structures. To achieve this, three objectives were identified as the guiding narrative to collect, assess, manipulate, investigate, and present the data and findings. Firstly, to investigate what necessary data, standards, and ideal conditions are necessary to carry out measurement and feature extraction of forest features and structures using a multi-rotor UAV and SfM Photogrammetry. Secondly, to use existing and collected data to compare labour intensity, spatial resolution, and spatial accuracy of more accurate technologies such as ALS_{LiDAR} and TLS_{LiDAR} to UAV_{SfM} within the study areas and validate these UAV_{SfM} derived feature measurement results. Finally, to conclude and make recommendations on the efficiency of capturing homogeneous and heterogenous *Pinus* forest structures in South Africa using multi-rotor UAV_{SfM} Photogrammetry in support of bridging technological gaps for the REDD+ programme in the country.

Creating dense UAV_{SfM} derived photogrammetric point cloud adequate to extract allometric features of homogenous and heterogenous *Pinus* forest structures requires high resolution imagery acquired from multiple perspectives and with high image overlap. In this research, not only were 1 cm/px to 3 cm/px nadir and oblique imagery acquired from multiple flight heights above and around the forest structures, but high-resolution tessellated façade imagery was also acquired of the forest face to provide additional perspectives. All images were acquired using a relatively cheap commercially available UAV. In addition to that, some rudimentary GCPs were utilised to assist with image alignment and optimisation, as well as a capable SfM software. Though there is no industry standard for producing UAV_{SfM} point cloud the workflow followed in this research endeavour, elaborated on in Chapter 4, mirrors that followed by previous studies. Optimal weather conditions for UAV flight include a cloudless or minimally clouded sky to minimise image quality in terms of brightness, wind speeds below 15 km/h to minimise camera motion blur and faster battery depletion. Flying at midday or high noon can reduce the presence of shadows that may affect image alignment that can translate into a noisy point cloud.

Compared to acquiring TLS_{LiDAR} capturing UAV_{SfM} data was a less tedious task as there is no need to traverse through forests and create multiple setups to scan trees. Capturing all the UAV imagery for all three study areas took a grand total of 182 minutes (3 hours 20 minutes), while capturing the TLS_{LiDAR} for a section of $H_{etero}FS_1$ alone took 65 minutes (1 hour 5 minutes) across 13 setups, while traversing through difficult forested terrain. Processing the UAV data was also less tedious as most of it was automated once the right parameters were included and the right processing phases scheduled. The only real human input aside from adding the images into the software was placing the GCPs in their right positions. With the TLS_{LiDAR} a fair bit of manual registration was required to register the various scans and finally unify them into one composite scan. When spatial resolution and spatial accuracy is considered, although the UAV_{SfM} data is limited to centimetre accuracy it faired rather well compared to its TLS_{LiDAR} and ALS_{LiDAR} data counterparts as the results demonstrate.

To conclude, the research findings suggest that although inherent of some technological shortcomings, such as battery life and sensor limitations, UAV_{SfM} point cloud derived from a multi-rotor UAV has a place in forest management systems, forest inventory acquisition, and subsequently biomass estimation. Compared to LiDAR, UAV_{SfM} should not be seen as a replacement but rather as a viable supplement or cheaper alternative depending on the scale or cost of the project initiative, even perhaps as a sampling technique.

6.2 Recommendation

The strength of an adequate dense UAV_{SfM} point cloud lies in the inclusion of multiple images from various perspectives. Though the various dense cloud produced in this research endeavour provided suitable results, more images are recommended. In particular, oblique imagery of the forest structure where the structure occupies most of the frame with very little inclusion of the sky or distant features. Further study should be done to investigate the quality of the point cloud obtained from this.

Tessellated façade imagery contributed to the quality of reconstructing the below-canopy forest structures. Further study should be done on utilising this imagery exclusively in reproducing forest structures, or inclusively with nadir and oblique imagery to ascertain its role as a viable flight pattern in UAV_{SfM} forestry management.

REFERENCES

Aber, J.W. and Babb, T.A., 2018. The Challenges of Processing Kite Aerial Photography Imagery with Modern Photogrammetry Techniques. *International Journal of Aviation, Aeronautics, and Aerospace*, 5(2), pp.3–24.

Afif-Khouri, E., Camara-Obregon, A., Canga, E. and Dieguez-Aranda, I., 2013. Above-ground biomass equations for Pinus radiata D . Don. *Forest Systems*, 22(3), pp.408–415.

Agisoft, 2015. *Photoscan Professional, v 1.1*.

Agisoft, 2017. Agisoft PhotoScan User Manual. (Professional Edition).

Agriculture, F. and C.D., 2006. *Measurement of Diameter at Breast Height (DBH)*. *Nature Conservation Practice Note*, .

AgriOptics, 2019. *GreenSeeker*. California.

Arp, H., Griesbach, J.C. and Burns, J., 1982. Mapping in Tropical Forests: A New Approach Using the Laser Airborne Profile Recorder. *Photogrammetric Engineering and Remote Sensing*, 48, pp.91–100.

Bagaram, M.B., Giuliarelli, D., Chirici, G., Giannetti, F. and Barbati, A., 2018. UAV remote sensing for biodiversity monitoring: Are forest canopy gaps good covariates? *Remote Sensing*, 10(9), pp.1–28.

Bao, Y., Gao, W. and Gao, Z., 2009. Estimation of winter wheat biomass based on remote sensing data at various spatial and spectral resolutions. *Frontiers of Earth Science in China*, 3(1), pp.118–128.

Blue Marble Geographics, 2017a. *Create Elevation Grid from 3D Vector Data*. [online] Available at: <https://www.bluemarblegeo.com/knowledgebase/global-mapper-19/Create_Elevation_Grid_from_3D_Vector_Data.htm#Binning_an_Elevation_Grid> [Accessed 15 Dec. 2020].

Blue Marble Geographics, 2017b. *Lidar Automatic Non-Ground Classification*. [online] Available at: <https://www.bluemarblegeo.com/knowledgebase/global-mapper-19/Lidar_Module/nonground_classification.htm> [Accessed 14 Dec. 2020].

Bognot, J.R., Candido, C.G., Blanco, A.C., Rene, J. and Montelibano, Y., 2018. BUILDING CONSTRUCTION PROGRESS MONITORING USING UNMANNED AERIAL SYSTEM (UAS), LOW-

COST PHOTOGRAMMETRY, AND GEOGRAPHIC INFORMATION SYSTEM (GIS).

Brede, B., Lau, A., Bartholomeus, H.M. and Kooistra, L., 2017. Comparing RIEGL RiCOPTER UAV LiDAR derived canopy height and DBH with terrestrial LiDAR. *Sensors (Switzerland)*, 17(10), pp.1–17.

Carlson, T.N. and Riziley, D.A., 1997. On the Relation between NDVI, Fractional Vegetation Cover, and Leaf Area Index. *Remote Sensing Environ*, 62(2), pp.241–252.

Carnevali, L., Ippoliti, E., Lanfranchi, F., Menconero, S., Russo, M. and Russo, V., 2018. Close-range MINI-UAVS photogrammetry for architecture survey. *International Archives of the Photogrammetry, Remote Sensing and Spatial Information Sciences - ISPRS Archives*, 42(2), pp.217–224.

CCRS/CCT, 2016a. *Tutorial: Fundamentals of Remote Sensing (Online)*. CCRS, Canadian Centre for Remote Sensing.

CCRS/CCT, 2016b. *Tutorial: Fundamentals of Remote Sensing (Online)*. [online] CCRS, Canadian Centre for Remote Sensing. Available at: <http://www.nrcan.gc.ca/earth-sciences/geomatics/satellite-imagery-air-photos/satellite-imageryproducts/educational-resources/9309>.

Chisholm, R.A., Cui, J., Lum, S.K.Y. and Chen, B.M., 2013. UAV LiDAR for below-canopy forest surveys. *Journal of Unmanned Vehicle Systems*, 01(01), pp.61–68.

Colomina, I. and Molina, P., 2014. Unmanned aerial systems for photogrammetry and remote sensing: A review. *ISPRS Journal of Photogrammetry and Remote Sensing*, 92, pp.79–97.

Dandois, J.P., Olano, M. and Ellis, E.C., 2015. Optimal altitude, overlap, and weather conditions for computer vision uav estimates of forest structure. *Remote Sensing*, 7(10), pp.13895–13920.

DEA, 2014. *Greenhouse gas inventory for South Africa 2000 - 2010*. *South Africa Government*, .

Díaz-Varela, R.A., de la Rosa, R., León, L. and Zarco-Tejada, P.J., 2015. High-resolution airborne UAV imagery to assess olive tree crown parameters using 3D photo reconstruction: Application in breeding trials. *Remote Sensing*, 7(4), pp.4213–4232.

DJI, 2017a. DJI Phantom 3 Professional User Manual.

DJI, 2017b. DJI Phantom 4 Professional User Manual.

DJI, 2020. *DJI Matrice 600 Pro - DJI*. [online] Available at: <https://www.dji.com/matrice600-pro?site=brandsite&from=nav> [Accessed 8 May 2020].

Domingo, D., Ørka, H.O., Næsset, E., Kachamba, D. and Gobakken, T., 2019. Effects of UAV image resolution, camera type, and image overlap on accuracy of biomass predictions in a tropicalwoodland. *Remote Sensing*, 11(8).

Dovey, S.B., 2014. *Current carbon stock estimation capability for South African commercial forest plantations*. Pietermaritzburg.

Eisenbeiss, H., 2009. *UAV photogrammetry*. Zürich: ETH Zürich.

ESA, 2019a. *Spatial Resolution*. [online] Available at: <https://sentinel.esa.int/web/sentinel/user-guides/sentinel-2-msi/resolutions/spatial> [Accessed 28 Oct. 2019].

ESA, 2019b. *Spatial Resolution*.

FAO, 2016. *Global Forest Resources Assessment 2015*. *FAO Forestry*.

FAO FRA, 2012. Forest Resources Assessment 2015: Terms and Definitions. *FAO report*, p.36.

Fraser, B.T. and Congalton, R.G., 2018. Issues in Unmanned Aerial Systems (UAS) data collection of complex forest environments. *Remote Sensing*, 10(6).

Galidaki, G., Zianis, D., Gitas, I., Radoglou, K., Karathanassi, V., Tsakiri–Strati, M., Woodhouse, I. and Mallinis, G., 2017. Vegetation biomass estimation with remote sensing: focus on forest and other wooded land over the Mediterranean ecosystem. *International Journal of Remote Sensing*, 38(7), pp.1940–1966.

García, M., Riaño, D., Chuvieco, E. and Danson, F.M., 2010. Estimating biomass carbon stocks for a Mediterranean forest in central Spain using LiDAR height and intensity data. *Remote Sensing of Environment*, 114(4), pp.816–830.

GISGeography, 2019. *Landsat Program: Satellite Imagery Data and Bands*. [online] Available at: <https://gisgeography.com/landsat-program-satellite-imagery-bands/> [Accessed 24 Oct. 2019].

González-Jaramillo, V., Fries, A. and Bendix, J., 2019. AGB estimation in a tropical mountain forest (TMF) by means of RGB and multispectral images using an unmanned aerial vehicle (UAV). *Remote Sensing*, 11(12), pp.1–22.

Gonzalez, P., Asner, G.P., Battles, J.J., Lefsky, M.A., Waring, K.M. and Palace, M., 2010. Forest carbon densities and uncertainties from Lidar, QuickBird, and field measurements in California. *Remote Sensing of Environment*, 114(7), pp.1561–1575.

Guerra-Hernández, J., González-Ferreiro, E., Sarmento, A., Silva, J., Nunes, A., Correia, A.C., Fontes, L., Tomé, M. and Díaz-Varela, R., 2016. Using high resolution UAV imagery to estimate tree variables in Pinus pinea plantation in Portugal. *Forest Systems*, 25(2), pp.1–5.

Günlü, A., Ercanli, I., Başkent, E.Z. and Çakır, G., 2014. Estimating aboveground biomass using Landsat TM imagery: A case study of Anatolian Crimean pine forests in Turkey. *Annals of Forest Research*, 57(2), pp.289–298.

Iglhaut, J., Cabo, C., Puliti, S., Piermattei, L., O'Connor, J. and Rosette, J., 2019. Structure from Motion Photogrammetry in Forestry: a Review. *Current Forestry Reports*, 5(3), pp.155–168.

Iizuka, K., Yonehara, T., Itoh, M. and Kosugi, Y., 2018. Estimating Tree Height and Diameter at Breast Height (DBH) from Digital surface models and orthophotos obtained with an unmanned aerial system for a Japanese Cypress (Chamaecyparis obtusa) Forest. *Remote Sensing*, 10(1), pp.1–14.

IPCC, 2006. *Intergovernmental Panel on Climate, Guidelines for National Greenhouse Gas Inventories, Prepared by the National Greenhouse Gas Inventories Programme*.

IRENA, 2016. World Energy Resources: Bioenergy 2016. *World Energy Council*, p.60.

Jayathunga, S., Owari, T. and Tsuyuki, S., 2018. Evaluating the performance of photogrammetric products using fixed-wing UAV imagery over a mixed conifer-broadleaf forest: Comparison with airborne laser scanning. *Remote Sensing*, 10(2), pp.1–24.

Jones, C.L., Weckler, P.R., Maness, N.O., Jayasekara, R., Stone, M.L. and Chrz, D., 2007. Remote Sensing To Estimate Chlorophyll Concentration In Spinach Using Multi-Spectral Plant Reflectance. *American Society of Agricultural and Biological Engineers*, 50(6), pp.2267–2273.

Kachamba, D.J., Eid, T. and Gobakken, T., 2016. Above- and belowground biomass models for trees in the miombo woodlands of Malawi. *Forests*, 7(2).

Kachamba, D.J., Ørka, H.O., Gobakken, T., Eid, T. and Mwase, W., 2016. Biomass estimation using 3D data from unmanned aerial vehicle imagery in a tropical woodland. *Remote Sensing*, 8(11), pp.1–18.

Kameyama, S. and Sugiura, K., 2020. Estimating tree height and volume using unmanned aerial vehicle photography and sfm technology, with verification of result accuracy. *Drones*, 4(2), pp.1–21.

Kumar, Garg, Govil and Kushwaha, 2019. PolSAR-Decomposition-Based Extended Water Cloud Modeling for Forest Aboveground Biomass Estimation. *Remote Sensing*, 11(19), p.2287.

Kumar, L. and Mutanga, O., 2017. Remote Sensing of Above-Ground Biomass. *Remote Sensing*, 9(9), p.935.

Lachat, E., Landes, T. and Grussenmeyer, P., 2018. COMPARISON OF POINT CLOUD REGISTRATION ALGORITHMS FOR BETTER RESULT ASSESSMENT-TOWARDS AN OPEN-SOURCE SOLUTION.

Lamprecht, S., Stoffels, J., Dotzler, S., Haß, E. and Udelhoven, T., 2015. aTrunk-an ALS-based trunk detection algorithm. *Remote Sensing*, 7(8), pp.9975–9997.

Landsberg, J.J., Waring, R.H. and Coops, N.C., 2003. Performance of the forest productivity model 3-PG applied to a wide range of forest types. *Forest Ecology and Management*, 172(2–3), pp.199–214.

Lehtonen, A., Mäkipää, R., Heikkinen, J., Sievänen, R. and Liski, J., 2004. Biomass expansion factors (BEFs) for Scots pine, Norway spruce and birch according to stand age for boreal forests. *Forest Ecology and Management*, 188(1–3), pp.211–224.

Lenovo, 2020. *Lenovo Y70 Touch | 17.3" Affordable Mobile Laptop | Lenovo US*. [online] Available at: <https://www.lenovo.com/us/en/laptops/lenovo/y-series/y70-touch/> [Accessed 13 Jun. 2020].

Lim, K., Treitz, P., Wulder, M., St-Onge, B. and Flood, M., 2003. LiDAR remote sensing of forest structure. *Progress in Physical Geography*, 27(1), pp.88–106.

Lisein, J., Pierrot-Deseilligny, M., Bonnet, S. and Lejeune, P., 2013. A Photogrammetric Workflow for the Creation of a Forest Canopy Height Model from Small Unmanned Aerial System Imagery. *Forests*, 4(4), pp.922–944.

Maack, J., Kattenborn, T., Fassnacht, F.E. and Enssle, F., 2015. Modeling forest biomass using Very-High-Resolution data - Combining textural , spectral and photogrammetric predictors derived from spaceborne stereo images. *European Journal of Remote Sensing*, 48(April), pp.245–261.

Maina, E.W., Odera, P.A. and Kinyanjui, M.J., 2017. Estimation of Above Ground Biomass in Forests Using Alos Palsar Data in Kericho and Aberdare Ranges. *Open Journal of Forestry*, 07(02), pp.79–96.

Makhado, R. a., Saidi, A.T., Mantlana, B.K. and Mwayafu, M.D., 2011. Challenges of reducing emissions from deforestation and forest degradation (REDD+) on the African continent. *South African Journal of Science*, 107, pp.7–9.

Malone, T., Liang, J. and Packee, E., 2009. *Agriculture Cooperative Alaska Forest Inventory*.

Meintjes, E.M., Douglas, T.S., Martinez, F., Vaughan, C.L., Adams, L.P., Stekhoven, A. and Viljoen, D., 2002. A stereo-photogrammetric method to measure the facial dysmorphology of children in the diagnosis of fetal alcohol syndrome. *Medical Engineering & Physics*, 24(10), pp.683–689.

Meng, S., Pang, Y., Zhang, Z., Jia, W. and Li, Z., 2016. Mapping aboveground biomass using texture indices from aerial photos in a temperate forest of Northeastern China. *Remote Sensing*, 8(3).

Mesas-Carrascosa, F.J., Torres-Sánchez, J., Clavero-Rumbao, I., García-Ferrer, A., Peña, J.M., Borra-Serrano, I. and López-Granados, F., 2015. Assessing optimal flight parameters for generating accurate multispectral orthomosaicks by uav to support site-specific crop management. *Remote Sensing*, 7(10), pp.12793–12814.

Mikhail, E.M., Bethel, J.S. and McGlone, J.C., 2001. *Introduction to modern photogrammetry*. Volume 1 ed. New Yord: John Wiley & Sons, Inc.

Mlambo, R., Woodhouse, I.H., Gerard, F. and Anderson, K., 2017. Structure from motion (SfM) photogrammetry with drone data: A low cost method for monitoring greenhouse gas emissions from forests in developing countries. *Forests*, 8(3), pp.1–20.

Mohan, M., Silva, C.A., Klauberg, C., Jat, P., Catts, G., Cardil, A., Hudak, A.T. and Dia, M., 2017. Individual tree detection from unmanned aerial vehicle (UAV) derived canopy height model in an open canopy mixed conifer forest. *Forests*, 8(9), pp.1–17.

Montealegre, A.L., Lamelas, M.T., de la Riva, J., García-Martín, A. and Escribano, F., 2016. Use of low point density ALS data to estimate stand-level structural variables in Mediterranean Aleppo pine forest. *Forestry*, 89(4), pp.373–382.

Moore, J.R., 2010. Allometric equations to predict the total above-ground biomass of radiata pine trees. *Annals of Forest Science*, 67(8), pp.806–806.

Naesset, E., 2002. Determination of Mean Tree Height of Forest Stands by Digital Photogrammetry. *Scandinavian Journal of Forest Research*, 17(5), pp.446–459.

Nagai, M., Shibasaki, R., Manandhar, D. and Zhao, H., 2004. *DEVELOPMENT OF DIGITAL SURFACE MODEL AND FEATURE EXTRACTION BY INTEGRATING LASER SCANNER AND CCD SENSOR WITH IMU TS SS-3: Mobile Multi-Sensor Mapping Systems*.

National Forestry Act 84.

NEED, 2006. Biomass at a glance. *National Energy Education Development*.

Olofsson, K. and Holmgren, J., 2017. Tree stem and canopy biomass estimates from terrestrial laser scanning data. In: *International Archives of the Photogrammetry, Remote Sensing and Spatial Information Sciences - ISPRS Archives*. International Society for Photogrammetry and Remote Sensing, pp.157–160.

Pang, Y., Li, Z., Ju, H., Lu, H., Jia, W., Si, L., Guo, Y., Liu, Q., Li, S., Liu, L., Xie, B., Tan, B. and Dian, Y., 2016. LiCHy: The CAF's LiDAR, CCD and hyperspectral integrated airborne observation system. *Remote Sensing*, 8(5), pp.1–16.

Parresol, B.R., 1999. Assessing tree and stand biomass: A review with examples and critical comparisons. *Forest Science*, 45(4), pp.573–593.

Pix4Dcapture, 2019a. *Pix4Dcapture - Getting Started – Support*. [online] Available at: <https://support.pix4d.com/hc/en-us/articles/202557269-Pix4Dcapture-Getting-Started> [Accessed 13 Sep. 2019].

Pix4Dcapture, 2019b. *Pix4Dcapture - Getting Started – Support*. [online] Available at: <https://www.pix4d.com/product/pix4dcapture>.

Pommerening, A., 2007. *Basic tree variables , forestry summary characteristics and biodiversity measures*.

Puliti, S., 2017. Use of photogrammetric 3D data for forest inventory Bruk av 3D-data fra fotogrammetri for skogtaksering Philosophiae Doctor (PhD) Thesis Norwegian University of Life Sciences. (November).

Puliti, S., Gobakken, T., Ørka, H.O. and Næsset, E., 2017. Assessing 3D point clouds from aerial photographs for species-specific forest inventories. *Scandinavian Journal of Forest Research*, 32(1), pp.68–79.

Puliti, S., Ørka, H.O., Gobakken, T. and Næsset, E., 2015. Inventory of small forest areas using an unmanned aerial system. *Remote Sensing*, 7(8), pp.9632–9654.

Rahlao, S., Mantlana, B., Winkler, H. and Knowles, T., 2012. South Africa's national REDD+ initiative: Assessing the potential of the forestry sector on climate change mitigation. *Environmental Science and Policy*, 17, pp.24–32.

Ratnasingam, J.., Ng'Andwe, P.., Ioras, F.. and Abrudan, I.V.., 2014. Forestry and Forest Products Industries in Zambia and the Role of REDD+ Initiatives. *International Forestry Review*, 16(4), pp.474–484.

Richards J.A., 1993. Fourier Transformation of Image Data. In: *Fourier Transformation of Image Data. In: Remote Sensing Digital Image Analysis*. Berlin, Heidelberg: Springer, Berlin, Heidelberg, p.pp 155-179.

Riegl, 2020. *RIEGL - RIEGL Laser Measurement Systems*. [online] Available at: <http://www.riegl.com/> [Accessed 7 Apr. 2020].

Roy, P.S. and Ravan, S.A., 1996. Biomass estimation using satellite remote sensing data - An investigation on possible approaches for natural forest. *Journal of Biosciences*, 21(4), pp.535–561.

SANBI, 2019. *South African National Parks - SANParks - Official Website - Accommodation, Activities, Prices, Reservations*. [online] Available at: <https://www.sanparks.org/misc/terms/> [Accessed 19 Feb. 2019].

Schenk, T., 2005. *Introduction to Photogrammetry*. Ohio.

Sensefly Ltd, 2014. Ebee Sensefly: Extended User Manual. (September), p.166.

Simonson, W., Ruiz-Benito, P., Valladares, F. and Coomes, D., 2016b. Modelling above-ground carbon dynamics using multi-temporal airborne lidar: insights from a Mediterranean woodland. *Biogeosciences*, 13(4), pp.961–973.

Skarlatos, D. and Kiparissi, S., 2012. COMPARISON of LASER SCANNING, PHOTOGRAMMETRY and SFM-MVS PIPELINE APPLIED in STRUCTURES and ARTIFICIAL SURFACES. *ISPRS Annals of the Photogrammetry, Remote Sensing and Spatial Information Sciences*, 1(September), pp.299–304.

St-Onge, B., Vega, C., Fournier, R.A., Hu, Y., Vega{, C. and Hu{, Y., 2008. Mapping canopy height using a combination of digital stereo-photogrammetry and lidar. *nternational Journal of Remote Sensing*, 29(11), pp.3343–3364.

Tagoe, N.D., Rüther, H. and Smit, J., 2016. *Developing an accurate close-range photogrammetric technique for extracting 3D information from spherical panoramic*

images. University of Cape Town.

Tanhuanpää, T., Saarinen, N., Kankare, V., Nurminen, K., Vastaranta, M., Honkavaara, E., Karjalainen, M., Yu, X., Holopainen, M. and Hyyppä, J., 2017. Accuracy of high-altitude photogrammetric point clouds in mapping. In: *Lecture Notes in Geoinformation and Cartography*. Springer Berlin Heidelberg, pp.167–181.

Ter-Mikaelian, M.T. and Korzukhin, M.D., 1997. Biomass equations for sixty-five North American tree species. *Forest Ecology and Management*, 97(1), pp.1–24.

Theodoridou, S., Tokmakidis, K. and Scarlatos, D., 2000. USE OF RADIO-CONTROLLED MODEL HELICOPTERS IN ARCHAEOLOGY SURVEYING AND IN BUILDING CONSTRUCTION INDUSTRY. *International Archives of Photogrammetry and Remote Sensing*, Volume 33, pp.825–829.

Theron, J.M., Van Laar, A., Kunneke, A. and Bredenkamp, B. V., 2004. A preliminary assessment of utilizable biomass in invading Acacia stands on the Cape coastal plains. *South African Journal of Science*, 100(1–2), pp.123–125.

Tongwane, M., Mdlambuzi, T., Moeletsi, M., Tsubo, M., Mliswa, V. and Grootboom, L., 2016. Greenhouse gas emissions from different crop production and management practices in South Africa. *Environmental Development*, 19(June), pp.23–35.

Topodrone, 2021. *Correction of the rolling shutter distortion and processing survey data from Topodrone DJI Mavic 2 Pro L1/L2 RTK/PPK*. [online] Available at: <https://topodrone.org/news/article/rolling-shutter-distortion-correction/> [Accessed 7 Jul. 2021].

Tuswa, N., Bugan, R.D.H., Mapeto, T., Jovanovic, N., Gush, M., Kapangaziwiri, E., Dzikiti, S., Kanyerere, T. and Xu, Y., 2019. The impacts of commercial plantation forests on groundwater recharge: A case study from George (Western Cape, South Africa). *Physics and Chemistry of the Earth*, 112(December), pp.187–199.

Wallace, L., Lucieer, A., Malenovskỳ, Z., Turner, D. and Vopěnka, P., 2016. Assessment of forest structure using two UAV techniques: A comparison of airborne laser scanning and structure from motion (SfM) point clouds. *Forests*, 7(3).

Wang, J., Zongjian, L. and Li, C., 2004. *RECONSTRUCTION OF BUILDINGS FROM A SINGLE UAV IMAGE*.

Wester-Ebbinghaus, W. and Przybilla, H.J., 1979. Aerial photos by means of radio-

controlled aircraft. *Bildmessung und Luftbildwesen*, Volume 47(Issue 5), pp.137–142.

Wester-Ebbinghaus, W., 1980. Aerial photography by radio controlled model helicopter. *The Photogrammetric Record*, 10, pp.85–92.

Yurtseven, H., Akgül, M. and Gülci, S., 2017. MODELLING SINGLE TREE STRUCTURE WITH TERRESTRIAL LASER SCANNER.

Zianis, D., Muukkonen, P., Mäkipää, R. and Mencuccini, M., 2005. *Biomass and stem volume equations for tree species in Europe*. *Silva Fennica Monographs*, .

Zischinsky, T., Dorffner, L. and Rottensteiner, F., 2000. Application of a New Model Helicopter System in Arquitectural Photogrammetry. *International Archives of Photogrammetry. Remote Sensing and Spatial Information Sciences*, 33(January 2000), pp.177–183.

Zoller + Fröhlich, 2020. *ZF-Laser - Z+F IMAGER® 5010X, 3D Laser Scanner*. [online] Available at: <https://www.zf-laser.com/Z-F-IMAGER-R-5010X.3d_laser_scanner.0.html?&L=1> [Accessed 9 Apr. 2020].

Zoller + Fröhlich, 2020. *ZF-Laser - Z+F LaserControl®*. [online] Available at: <https://www.zf-laser.com/Z-F-LaserControl-R.laserscanner_software_1.0.html?&L=1> [Accessed 20 Nov. 2020].

APPENDIX A – HomoFS Agisoft Processing Report

30 July 2018

Survey Data

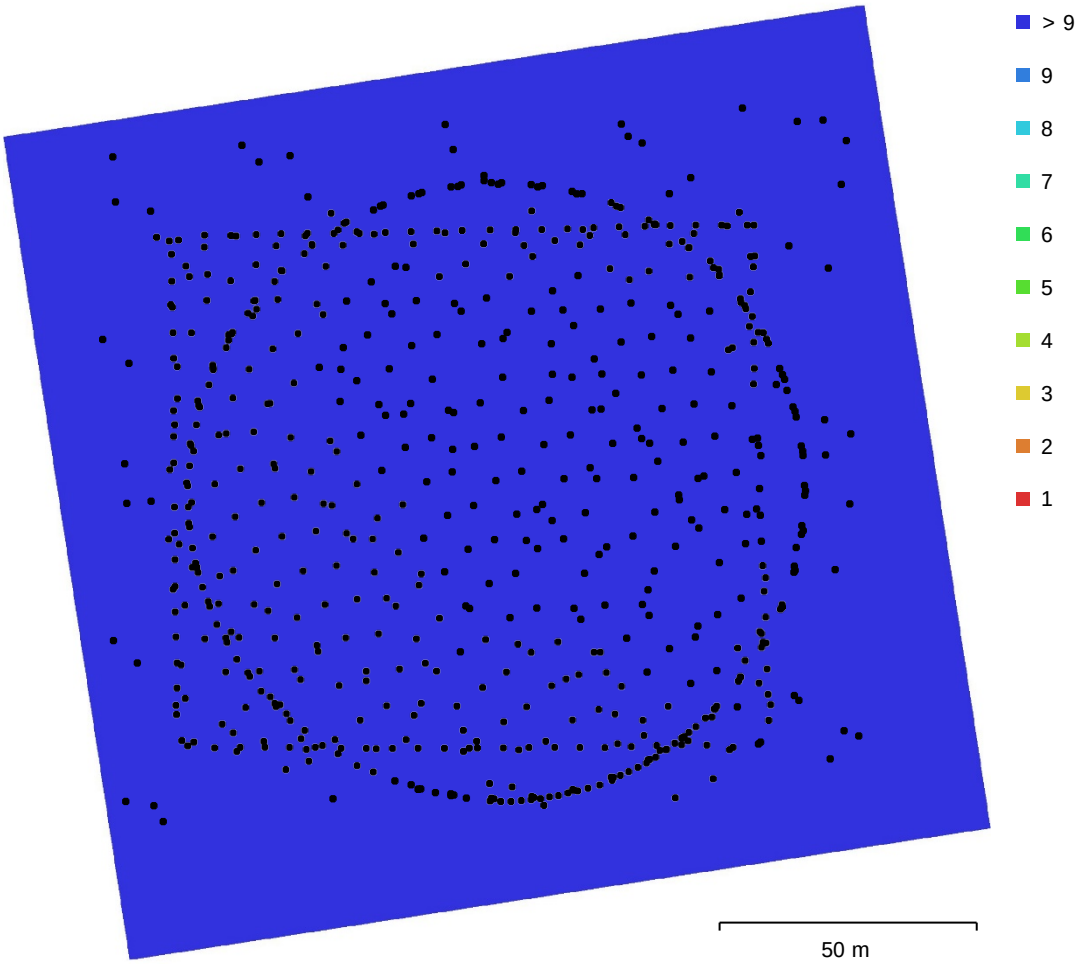

Fig. 1. Camera locations and image overlap.

Number of images:	647	Camera stations:	647
Flying altitude:	42 m	Tie points:	74,312
Ground resolution:	1.09 cm/pix	Projections:	460,299
Coverage area:	0.0274 km²	Reprojection error:	2.02 pix

Camera Model	Resolution	Focal Length	Pixel Size	Precalibrated
FC6310 (8.8mm)	4864 x 3648	8.8 mm	2.61 x 2.61 µm	No
FC6310 (8.8mm)	5472 x 3648	8.8 mm	2.41 x 2.41 µm	No

Table 1. Cameras.

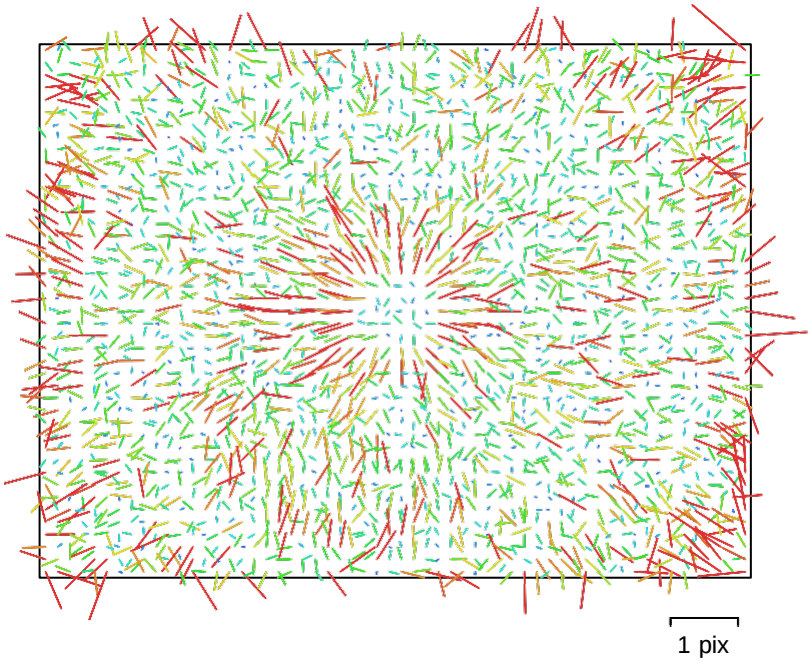

Fig. 2. Image residuals for FC6310 (8.8mm).

FC6310 (8.8mm)

484 images

Type	Resolution	Focal Length	Pixel Size
Frame	**4864 x 3648**	**8.8 mm**	**2.61 x 2.61 µm**

	Value	Error	F	Cx	Cy	B1	B2	K1	P1	P2
F	**3673.33**	0.11	1.00	0.08	-0.40	-0.39	-0.12	-0.07	-0.07	-0.09
Cx	**13.0699**	0.071		1.00	-0.01	0.05	0.14	0.01	0.75	-0.00
Cy	**15.8724**	0.066			1.00	-0.01	0.02	-0.11	-0.02	0.57
B1	**-0.857576**	0.024				1.00	-0.05	-0.08	0.06	0.03
B2	**1.47165**	0.024					1.00	-0.08	-0.03	0.04
K1	**-0.00144747**	1.7e-005						1.00	-0.01	-0.11
P1	**0.0013152**	6.1e-006							1.00	-0.01
P2	**0.000132769**	4.8e-006								1.00

Table 2. Calibration coefficients and correlation matrix.

Camera Calibration

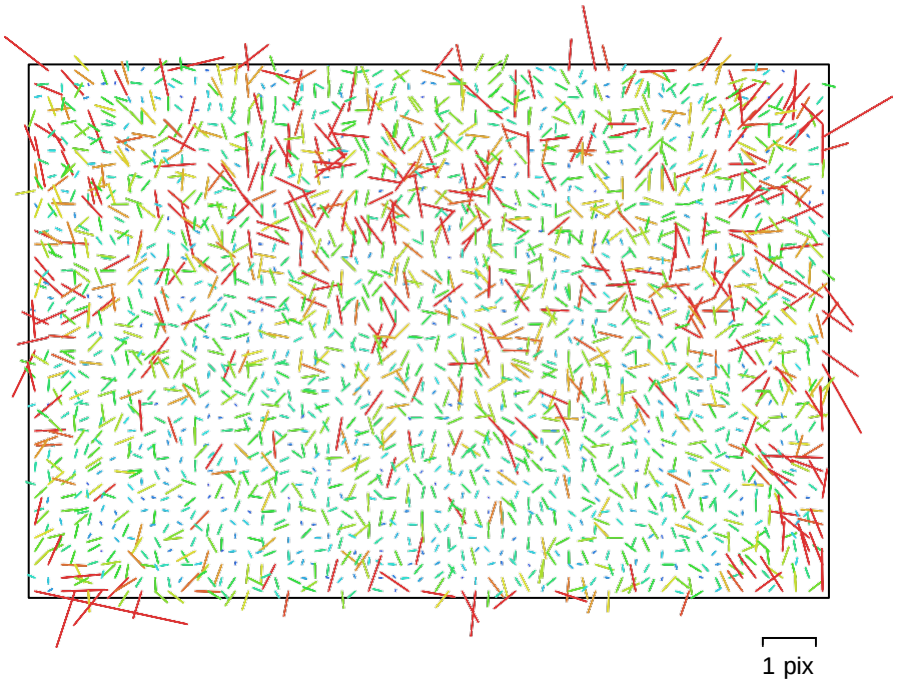

Fig. 3. Image residuals for FC6310 (8.8mm).

FC6310 (8.8mm)

163 images

Type	Resolution	Focal Length	Pixel Size
Frame	**5472 x 3648**	**8.8 mm**	**2.41 x 2.41 µm**

	Value	Error	F	Cx	Cy	B1	B2	K1	P1	P2
F	**3670.86**	0.22	1.00	-0.03	-0.34	-0.61	-0.08	-0.07	0.04	-0.09
Cx	**13.5547**	0.27		1.00	0.03	0.06	0.26	0.08	0.89	0.10
Cy	**10.0102**	0.33			1.00	-0.41	0.04	-0.11	-0.00	0.31
B1	**-0.770449**	0.17				1.00	0.03	-0.15	0.04	0.14
B2	**1.98143**	0.15					1.00	-0.05	-0.11	0.03
K1	**-0.0028874**	3.3e-005						1.00	0.13	-0.45
P1	**0.00141596**	2.8e-005							1.00	0.06
P2	**-0.000193719**	1.7e-005								1.00

Table 3. Calibration coefficients and correlation matrix.

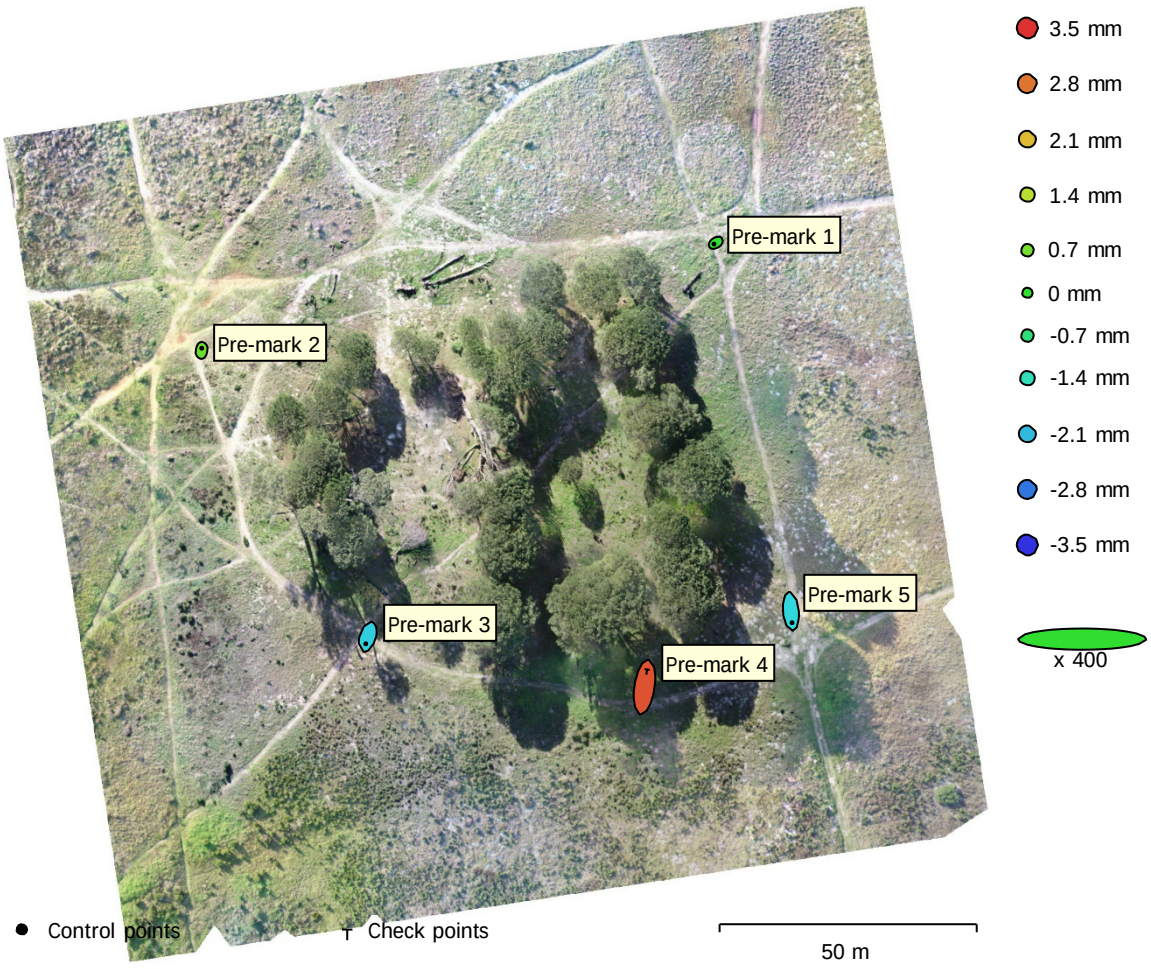

Fig. 4. GCP locations and error estimates.

Z error is represented by ellipse color. X,Y errors are represented by ellipse shape.

Estimated GCP locations are marked with a dot or crossing.

Count	X error (cm)	Y error (cm)	Z error (cm)	XY error (cm)	Total (cm)
4	0.143161	0.66345	0.134073	0.67872	0.691835

Table 4. Control points RMSE.

X - Westing, Y - Southing, Z - Altitude.

Count	X error (cm)	Y error (cm)	Z error (cm)	XY error (cm)	Total (cm)
1	0.25103	1.70126	0.315741	1.71968	1.74842

Table 5. Check points RMSE.

X - Westing, Y - Southing, Z - Altitude.

Label	X error (cm)	Y error (cm)	Z error (cm)	Total (cm)	Image (pix)
Pre-mark 1	0.180713	0.126245	-0.00569413	0.220516	0.004 (40)
Pre-mark 2	-0.0121693	-0.217364	0.0591828	0.225606	0.003 (56)
Pre-mark 3	0.1924	0.68573	-0.189287	0.736935	0.004 (185)
Pre-mark 5	-0.110261	1.10781	-0.180383	1.12781	0.011 (33)
Total	**0.143161**	**0.66345**	**0.134073**	**0.691835**	**0.005**

Table 6. Control points.

X - Westing, Y - Southing, Z - Altitude.

Label	X error (cm)	Y error (cm)	Z error (cm)	Total (cm)	Image (pix)
Pre-mark 4	-0.25103	-1.70126	0.315741	1.74842	0.009 (107)
Total	**0.25103**	**1.70126**	**0.315741**	**1.74842**	**0.009**

Table 7. Check points.

X - Westing, Y - Southing, Z - Altitude.

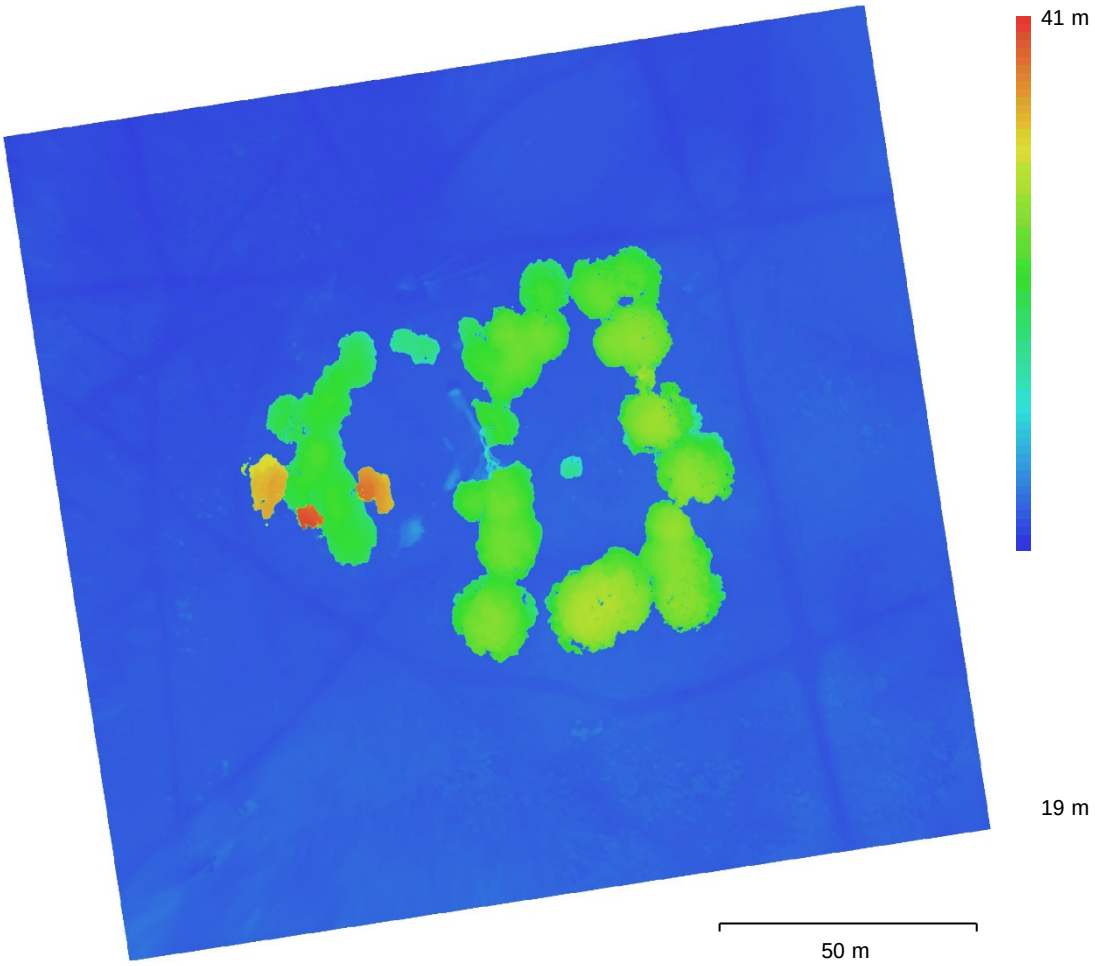

Fig. 5. Reconstructed digital elevation model.

Resolution: 4.37 cm/pix

Point density: 523 points/m²

Processing Parameters

General

Cameras	647
Aligned cameras	647
Markers	5
Coordinate system	Hartebeesthoek94 / Lo19 (EPSG::2048)
Rotation angles	Yaw, Pitch, Roll

Point Cloud

Points	74,312 of 89,281
RMS reprojection error	0.161442 (2.02264 pix)
Max reprojection error	0.839186 (72.1575 pix)
Mean key point size	11.1108 pix
Point colors	3 bands, uint8
Key points	No
Average tie point multiplicity	8.35173

Alignment parameters

Accuracy	Low
Generic preselection	Yes
Reference preselection	Yes
Key point limit	40,000
Tie point limit	1,000
Matching time	27 minutes 52 seconds

Optimization parameters

Parameters	f, b1, b2, cx, cy, k1, p1, p2
Optimization time	19 seconds

Dense Point Cloud

Points	22,303,695
Point colors	3 bands, uint8

Reconstruction parameters

Quality	Medium
Depth filtering	Aggressive
Depth maps generation time	20 hours 4 minutes
Dense cloud generation time	1 days 5 hours

Model

Faces	1,485,918
Vertices	743,442
Vertex colors	3 bands, uint8
Texture	4,096 x 4,096, 4 bands, uint8

Reconstruction parameters

Surface type	Height field
Source data	Dense
Interpolation	Enabled
Quality	Medium
Depth filtering	Aggressive
Face count	1,486,885
Processing time	27 seconds

Texturing parameters

Mapping mode	Orthophoto
Blending mode	Mosaic
Texture size	4,096 x 4,096
Enable hole filling	Yes

General

Enable ghosting filter	No
UV mapping time	7 seconds
Blending time	32 minutes 41 seconds

DEM

Size	4,395 x 4,267
Coordinate system (EPSG::2048)	Hartebeesthoek94 / Lo19

Reconstruction parameters

Source data	Dense cloud
Interpolation	Enabled
Use North Up orientation	Yes
Processing time	36 seconds

Orthomosaic

Size	17,560 x 17,000
Coordinate system	Hartebeesthoek94 / Lo19 (EPSG::2048)
Colors	3 bands, uint8

Reconstruction parameters

Blending mode	Mosaic
Surface	DEM
Enable hole filling	Yes
Use North Up orientation	Yes
Processing time	50 minutes 33 seconds

Software

Version	1.5.1 build 7618
Platform	Windows 64

APPENDIX B – HeteroFS1 Agisoft Processing Report

Tessallated Facade Aerial Mission

23 June 2020

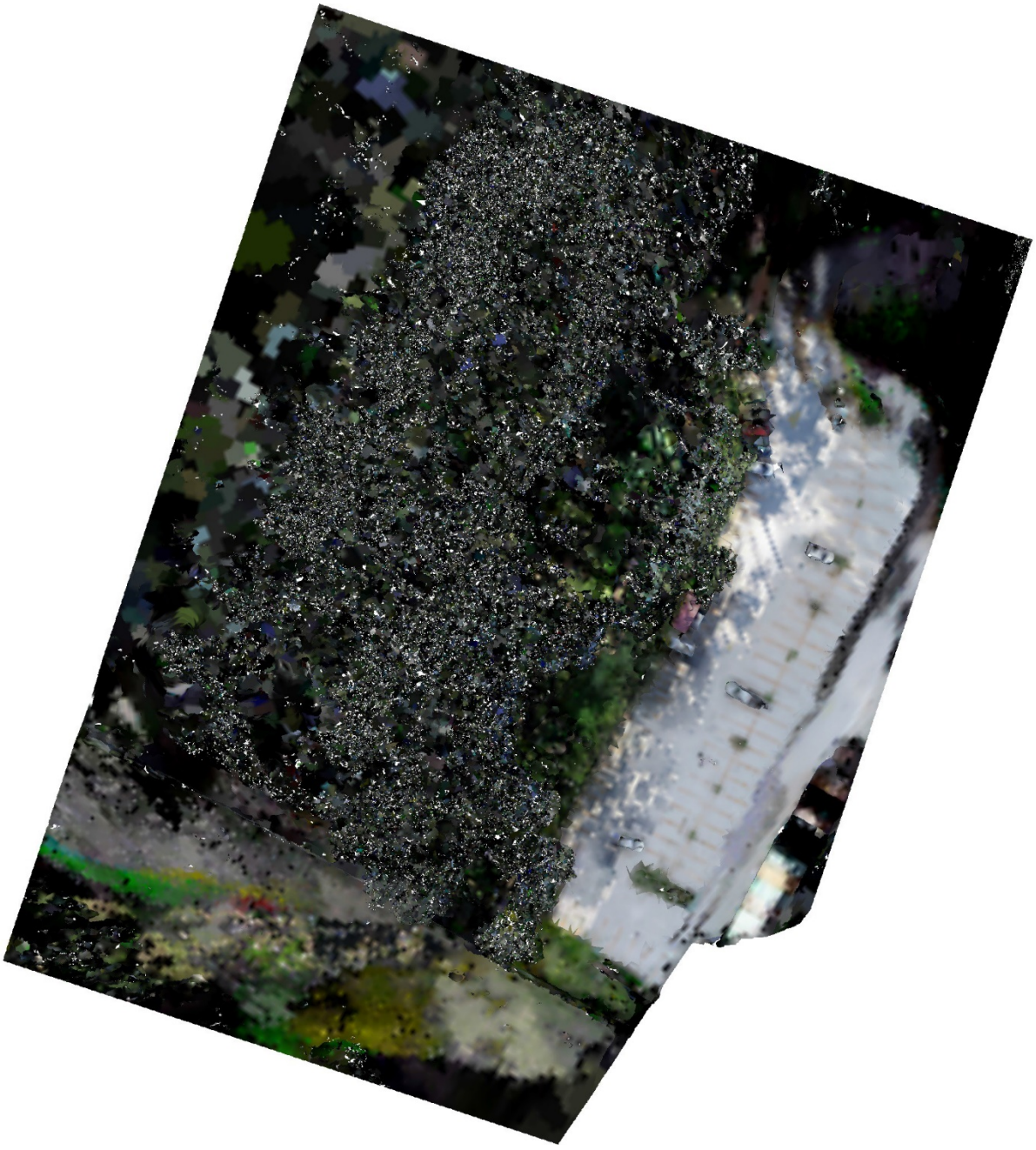

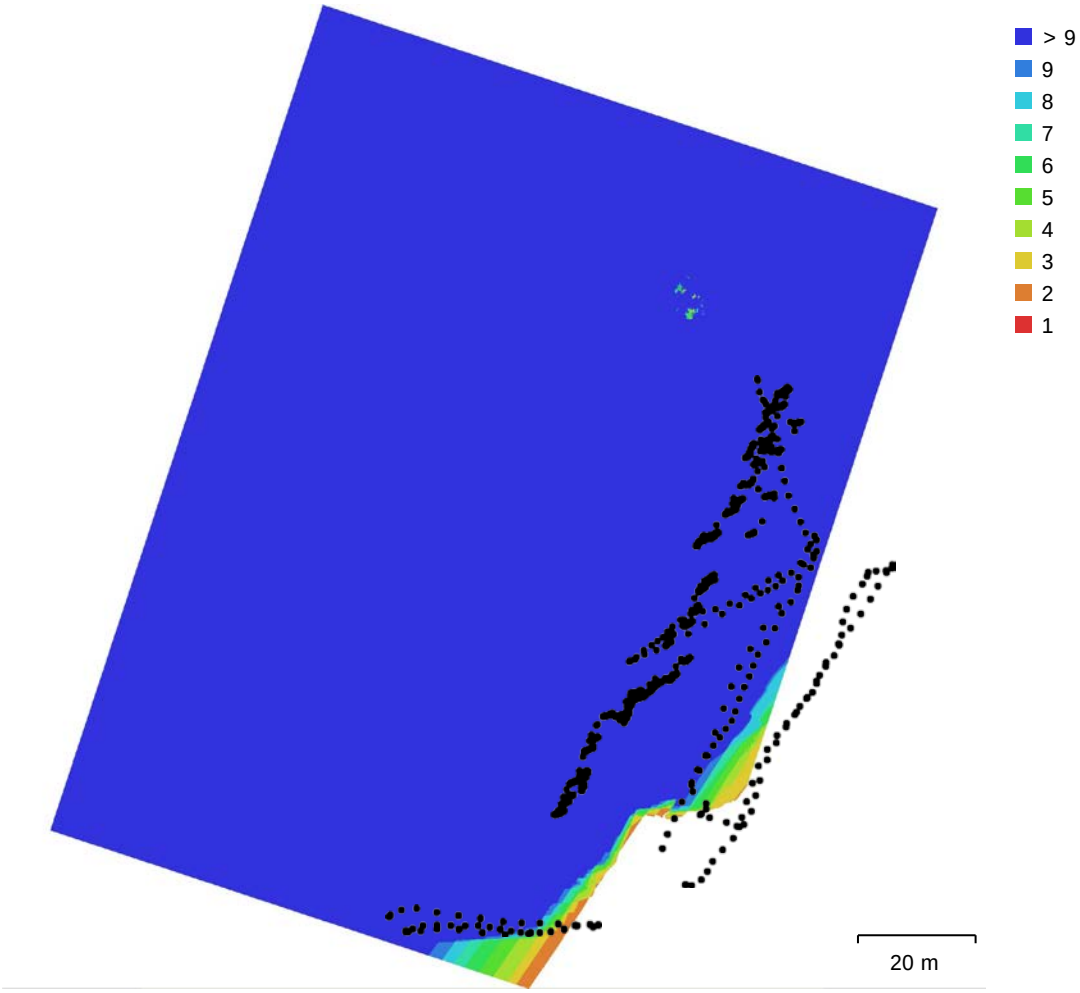

Fig. 1. Camera locations and image overlap.

Number of images:	1,250	Camera stations:	1,250
Flying altitude:	31.7 m	Tie points:	1,155,887
Ground resolution:	8.54 mm/pix	Projections:	3,559,079
Coverage area:	0.0156 km²	Reprojection error:	1.16 pix

Camera Model	Resolution	Focal Length	Pixel Size	Precalibrated
FC6310 (8.8mm)	5472 x 3648	8.8 mm	2.41 x 2.41 µm	No

Table 1. Cameras.

Camera Calibration

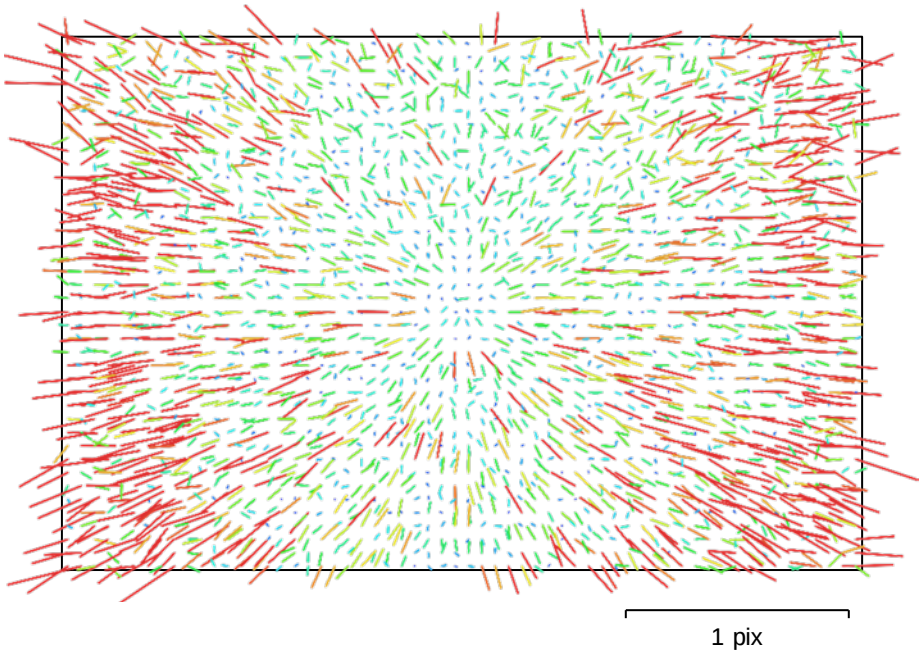

Fig. 2. Image residuals for FC6310 (8.8mm).

FC6310 (8.8mm)

1250 images

Type	Resolution	Focal Length	Pixel Size
Frame	**5472 x 3648**	**8.8 mm**	**2.41 x 2.41 µm**

	Value	Error	F	Cx	Cy	K1	K2	K3	P1	P2
F	**3678**	0.07	1.00	0.10	-0.02	-0.03	0.17	-0.15	0.09	0.01
Cx	**10.2388**	0.12		1.00	0.02	0.03	0.00	-0.01	0.92	0.06
Cy	**15.9128**	0.12			1.00	-0.08	0.03	-0.02	0.05	0.75
K1	**0.00237772**	3.7e-05				1.00	-0.94	0.88	0.03	-0.11
K2	**-0.00462638**	9.6e-05					1.00	-0.98	0.01	0.02
K3	**0.00600668**	8e-05						1.00	-0.01	-0.00
P1	**0.00121078**	8.8e-06							1.00	0.07
P2	**1.30469e-05**	7.4e-06								1.00

Table 2. Calibration coefficients and correlation matrix.

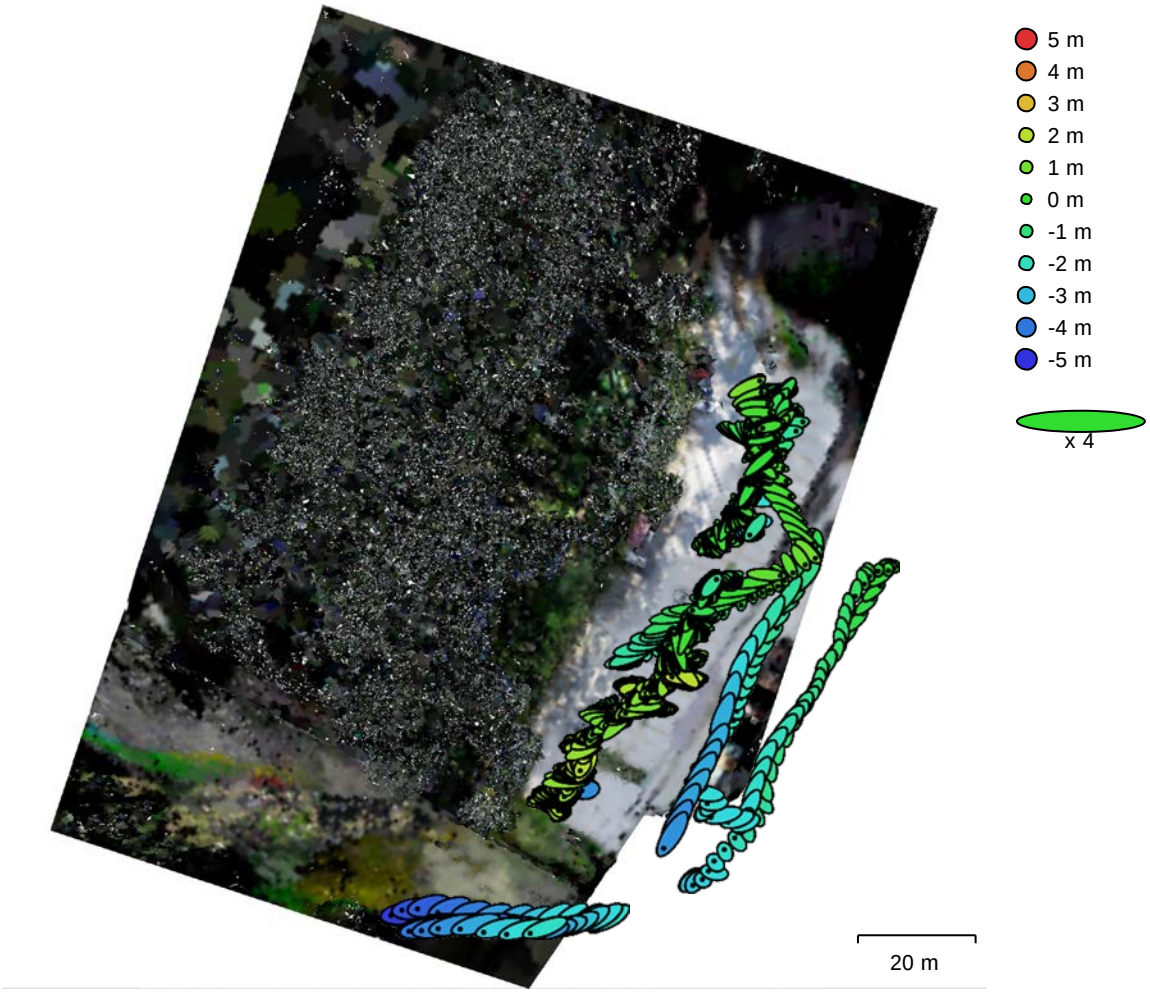

Fig. 3. Camera locations and error estimates.

Z error is represented by ellipse color. X,Y errors are represented by ellipse shape. Estimated camera locations are marked with a black dot.

X error (m)	Y error (m)	Z error (m)	XY error (m)	Total error (m)
0.698213	0.501844	1.38585	0.859854	1.63093

Table 3. Average camera location error.

X - Westing, Y - Southing, Z - Altitude.

Digital Elevation Model

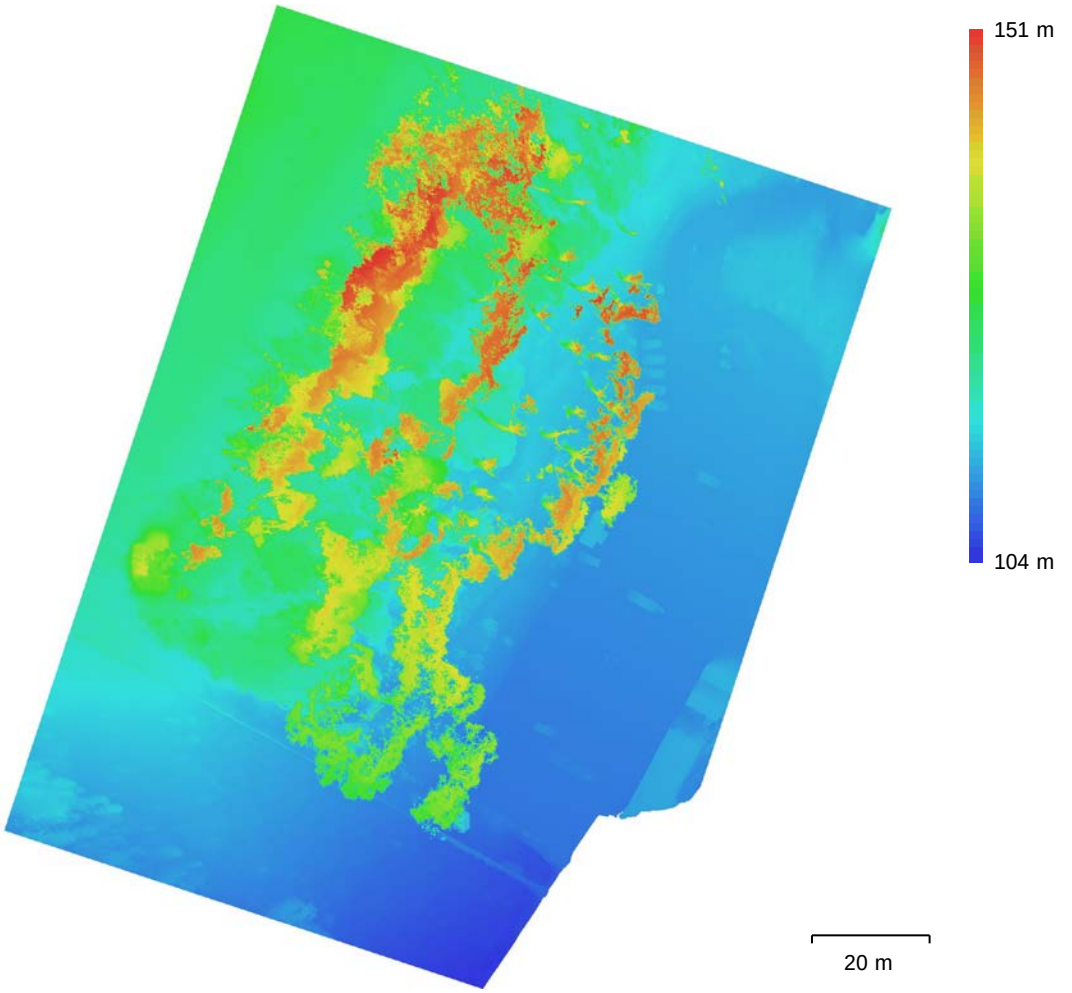

Fig. 4. Reconstructed digital elevation model.

Resolution:	1.71 cm/pix
Point density:	0.343 points/cm²

General

Cameras	1250
Aligned cameras	1250
Coordinate system	Hartebeesthoek94 / Lo19 (EPSG::2048)
Rotation angles	Omega, Phi, Kappa

Point Cloud

Points	1,155,887 of 1,905,747
RMS reprojection error	0.0998969 (1.15954 pix)
Max reprojection error	0.252544 (52.7735 pix)
Mean key point size	8.93832 pix
Point colors	3 bands, uint8
Key points	2.22 GB
Average tie point multiplicity	3.52415

Alignment parameters

Accuracy	Medium
Generic preselection	Yes
Reference preselection	Source
Key point limit	40,000
Tie point limit	10,000
Guided image matching	No
Adaptive camera model fitting	No
Matching time	5 minutes 4 seconds
Matching memory usage	220.85 MB
Alignment time	23 minutes 8 seconds
Alignment memory usage	1.70 GB
Software version	1.6.2.10247

Depth Maps

Count	1250

Depth maps generation parameters

Quality	High
Filtering mode	Aggressive
Processing time	1 hours 17 minutes
Software version	1.6.2.10247

Dense Point Cloud

Points	218,459,096
Point colors	3 bands, uint8

Depth maps generation parameters

Quality	High
Filtering mode	Aggressive
Processing time	1 hours 17 minutes

Dense cloud generation parameters

Processing time	4 hours 43 minutes
Software version	1.6.2.10247

Model

Faces	43,670,116
Vertices	21,838,559
Vertex colors	3 bands, uint8

Processing Parameters

Texture	4,096 x 4,096, 4 bands, uint8

Depth maps generation parameters

Quality	High
Filtering mode	Aggressive
Processing time	1 hours 17 minutes

Reconstruction parameters

Surface type	Height field
Source data	Dense cloud
Interpolation	Enabled
Strict volumetric masks	No
Processing time	12 minutes 33 seconds

Texturing parameters

Mapping mode	Generic
Blending mode	Mosaic
Texture size	4,096
Enable hole filling	Yes
Enable ghosting filter	Yes
UV mapping time	1 hours 15 minutes
Blending time	49 minutes 48 seconds
Software version	1.6.2.10247

DEM

Size	8,866 x 10,269
Coordinate system	Hartebeesthoek94 / Lo19 (EPSG::2048)

Reconstruction parameters

Source data	Dense cloud
Interpolation	Enabled
Use North Up orientation	Yes
Processing time	1 minutes 24 seconds
Software version	1.6.2.10247

System

Software name	Agisoft Metashape Professional
Software version	1.6.2 build 10247
OS	Windows 64 bit
RAM	127.87 GB
CPU	AMD Ryzen Threadripper 2990WX 32-Core Processor
GPU(s)	GeForce RTX 2070 SUPER GeForce RTX 2070 SUPER